Department für Bautechnik und Naturgefahren

Institut für Geotechnik

Vorstand und Betreuer: **Univ.Prof.Dr.-Ing. Wei Wu**

Numerical Modelling of Snow Avalanches

Interaction between Granular Flow and Obstruction

Dissertation zur Erlangung des Doktorgrades
an der
Universität für Bodenkultur Wien

Eingereicht von **Dipl.-Ing. Markus Wawra**

Wien, August 2010

Dissertation Nr. 25

Danksagung

Diese Dissertation wurde im Laufe eines Projekts am Institut für Geotechnik der Universität für Bodenkultur verfasst. Ich möchte mich bei meinem Betreuer und Institutsvorstand Wei Wu und dem Projektleiter Yongqi Wang herzlich bedanken, die mir die Mitarbeit an diesem Projekt und damit das Verfassen meiner Dissertation ermöglicht haben. Sie waren beide stets wichtige und hilfreiche Ansprechpartner für mich und ich konnte viel von ihnen lernen, sowohl fachlich, wie sprachlich, wie in der Methodik des wissenschaftlichen Arbeitens.
Finanziert wurde das Projekt durch den FWF, Fonds zur Förderung der wissenschatlichen Forschung der Republik Österreich.
Auch bei den anderen Mitarbeitern des Instituts möchte ich mich bedanken. Vor allem bei meinem Kollegen Harald Teufelsbauer, der mit mir an diesem Projekt gearbeitet hat und die hier präsentierten diskreten Berechnungen durchgeführt hat. Auch Shiva P. Pudasaini gilt mein gesonderter Dank. Er war vor allem in der Anfangsphase ein hilfreicher Ansprechpartner und hat mir das Einarbeiten in das Fachgebiet erleichtert.
Bedanken möchte ich mich auch bei meiner Familie und meinen Freunden, für ihre Unterstützung und die gemeinsame Zeit abseits des Universitätsalltags.

Markus Wawra

Abstract

Snow avalanches have always been a big threat for people in mountainous areas. Increased population and the exploitation of outlying valleys for winter sport tourism has aggravated the situation in the 20^{th} century and a lot of money is spent to protect endangered areas.
At the same time scientific interest has risen and various models have been proposed to describe the complex behaviour of snow avalanches with different approaches having different advantages and disadvantages.
The topic of this dissertation is the interaction between granular flows and obstructions of different shape.
Two very different approaches will be applied to model the granular material numerically, on one side a continuum mechanical model, based on Savage-Hutter theory (1989) and on the other side the Discrete Element Method (DEM) by Cundall and Strack (1979).
The continuum mechanical model of Savage and Hutter has proven in the past to be an appropriate model to simulate dense-flow avalanches. The depth-integrated formulation is elegant, but presumes a shallow flow. This condition is not fulfilled if obstructions with steep fronts, like walls or dams, are hit, since material is accumulated there. The limits of the existing model are presented and different approaches to building obstructions into the model are discussed. Further, the numerical solver, the NOC-scheme (Non-Oscillatory Central Difference) with TVD-limiter (Total Variation Diminishing) is extended by the Adaptive-Mesh-Refinement method (AMR), which provides local grid refinement. The suitability of the extended model is discussed for different obstructions and compared to experiments by Chiou (2006).
As an alternative to the continuum mechanical model, DEM is discussed, following the work of Teufelsbauer et al. (2009). The model is programmed in the commercial software PFC3d. The advantage of this method is the completely three-dimensional modelling of the mass. The granular mass is simulated by small balls and the motion and the interaction among each other is described by simple physical laws. The large number of elements needed requires high computational effort, though. DEM is compared to the

same experiments by Chiou.
Additionally, impact forces of the granular material on the obstruction are computed for both models. In addition to the measurements of Chiou, measurements by Moriguchi et al. (2009) are employed.

Zusammenfassung

Schneelawinen sind seit jeher einen großes Risiko für Menschen in Gebirgsregionen. Durch die dichter werdende Besiedlung und die Erschließung entlegener Täler durch den Wintersporttourismus hat sich die Lage im 20. Jahrhundert deutlich verschärft. Viel Geld wird in die Sicherung gefährdeter Gebiete investiert.
Im gleichen Zeitraum ist auch das Interesse einer wissenschaftlichen Beschreibung gestiegen. Verschiedene Modelle wurden vorgeschlagen um den komplexen Abgang einer Schneelawine zu beschreiben. Die unterschiedlichen Ansätze haben alle ihre Vor- und Nachteile.
In dieser Dissertation wird die Interaktion von granulären Flüssen mit verschiedenförmigen Hindernissen behandelt. Zwei sehr unterschiedliche Ansätze werden zur numerischen Modellierung des granulären Materials herangezogen, zum einen ein kontinuumsmechanisches Modell, basierend auf der Savage-Hutter-Theorie (1989), zum anderen die Diskrete-Elemete-Methode (DEM) von Cundall und Strack (1979).
Das kontinuumsmechanische Modell von Savege und Hutter hat sich in der Vergangenheit als geeignetes Modell für die Simulation von Fließlawinen bewährt. Die tiefenintegrierte Formulierung ist elegant, setzt aber eine niedrige Fließhöhe voraus. Diese Bedingung wird beim Auftreffen auf Hindernisse mit steiler Front, wie Wänden oder Dämmen, nicht mehr erfüllt, da sich das Material dort anstaut. Die Grenzen des vorhandenen Modells werden aufgezeigt und unterschiedliche Ansätze Hindernisse in die Topographie einzubauen diskutiert. Weiters wird der numerische Lösungsalgorithmus NOC-Schema (Non-Oscillatory Central Difference) mit TVD-Begrenzer (Total Variation Diminishing) mit der Adaptive-Mesh-Refinement-Methode (AMR) erweitert, die eine lokale Netzverfeinerung ermöglicht. Die Eignung des erweiterten Modells wird für verschiedene Hindernissen untersucht und mit experimentellen Ergebnissen von Chiou (2006) verglichen.
Als Alternative zum kontinuumsmechanischen Modell wird die DEM diskutiert, folgend der Arbeit von Teufelsbauer u.a. (2009). Das Modell wird in der kommerziellen Software PFC3d programmiert. Der Vorteil dieser Metho-

de ist die vollständige dreidimensionale Modellierung der Masse. Die granuläre Masse wird durch kleine Bälle simuliert. Deren Bewegung und das Aufeinandertreffen der Bälle miteinander werden durch einfache physikalische Gesetzte beschrieben. Durch die erforderliche hohe Anzahl an Bllen ist die Methode aber sehr rechenaufwendig. DEM wird für die Simulation der gleichen Experimente von Chiou herangezogen und verglichen.
Des Weiteren werden für beide Modelle die Aufprallkräfte des granulären Flusses berechnet, die auf das Hindernis wirken. Zusätzlich zu Messergebnissen von Chiou werden auch Kraftmessungen von Morigutchi u.a. (2009) zu Vergleichen herangezogen.

Contents

Chapter 1

Introduction

People living in mountainous area had acquired considerable experience to deal with snow avalanches and to avoid high risk areas long before scientists started to work on this topic. Scientists, intellectuals or artists rarely visited mountainous regions for long time, so most publications of that time were based on imagination rather than observation. Early descriptions showed avalanches as huge snowballs rolling down the slope. This image can be found on various old paintings and even modern ones, like comic strips.

The scientific research of snow avalanches started in Switzerland with the first documentations in the 18th century. In the 19th century also other countries became interested. In that time, most effort was made to protect the newly built infrastructure like railroad tracks or mining facilities. The first institutes, dealing with avalanches in organized ways, were not established before the 1930s. Again it was Switzerland that did pioneering work and founded the Eidgenössisches Institut für Schnee- und Lawinenfoschung (EISLF, Swiss Federal Institute of Snow and Avalanche Research). After World War II also other countries, all around the world, founded similar institutes and many of them were strongly influenced by the Swiss group.

Modern avalanche protection has to be diverted into two very different fields, which strongly interact. One field is the observation, simulation and estimation of snow covers. This starts at meteorology and field observations to estimate the amount of snow. Closely related is the observation of the structure of the snow cover. Snow can be very different and its consistency changes permanently throughout winter. A snow cover can therefore be from stable to instable state. These observation are used by local authorities to inform and warn people, especially skiers, and, if necessary, to evacuate endangered areas or close roads. To avoid dangerous situations, explosives are often used to release small avalanches, so that no critical masses can build up. Moreover, snow fences are built to avoid transportation of snow by wind into critical

release zones. Snow bridges are built directly in the release zone, to a avoid a release, but they fail if the snow cover is higher than the construction.
The second field is the simulation and estimation of moving avalanches. There are two different kinds of snow avalanches namely powder snow avalanche and dense flow avalanche. Different models are needed for both types. All avalanches start as dense flow avalanches. They consist of dense granular material like fluids. On steep terrain a powder snow layer can build up above the dense flow forming a powder snow avalanche. Such powder snow layers consist of relatively small ice particles suspended in the air and show gaseous behaviour.
Avalanche models are used to estimate run out zones of possible avalanches to protect people and infrastructure in the mountainous areas. As protection measure, breaking dams are often built in the slope to divert the flow into less powerful and smaller avalanches. Catching dams are built in the run out area to reduce the run out zone and protect buildings behind the dam. Similar tasks can be fulfilled by deflecting dams or galleries, which are usually built to protect streets or railroads.
The interaction of avalanches with dams is not described satisfactory by actual models and will be the topic of this work.

1.1 Avalanche Models

Various models have been developed in the last century. These models have their advantages and disadvantages. The use of certain models in practice is often a question of regional practice and knowledge. Also current research goes in many different directions. This section provides a short overview of some classical avalanche models.

1.1.1 Statistical Models

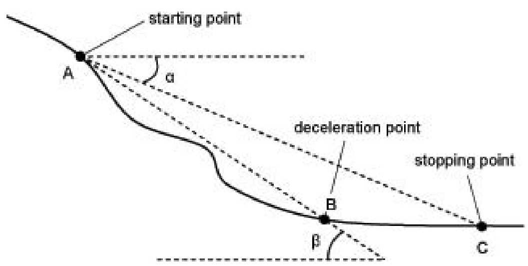

Figure 1.1: Sketch of a statistical model with starting point A, deceleration point B and stopping point C on an one-dimensional curved topography.

Statistical models are usually based on documented avalanches of the past or methods for computing boundaries of the avalanches. They are used to work out hazard maps, by determining the avalanche spread. Among the many proposed statistical models, a widely used model is briefly recapitulated here. Along the slope, a continuous curve (e.g. a parabola) is laid through three points to describe a one-dimensional path of the avalanche, see Figure 1.1. The first, A, is the initiation point, the second, B, the one in the transition zone and the third point, C, marks the position where the avalanche stops. Now the average inclination angle β is defined as angle between the horizontal and the straight line between A and B. The angle α, between the horizontal and the straight line between A and C, is called stopping angle. α can now be expressed as a function of β by using regression methods. The model can be explicitly written as $\alpha = \lambda\beta + \gamma$, where λ is the regression coefficient and γ a constant. These parameters have to be determined by field studies. These parameters have to be varied to achieve reliable results. This model was proposed by Lied and Bakkehøi [39] and McClung and Lied [41].

The advantages of statistical models are relative simplicity and reliability for a fixed topography and have therefore been used for many years in practice. On the other hand, the return period is very long. For every single avalanche track datasets of typically 100 years are needed. Further, the one-dimensional model can not simulate areal spread, which is a very important feature in risk zone mapping. The simplification also ignores other effects than geometrical features, like rheological and mechanical properties of snow.

1.1.2 Mass Point Models

Mass point models are based on the pioneering work of Voellmy [63]. He assumed uniform and steady conditions and utilized a center of mass approach. Voellmy's model combines a shear traction at the base of the flow, relative to the square of the velocity, with Coulomb friction. To obtain results that match field studies, a number of subjective parameters must be predetermined. This allows a wide field of application. Depending on the choice of the parameters, both dense flow and powder snow avalanches can be simulated. The parameter identification can be difficult and is crucial to receive realistic results. Until the late 1980s, mass point approach was the most used avalanche model. Many attempts were made to improve Voellmy's model, but the main weakness of the mass point approach remained. They cannot provide information about temporal or spatial properties, like velocity distributions and the evolution of height and spread of avalanches. These are certainly not constant as Voellmy proposed.

1.1.3 Hydraulic Models

Hydraulic models are based on Navier-Stokes equations, which may be solved numerically. They simulate channel flows, as they are known from river hydrodynamics. The focus is on flow depth and flow velocity. Very popular are models based on Saint Vernant equations with depth integration for shallow flow. Usually incompressibility is assumed. Some attempts were made to obtain flow profiles that match observations by employing the constitutive model of Ericksen-Fibley fluid combined with Coulomb friction model to generalize it to an unsteady three-dimensional model. But non of them has so far been applied to general flow conditions. Hydraulic models are mainly used when geometric aspects shall be observed. It is obviously not feasible to assume that this type of constitutive relation adequately describes the complex behaviour of snow.

1.1.4 Kinetic Models

Kinetic models are applied for rapidly moving masses, where particles are in high agitative motion and interact by frequently colliding with other particles. This can be described as dense granular gas. The balance laws for mass, momentum and fluctuation energy for the field variables density, velocity and temperature are needed to describe the kinetic theory. Even for steady chute flows the solution becomes very complicated, as rather complex boundary conditions for granular temperature, stresses and velocities are required. Jenkins and Richardson [27] derived explicit forms of boundary conditions for ideal situations of identical spheres and regular bumpy boundaries. A further step of Jenkins [26] was to apply a mixed theory, where the upper part of avalanches is assumed to behave like a frictional plastic mass, while at its base, in a thin shear layer, the grains interact strongly through collisions. The upper part is assumed to deform by frictional shear, described by Mohr-Coulomb criterion. The relations between shear stress, normal stress and relative velocity of the boundaries in the shear layer can be determined [26].

1.1.5 Discrete Element Method (DEM)

The idea of DEM is to simulate the motion of single particles following Newton's second law of motion. The contact rules treat the interaction of particles when colliding with one another or the boundary. Generally, DEM is a useful tool to understand the behaviour of dry granular avalanches. Although the theoretical background is relatively simple, the implementation is rather difficult. For problems in the practice the number of particles is usually too large to be handled, even if considering small scale laboratory experiments. The tracks of all these particles must be computed and checked for collusions with all other particles at any time, resulting in a high demand for memory. Several numerical methods for more effective simulations have been suggested, but when compared to other models, the effort is still enormous. Another difficulty is the behaviour of the particles. Usually spherical particles are used, which simplifies the collusion computations. Introducing features like elasticity, slipping or overlapping allows a realistic behaviour of the particles, but some features of natural materials, like cohesion, which is very typical for snow, is difficult to model.

1.1.6 Continuum Mechanical Models

In this work focus will be on continuum models. Particularly, the models based on Savage-Hutter theory [51], [52], which was developed as a two dimensional model for gravity-driven, free-surface granular flows and has been extended to three dimensions [13], [25], [49]. In the last two decades, it became an attractive approach with adequate description of the behaviour of dense flows. It consists of depth-integrated balance laws of mass and momentum and has a similar mathematical structure as the shallow-water equations, known from hydrodynamics. The material is considered incompressible and obeys a dry Coulomb-type friction with constant internal friction angle. Nonlinear earth pressure coefficients are introduced to describe the ratio of overburden pressure and normal pressure in downflow- and cross-flow-direction. Altogether, the internal friction angle and the bed friction angle, which measures the friction between the moving granular mass and the bed surface, enter the model as only material parameters. The extended model is feasible to model flows on arbitrarily curved surface with small local irregularities.

1.2 Goals of this Work

The goal of this work is to simulate the interaction between granular flow and obstructions. The existing continuum mechanical model will be improved and tested.

In Chapter 2, the continuum model based on Savage-Hutter theory, is introduced. Starting with the simple one-dimensional model, the depth-averaged two-dimensional model in a curvilinear coordinate system with all its simplifications is presented.

Chapter 3 discusses the numerical solution. In the last two decades various schemes have been applied and tested on Savage-Hutter theory. The best performance has been shown by the non-oscillatory central (NOC) scheme with a Total Variation Diminishing (TVD) Minmod limiter. This scheme is used here.

The interaction between granular flows and obstructions is discussed in Chapter 4. The elevation function is used to model the obstructions. The model is compared with experiments by Chiou [8]. Some weaknesses of this approach will be discussed. As an alternative to continuum modelling, a PFC3d model, based on Discrete Element Method (DEM), is compared with the same experiments.

To improve the continuum model, the Adaptive Mesh Refinement (AMR) is applied. AMR makes use of local grid refinement and improves the results of the model significantly. However, the physical inadequacy of depth-averaged models to simulate the complex behaviour of granular flows interacting with steep walls remains. AMR is discussed in Chapter 5.

In Chapter 6, an alternative method to implement cuboid obstructions is proposed. The obstruction is built directly into the basal surface by adding planes to the slope plane. At the intersection of the planes, the mass is transfered form one plane to the other. At these intersections singularities occur. A simple method to handle this with a single parameter is suggested and a parameter study performed.

In Chapter 7, the impact forces on the obstructions are calculated and compared to experiments. Both, the continuum mechanical model and DEM are considered. As alternative to the chute experiments, also a flume experiment is simulated for both the continuum and discontinuum model. In the continuum mechanical model the wall is implemented as boundary condition in this case, with realistic results, although the results cannot be compared to the experiment, due to the overflow in the experiment.

The final Chapter 8 contains a summary of the results and some suggestions for future work.

Chapter 2

Extended Savage-Hutter Model

In 1989, Savage and Hutter [51] were the first who published a model for finite granular mass evolving and sliding down an inclined slope, which is based on continuum mechanics. The original model is two-dimensional, but it has been extended to three dimensions by Hutter et al. [25], Greve et al. [15], Gray et al. [13] and Pudasaini and Hutter [49]. Several adequate simplifications were made leading to an elegant mathematical formulation. Some of them have already been known from shallow water equations.

- The volume is assumed to be constant. Experimental observations have shown that the moving mass preserves its volume. Only at the initiation the volume expands and at the stand still the volume compacts. Since the theory mainly describes the dynamic process, volume preserving is reasonable.

- The moving dry granular mass is cohesionless. The constitutive equations for the internal stresses are based on the Mohr-Coulomb yield criterion.

- The shear stresses orthogonal to the main flow direction can be neglected.

- Thermal effects can be neglected.

- To simplify the formulation, moving masses are considered shallow, in the sense that the typical depths are small compared to length and width along the surface.

- The avalanching motion consists of shearing within the deforming mass and sliding along the basal surface. The basal boundary layer, where the shearing deformation takes place, is very thin and considered to be of zero thickness. This is justified by observations. Sliding and shearing are combined to a single sliding law. Hence, depth-averaged equations may be used.

- Integration through the avalanche depth, with kinematic boundary conditions at the free surface and base of the avalanche, reduces the spacial dimension of the theory spatially.

- Scaling analysis identifies the physically significant terms in the governing equations and isolates negligible terms.

In this chapter the simple one-dimensional model will be presented in the first section, to understand the basic ideas of the model. The second section shows the more general two-dimensional model.

2.1 One-Dimensional Model

To understand the basic Savage-Hutter equations, it is useful to look at a very simple one-dimensional flow down an inclined plane, with inclination angle ζ. The downflow direction is represented by the x-coordinate, while z-coordinate is orthogonal to it. Assume that the density ρ of the granular material is constant and that the velocity is constant over depth, so that $u(x,z,t) = u(x,t)$. Looking at the change of mass in a column of length dx, which is equivalent to the change of height, yields

$$\begin{aligned} \frac{\partial}{\partial t}(\rho h(x,t))dx &= \rho h(x,t)u(x,t) - \rho h(x+dx,t)u(x+dx,t) \qquad (2.1) \\ &= -\frac{\partial}{\partial x}(\rho h(x,t)u(x,t))dx + \mathcal{O}((dx)^2), \end{aligned}$$

where h is the flow height and in- and outflow of the infinitesimal element $x \in [x, x+dx]$ are summed up, see Figure 2.1.
Since ρ is considered constant, (2.1) reduces to

$$\frac{\partial h}{\partial t} + \frac{\partial (hu)}{\partial x} = 0. \tag{2.2}$$

This equation is called mass balance.

For the same element the balance of x-momentum, given by $\rho hu\, dx$, can be derived. Again the time rate of change and the flux through the column walls,

$$\frac{\partial}{\partial t}(\rho h(x,t)u(x,t))dx + \frac{\partial}{\partial x}(\rho h(x,t)u^2(x,t))dx, \tag{2.3}$$

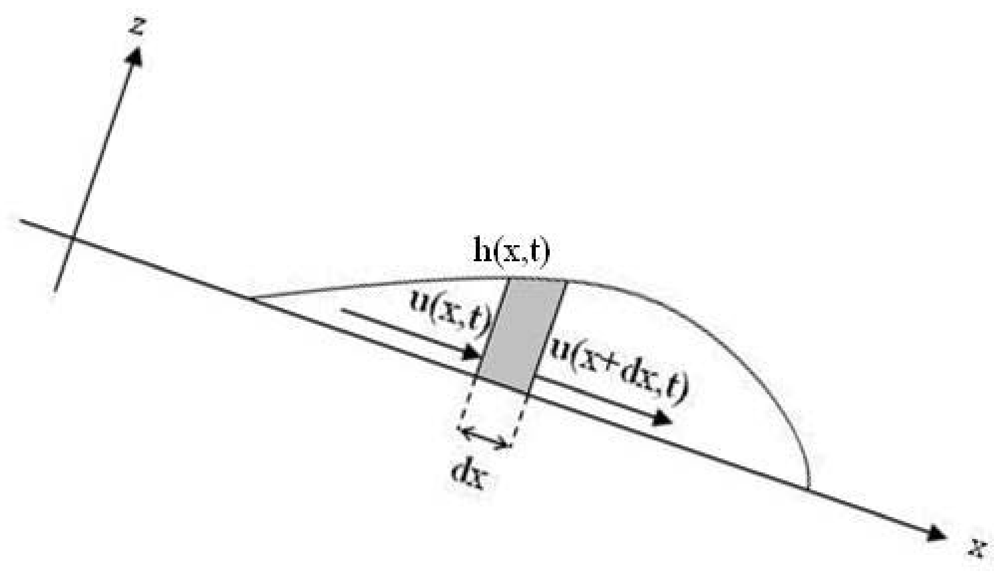

Figure 2.1: One-dimensional flow of granular material down an inclined plane with infinitesimal column where mass and momentum balances are formulated.

are the considerable contributions. But the forces acting on the column have also to be considered, as there are:

$$\text{gravity} \qquad \rho g h \sin\zeta \, dx \tag{2.4}$$

$$\text{basal friction} \qquad -\text{sgn}(u)\tau dx \tag{2.5}$$

$$\text{longitudinal pressure} \qquad \int_0^{h(x,t)} p_L(x,z,t)dz - \int_0^{h(x+dx,t)} p_L(x+dx,z,t)dz. \tag{2.6}$$

To the basal friction a Coulomb-type friction law is applied with bed friction angel δ, in the form

$$\tau = \tan\delta \, p_b,$$

where p_b denotes the isotropic pressure at the bed. Using a hydrostatic pressure distribution

$$p_b(x,t) = \rho g h(x,t)\cos\zeta,$$

(2.5) becomes:

$$(2.5) = -\text{sgn}(u)\tan\delta\rho g h(x,t)\cos\zeta \, dx. \tag{2.7}$$

p_L is the longitudinal pressure that may be different from the overburden pressure. The relation is described by a common ansatz from soil mechanics

$$p_L(x,z,t) \;=\; K_{act/pas}\, p(x,z,t). \tag{2.8}$$

$K_{act/pas}$ is dimensionless and is called earth pressure coefficient. The literature in soil mechanics suggests to use two different values for $K_{act/pas}$, one for an extending (K_{act}) and one for a compressing flow (K_{pas})

$$K_{act/pas} \;=\; \begin{cases} K_{act}, & \text{if} \quad \partial u/\partial x > 0, \\ K_{pas}, & \text{if} \quad \partial u/\partial x < 0. \end{cases} \tag{2.9}$$

Applying this, (2.6) can be written as

$$(2.6) = -\rho g \frac{1}{2}\frac{\partial}{\partial x}(K_{act/pas} h^2(x,t)) \cos\zeta \, dx + \mathcal{O}\left((dx)^2\right). \tag{2.10}$$

The collected terms can now be combined as (2.3)=(2.4)+(2.7)+(2.10). Reducing this formula by the common factor $\rho\, dx$, the momentum balance equation becomes

$$\begin{aligned} &\frac{\partial}{\partial t}(hu) + \frac{\partial}{\partial x}(hu^2) = \\ &\qquad g\left\{(\sin\zeta - \operatorname{sgn}(u)\tan\delta\cos\zeta)h - \frac{1}{2}\frac{\partial}{\partial x}(K_{act/pas} h^2)\cos\zeta\right\}. \end{aligned} \tag{2.11}$$

The equations (2.2) and (2.11) are the original Savage-Hutter equations for finite granular mass flowing down an inclined plane with inclination angle ζ [1]. The gravitation (2.4) is the driving force of the model. The basal friction (2.7) decelerates the flow, while the longitudinal pressure variation (2.10) is mainly responsible for changing the shape of the material. It may be directed both up- and downwards the slope. The implementation of the longitudinal pressure is, next to the assumption of the hydrostatic pressure, the most essential element of the model from a physical point of view.

When $p = p_L$, i.e. $K_{act/pas} = 1$, the model becomes a hydraulic model, also known as Saint Venant or Boussinesq equations. The pressure distribution is that of a still liquid.

The more complex case of $K_{act/pas} \neq 1$ is still remaining to be discussed in the above derivation. To determinate the active and passive earth pressure coefficients, K_{act} and K_{pas}, the stress space, respectively the Mohr circle for

[1] It should be remarked that this is not the way the equations were derived in the original paper [51]. This introduction follows the way the equations were derived in [50].

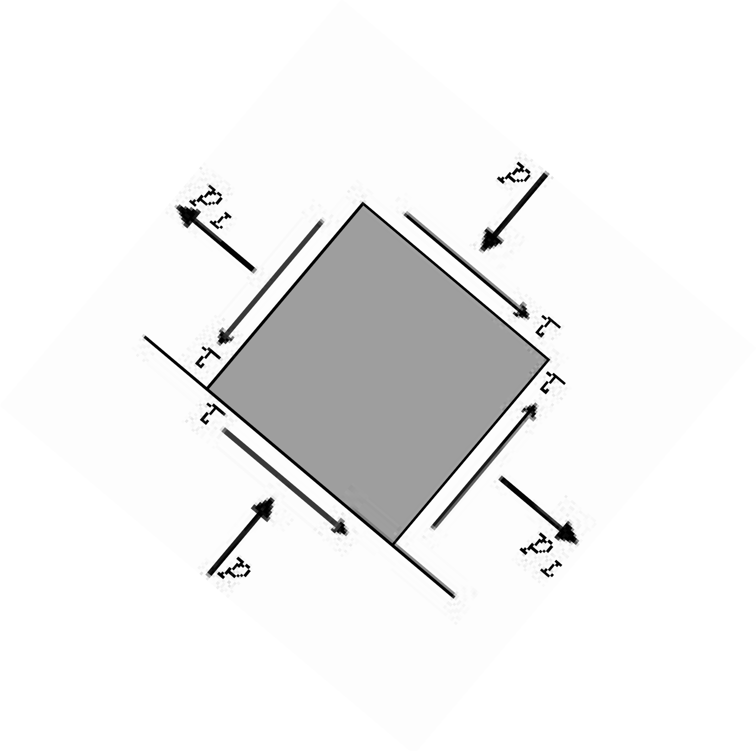

Figure 2.2: Stresses (p, τ) and (p_L, τ) acting on a plane element at the basal plane.

a material plane element at the base of the mass has to be observed. Figure 2.2 shows how p, p_L and τ act on this element. Assuming that the mass behaves as a cohesionless Coulomb material with internal friction angle ϕ and basal friction angle δ, the state of stress (p, τ) has to lie on the straight line through the origin and with inclination angle δ (see Figure 2.3). (p, τ) also has to lie on the Mohr circles. The straight lines through the origin and inclined by $\pm\phi$ are tangents of the circles. Given this, two circles are described, a smaller one, describing the active stress states, and a larger one of the passive stress states. (p_L, τ) lies on the opposite site of the respective circle, on one line with (p, τ) and the center $(= (p + p_L)/2)$. These geometric conditions can now be used to derive $K_{act/pas}$. (p, τ) lying on the straight line yields

$$\tau = p \tan \delta. \tag{2.12}$$

When looking at the rectangular triangular given by the vertexes origin, center of the circle and intersection of circle and tangent, the relation

$$\sin \phi = \frac{r}{\frac{1}{2}(p_L + p)}, \tag{2.13}$$

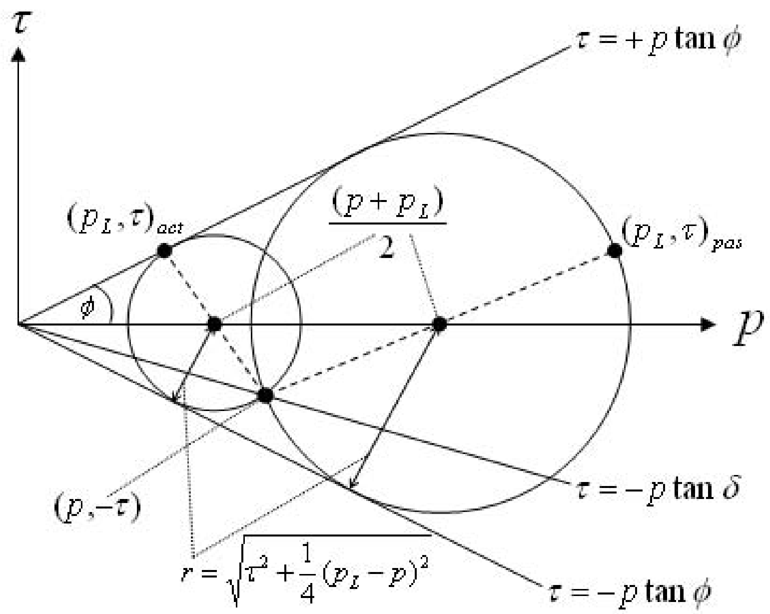

Figure 2.3: Mohr circles for active and passive stress states.

becomes obvious, where r, the radius of the Mohr circle, is given by

$$r = \sqrt{\tau^2 + \frac{1}{4}(p_L - p)^2} \tag{2.14}$$

Substituting (2.12) in (2.14) and the result in (2.13), yields

$$\sin\phi = \frac{\sqrt{p^2\tan^2\delta + \frac{1}{4}(p_L - p)^2}}{\frac{1}{2}(p_L + p)}. \tag{2.15}$$

Since $K_{act/pas} = p_L/p$, (2.15) can be transformed into a quadratic equation for $K_{act/pas}$

$$K^2_{act/pas} - 2(\frac{2}{\cos^2\phi} - 1)K_{act/pas} + 1 + \frac{4\tan^2\delta}{\cos^2\phi} = 0, \tag{2.16}$$

for which the solution is given by

$$K_{act/pas} = \frac{2}{\cos^2\phi}\left(1 \mp \sqrt{1 - \frac{\cos^2\phi}{\cos^2\delta}}\right) - 1. \tag{2.17}$$

The minus sign is used for active pressure, the plus for passive pressure. In this way $K_{act/pas}$ is dependent only on the two material constants. This is

especially important in practice, since ϕ and δ are relatively simple to be determined.
So far, all presented equations are in dimensional form. To derive non-dimensional forms, a length scale L, a depth scale H, a time scale $\sqrt{L/g}$ and a scale for velocity $\sqrt{gL}$ have to be introduced. Then let

$$\begin{aligned}
x_{dim} &= L\, x_{non-dim}, \\
z_{dim} &= H\, z_{non-dim}, \\
h_{dim} &= H\, h_{non-dim}, \\
u_{dim} &= \sqrt{Lg}\, u_{non-dim}, \\
t_{dim} &= \sqrt{L/g}\, t_{non-dim},
\end{aligned}$$

where the dimensional variables are listed on the left hand side, while the dimensionless pendants are stated on the right side. When substituting this dimensionless forms into the Savage-Hutter equations (2.2) and (2.11), the non-dimensional form is

$$\begin{aligned}
\frac{\partial h}{\partial t} + \frac{\partial (hu)}{\partial x} &= 0, \qquad (2.18) \\
\frac{\partial (hu)}{\partial t} + \frac{\partial (hu^2)}{\partial x} &= (\sin\zeta - \operatorname{sgn}(u)\tan\delta\cos\zeta)h - \frac{\partial}{\partial x}\left(\frac{\varepsilon}{2} K_{act/pas} h^2 \cos\zeta\right),
\end{aligned}$$

where

$$\varepsilon = \frac{H}{L} \ll 1,$$

is the aspect ratio, which is usually very small.

2.2 Two-Dimensional Model

In this section the one-dimensional Savage-Hutter model will be extended to two-dimensional. For this purpose, the general conservation laws in continuum mechanics are used to start the derivation form.

2.2.1 Governing Equations

The governing equations are known from continuum mechanics. The material is assumed to be incompressible, dry, cohesionless and of constant density ρ. It follows that the mass and momentum balance equations reduce to

$$\nabla \cdot \mathbf{v} = 0, \qquad (2.19)$$

$$\rho \left\{ \frac{\partial \mathbf{v}}{\partial t} + \nabla \cdot (\mathbf{v} \otimes \mathbf{v}) \right\} = -\nabla \cdot \mathbf{p} + \rho \mathbf{g}, \qquad (2.20)$$

where $\mathbf{v}$ is the velocity, $\mathbf{p}$ is the pressure tensor, $\mathbf{g}$ is the gravitational acceleration, $\partial/\partial t$ indicates the time derivative, ∇ the gradient operator and $\otimes$ the tensor product. The granular material is supposed to satisfy a Mohr-Coulomb yield criterion. The relationship between internal shear stress $\mathbf{S}$ and normal pressure N can be written as

$$|\mathbf{S}| = N \tan\phi, \tag{2.21}$$

where ϕ is the internal angle of friction, which is replaced by δ, the bed friction angle, at the base. The conservation laws (2.19) and (2.20) are completed by kinematic and dynamic boundary conditions at the free surface and at the base of the avalanche. Assume that both surfaces are smooth and orientable, so that they can be described by differentiable implicit functions

$$F^s(\mathbf{x}, t) = 0 \quad \text{and} \quad F^b(\mathbf{x}, t) = 0, \tag{2.22}$$

where the superscripts s and b indicate free surface and base, respectively. The normal vectors at these surfaces, outward pointing from the avalanche body, are

$$\mathbf{n}^s = \frac{\nabla F^s}{\|\nabla F^s\|} \quad \text{and} \quad \mathbf{n}^b = \frac{\nabla F^b}{\|\nabla F^b\|}. \tag{2.23}$$

When $\mathbf{v}^s$ and $\mathbf{v}^b$ indicate the displacement velocities of the free surface and the base, the kinematic boundary equations can be written as

$$\frac{\partial F^s}{\partial t} + \mathbf{v}^s \cdot \nabla F^s = 0, \tag{2.24}$$

$$\frac{\partial F^b}{\partial t} + \mathbf{v}^b \cdot \nabla F^b = 0, \tag{2.25}$$

where it can be seen that only the normal components of the velocity are physically relevant. The free surface of the avalanche is traction free, therefore the dynamical boundary conditions at the free surface is

$$\mathbf{p}^s \mathbf{n}^s = \mathbf{0}, \tag{2.26}$$

where $\mathbf{p}^s$ is the pressure tensor at the free surface. In most situations of practical interest, the basal surface of the avalanche is considered as a fixed topography, hence $\partial F^b/\partial t = 0$. This implies that $\mathbf{u}^b\mathbf{n}^b = 0$ and therefore the basal velocity is tangential to the basal surface. The shear traction is pointing in the opposite direction of $\mathbf{u}^b$ and, since the relation of normal stress and shear stress satisfy a Coulomb dry friction sliding law. The shear stress is equal to the normal basal pressure multiplied by a coefficient of friction $\tan\delta$, where δ is the bed friction angle. Hence the dynamical boundary condition at the base can be expressed as

$$\mathbf{p}^b\mathbf{n}^b - \mathbf{n}^b(\mathbf{n}^b \cdot \mathbf{p}^b\mathbf{n}^b) \quad = \quad \frac{\mathbf{u}^b}{|\mathbf{u}^b|}(\mathbf{n}^b \cdot \mathbf{p}^b\mathbf{n}^b)\tan\delta, \tag{2.27}$$

where $\mathbf{N} = \mathbf{p}^b\mathbf{n}^b$ is the negative traction vector, $\mathbf{n}^b \cdot \mathbf{p}^b\mathbf{n}^b$ is the normal pressure and $\mathbf{S} = \mathbf{p}^b\mathbf{n}^b - \mathbf{n}^b(\mathbf{n}^b \cdot \mathbf{p}^b\mathbf{n}^b)$ is the negative shear traction. This definition of the direction of the shear stress introduces a singularity at $\mathbf{u}^b = \mathbf{0}$, which restricts the model theoretically. In practical modelling of snow avalanches, rockfalls, debris flows or landslides, only the onset and the deposition, when the motion is near the end, are problematic regarding to this restriction.

2.2.2 Curvilinear Coordinates

To model a complex basal topography a curvilinear coordinate system is defined. The coordinate system follows a surface, called reference surface. Note that the choice of the coordinate system is not unique and may be dependent on the resulting surface. In many cases there may be different possibilities. For instance, it could follow the cross-averaged downslope topography or be fitted to a single downslope section of the topography. On this reference surface a function is laid that accounts for the local differences of the real basal topography and the reference surface,

$$z_b = z_b(x, y). \tag{2.28}$$

This function will be referred to as elevation function. The elevation function has to be shallow, which forces a well chosen reference surface and restricts the model on the permissible geometry.
In the following the reference surface is assumed to follow the mean downslope bed topography. An example for a channel-like topography based on such a reference surface is illustrated in Figure 2.4. An orthogonal curvilinear coordinate system $oxyz$ is defined by setting the z-coordinate normal to the reference surface, while x and y are tangential. The x-axis is assumed to follow the thalweg, the y-axis is normal in cross-slope direction. The inclination angle ζ is used to define the reference surface as function of the downslope coordinate x. Note that ζ is independent of the cross-slope coordinate y. To derive the equations, a Cartesian coordinate system O_{XYZ} with unit basis $\mathbf{i}, \mathbf{j}, \mathbf{k}$ is defined. The vector $\mathbf{k}$ is parallel, but in opposite sense to the gravity acceleration vector. $\mathbf{i}$ lies in the vertical plane in which the reference surface varies and $\mathbf{j}$ is perpendicular to both. A simple curvilinear coordinate system

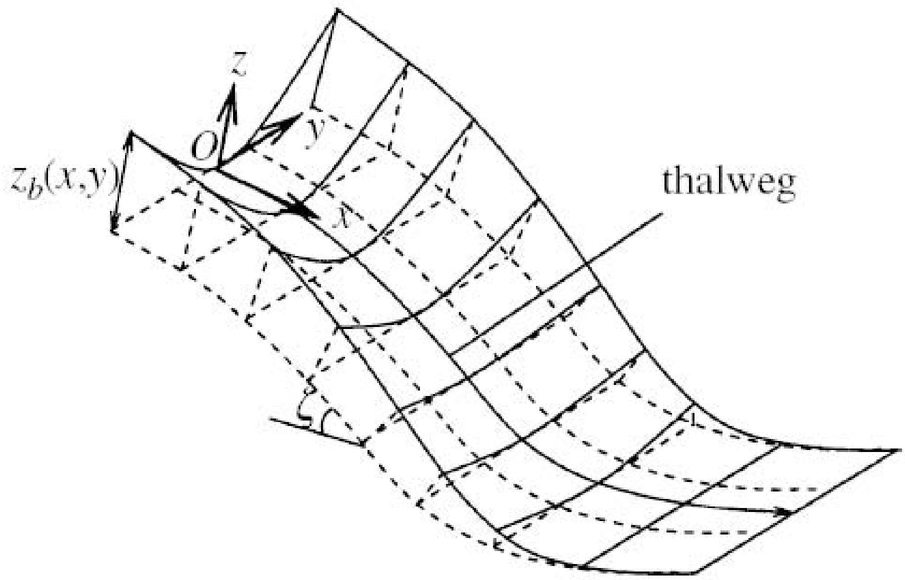

Figure 2.4: The dashed lines show the reference surface, defined by the curvilinear coordinate system $oxyz$. The z-axes is normal to the reference surface, the x-axis follows the curved thalweg and the y-axis lies in the reference surface in cross-slope direction. The downslope inclination angle of the reference surface ζ is measured relative to a horizontal plane. The basal topography (solid lines) is defined by the elevation function $z_b(x, y)$, by superposing the reference surface. Note, that the thalweg is not twisted. Graphic by Chiou [8].

is introduced following Greve et al. [15], which is similar to that of Savage and Hutter [52]. The position vector of a point $\mathbf{r}$ is given by

$$\mathbf{r} = \mathbf{r}^r(x, y) + z\mathbf{n}^r, \tag{2.29}$$

where $\mathbf{r}^r$ is a position vector of the reference surface and $\mathbf{n}^r$ is normal to the reference surface. In the Cartesian coordinate system $OXYZ$ the normal of the reference surface is given by

$$\mathbf{n}^r = \sin\zeta\mathbf{i} + \cos\zeta\mathbf{k}, \tag{2.30}$$

where ζ is the downslope inclination angle of the reference surface, which is the same as the inclination angle of the normal relative to the Z-axis of the Cartesian coordinates. For the convenience of notation the identification $(x, y, z) = (x^1, x^2, x^3)$ is made. These are contravariant components in the curvilinear coordinate system (see, e.g. Bowen and Wang [6],[7] or Klingbeil [30]), and the associated covariant basis vectors, $\mathbf{g}_i$, are given by

$$\mathbf{g}_i = \frac{\partial \mathbf{r}}{\partial x^i}. \tag{2.31}$$

When evaluating the covariant basis vectors of (2.29), it can be seen that the gradiants $\partial \mathbf{r}^r / \partial x^1$ and $\partial \mathbf{r}^r / \partial x^2$ are simply the tangent vectors to the reference surface in x^1- and x^2-direction. Thus choosing the mutually orthogonal tangent vectors with the x-axis in the OXZ plane it follows that $\partial \mathbf{r}^r / \partial x^1 = \cos\zeta \mathbf{i} - \sin\zeta \mathbf{k}$ and $\partial \mathbf{r}^r / \partial x^2 = \mathbf{j}$, so that

$$\begin{aligned} \mathbf{g}_1 &= (1 - \kappa x^3) \cos\zeta \mathbf{i} - \sin\zeta \mathbf{k}, \\ \mathbf{g}_2 &= \mathbf{j}, \\ \mathbf{g}_3 &= \sin\zeta \mathbf{i} + \cos\zeta \mathbf{k}, \end{aligned} \tag{2.32}$$

where κ is the curvature of the reference surface, given by

$$\kappa = -\frac{\partial \zeta}{\partial x^1}. \tag{2.33}$$

The covariant metric coefficients $g_{ij} = \mathbf{g}_i \mathbf{g}_j$ are therefore

$$(g_{ij}) = \begin{pmatrix} (1 - \kappa x^3)^2 & 0 & 0 \\ 0 & 1 & 0 \\ 0 & 0 & 1 \end{pmatrix}. \tag{2.34}$$

The off-diagonal elements of the metric tensor are zero, which implies that these simple curvilinear coordinates are orthogonal. The metric is uniquely defined as long as the z-coordinate is locally smaller than $1/\kappa$. Physically these points correspond to the positions at which the consecutive z-axes, which vary locally, intersect with one another. Provided that the avalanche does not pass through one of these points during motion, the curvilinear coordinates represent a valid coordinate system. The covariant unit vectors are defined as $\mathbf{g}_i^* = \mathbf{g}_i / \sqrt{(g_{ii})}$, where Einstein's summation convention is dropped for bracketed indices, i.e. $\mathbf{g}_1^* = \cos\zeta \mathbf{i} - \sin\zeta \mathbf{k}$, $\mathbf{g}_2^* = \mathbf{j}$ and $\mathbf{g}_3^* = \sin\zeta \mathbf{i} + \cos\zeta \mathbf{k}$. The contravariant basis vectors

$$\begin{aligned} \mathbf{g}^1 &= (\cos\zeta \mathbf{i} - \sin\zeta \mathbf{k}) / (1 - \kappa x^3), \\ \mathbf{g}^2 &= \mathbf{j}, \\ \mathbf{g}^3 &= \sin\zeta \mathbf{i} + \cos\zeta \mathbf{k}, \end{aligned} \tag{2.35}$$

are constructed by $\mathbf{g}_i * \mathbf{g}^j = \delta_i^j$, the Kronecker delta. The associated metric is

$$(g^{ij}) = \begin{pmatrix} \psi^2 & 0 & 0 \\ 0 & 1 & 0 \\ 0 & 0 & 1 \end{pmatrix}, \tag{2.36}$$

where $\psi = 1/(1-\kappa z)$. The Christoffel symbol in orthogonal curvilinear coordinates is defined by

$$\Gamma^k_{lm} = \frac{1}{2} g^{(kk)} (g_{mk,l} + g_{kl,m} - g_{lm,k}). \tag{2.37}$$

For the curvilinear coordinate system (2.34) the Christoffel symbol are given by

$$\Gamma^1 = -\psi \begin{pmatrix} \kappa' z & 0 & \kappa \\ 0 & 0 & 0 \\ \kappa & 0 & 0 \end{pmatrix}, \ \Gamma^2 = \mathbf{0},\ \Gamma^3 = (1-\kappa z) \begin{pmatrix} \kappa & 0 & 0 \\ 0 & 0 & 0 \\ 0 & 0 & 0 \end{pmatrix}, \tag{2.38}$$

where $\kappa' = \partial \kappa / \partial x$.
In order to rewrite the conservation laws (2.19) - (2.20) and their associated boundary conditions (2.24) - (2.27) in the curvilinear coordinate system, the expressions of the gradient of a scalar field and the divergence of a vector and a second order tensor in this coordinate system are required. This can be done by using the ∇-vector, $\nabla = \mathbf{g}^k \frac{\partial}{\partial x^k}$. The gradient of a scalar field F, expressed in the covariant unit base, is then

$$\nabla F = \frac{\partial F}{\partial x^k} g^{(kk)} \sqrt{g_{(kk)}} \mathbf{g}^*_k, \tag{2.39}$$

which reduces to

$$\nabla F = \psi \frac{\partial F}{\partial x} \mathbf{g}^*_1 + \frac{\partial F}{\partial y} \mathbf{g}^*_2 + \frac{\partial F}{\partial z} \mathbf{g}^*_3. \tag{2.40}$$

The divergence of a vector field $\mathbf{v} = u^i \mathbf{g}_i$ is

$$\nabla \cdot \mathbf{v} = \left(\mathbf{g}^k \frac{\partial}{\partial x^k} \right) (u_i \mathbf{g}_i) = u^i_{,k} + u^i \Gamma^k_{ik}. \tag{2.41}$$

The contravariant components of $\mathbf{v}$, u^i are related to the vector's physical components u^{i*}, defined relative to the unit base vectors, by

$$u^i = \frac{u^{i*}}{\sqrt{g_{(ii)}}}. \tag{2.42}$$

Substituting this, together with the Christoffel symbols (2.38), in (2.41) gives

$$\nabla \cdot \mathbf{v} = \frac{\partial (u^{1*}\psi)}{\partial x} + \frac{\partial u^{2*}}{\partial y} + \frac{\partial u^{3*}}{\partial z} - \frac{u^{1*}\kappa' z}{(1-\kappa z)^2} - \frac{u^{3*}\kappa}{1-\kappa z}. \tag{2.43}$$

Similarly, given a second order tensor $\mathbf{p} = p^{ij} \mathbf{g}_i \mathbf{g}_j$ the divergence

$$\nabla \cdot \mathbf{p} = \left(\mathbf{g}^k \frac{\partial}{\partial x^k} \right) (p^{ij} \mathbf{g}_i \mathbf{g}_j) = \left(p^{ij}_{,k} + p^{ij} \Gamma^k_{ik} + p^{kj} \Gamma^i_{jk} \right) \sqrt{g_{(ii)}} \mathbf{g}^*_i. \tag{2.44}$$

The relation of the physical components p^{ij*} are related to the contravariant components by

$$p^{ij} = \frac{p^{ij*}}{\sqrt{g_{(ii)}}\sqrt{g_{(jj)}}}. \tag{2.45}$$

Again this relation and the Christoffel symbols (2.38) are substituted in (2.44), hence

$$\begin{aligned}
\nabla \cdot \mathbf{p} \;=\; & \left(\frac{\partial(p^{11*}\psi)}{\partial x} + \frac{\partial p^{12*}}{\partial y} + \frac{\partial p^{13*}}{\partial z} - \frac{p^{11*}\kappa' z}{(1-\kappa z)^2} - \frac{2p^{13*}\kappa}{1-\kappa z}\right)\mathbf{g}_1^* \\
+ & \left(\frac{\partial(p^{12*}\psi)}{\partial x}) + \frac{\partial p^{22*}}{\partial y} + \frac{\partial p^{23*}}{\partial z} - \frac{p^{12*}\kappa' z}{(1-\kappa z)^2} - \frac{p^{23*}\kappa}{1-\kappa z}\right)\mathbf{g}_2^* \\
+ & \left(\frac{\partial(p^{13*}\psi)}{\partial x} + \frac{\partial p^{23*}}{\partial y} + \frac{\partial p^{33*}}{\partial z} - \frac{p^{13*}\kappa' z}{(1-\kappa z)^2} - \frac{(p^{33*}-p^{11*})\kappa}{1-\kappa z}\right)\mathbf{g}_3^*
\end{aligned} \tag{2.46}$$

2.2.3 Non-dimensional Equations

In order to make laboratory and other similar scaled experiments comparable to natural large scale flows, it is necessary to non-dimensionalize the above presented equations. To achieve this, three length scales, L for longitudinal scaling, H for depth scaling and $1/R$ for the basal curvature, where R is considered as the radius of curvature, are introduced. With gravity g as driving force and relating it to the acceleration of the moving mass implies that typical downslope velocity magnitudes are of order $\sqrt{gL}$ and that time scale is $\sqrt{L/g}$. Velocities normal to the slope are of order $\varepsilon\sqrt{gL}$, where $\varepsilon = H/L$, the aspect ratio of the avalanche. Further, assuming a constant density ρ_0, typical normal pressures at the base of the avalanche are of order $\rho_0 g H$, while typical shear stresses, following the Coulomb dry-friction law, are of order $\rho_0 g H\mu$, where $\mu = \tan\delta_0$ is a coefficient of friction for a typical basal angle of friction δ_0. The curvature of the reference surface is scaled by $1/R$. Next to ε and μ a third non-dimensional parameter $\lambda = L/R$, for the ratio of typical length of the avalanche and the curvature of the slope is introduced. The size of these parameters will be discussed further in the following, as they play a major role in ordering arguments. With all above assumptions, the physical variables are non-dimensionalized using the scalings

$$\begin{aligned}
(x, y)_{dim} &= L\,(x, y)_{non-dim}, \\
(z, F^s, F^b)_{dim} &= \varepsilon L\,(z, F^s, F^b)_{non-dim}, \\
(t)_{dim} &= \sqrt{L/g}\,(t)_{non-dim}, \\
(u, v, w)_{dim} &= \sqrt{Lg}\,(u, v, \varepsilon w)_{non-dim}, \\
(p_{xx}, p_{yy}, p_{zz})_{dim} &= \rho_0 g \varepsilon L\,(p_{xx}, p_{yy}, p_{zz})_{non-dim}, \\
(p_{xy}, p_{xz}, p_{yz})_{dim} &= \rho_0 g \varepsilon L\mu\,(p_{xy}, p_{yz}, p_{yz})_{non-dim}, \\
(\kappa)_{dim} &= \lambda/L(\kappa)_{non-dim},
\end{aligned} \tag{2.47}$$

Applying the scaling (2.47) and the curvilinear transformation rule (2.43) to the mass balance equation (2.19), yields

$$\frac{\partial(u\psi)}{\partial x} + \frac{\partial v}{\partial y} + \frac{\partial w}{\partial z} - \varepsilon\lambda\kappa' z u\psi^2 - \varepsilon\lambda\kappa w\psi = 0, \tag{2.48}$$

where $\psi = 1/(1 - \varepsilon\lambda\kappa z)$, for the non-dimensionalized mass balance equation in curvilinear coordinates. For the momentum balance equations (2.20), the transformation rule for tensors (2.46) has to be applied for the tensors $\mathbf{p}$ and $\mathbf{u} \otimes \mathbf{u}$. Together with scaling (2.47), the non-dimensionalized momentum balance equations in curvilinear coordinates are

$$\begin{aligned}&\tfrac{\partial u}{\partial t} + \tfrac{\partial(u^2\psi)}{\partial x} + \tfrac{\partial(uv)}{\partial y} + \tfrac{\partial(uw)}{\partial z} - \varepsilon\lambda\kappa' z u^2\psi^2 - 2\varepsilon\lambda\kappa uw\psi \\ &\quad = \sin\zeta - \varepsilon\tfrac{\partial(p_{xx}\psi)}{\partial x} - \varepsilon\mu\tfrac{\partial p_{xy}}{\partial y} - \mu\tfrac{\partial p_{xz}}{\partial z} + \varepsilon^2\lambda\kappa' z p_{xx}\psi^2 + 2\varepsilon\lambda\kappa\mu p_{xz}\psi,\end{aligned} \tag{2.49}$$

$$\begin{aligned}&\tfrac{\partial v}{\partial t} + \tfrac{\partial(uv\psi)}{\partial x} + \tfrac{\partial(v^2)}{\partial y} + \tfrac{\partial(vw)}{\partial z} - \varepsilon\lambda\kappa' z uv\psi^2 - \varepsilon\lambda\kappa vw\psi \\ &\quad = \varepsilon\tfrac{\partial p_{yy}}{\partial y} - \varepsilon\mu\tfrac{\partial(p_{xy}\psi)}{\partial x} - \mu\tfrac{\partial p_{yz}}{\partial z} + \varepsilon^2\lambda\kappa'\mu z p_{xy}\psi^2 + \varepsilon\lambda\kappa\mu p_{yz}\psi,\end{aligned} \tag{2.50}$$

$$\begin{aligned}&\varepsilon\left(\tfrac{\partial w}{\partial t} + \tfrac{\partial(uw\psi)}{\partial x} + \tfrac{\partial(vw)}{\partial y} + \tfrac{\partial w^2}{\partial z}\right) - \varepsilon^2\lambda\kappa' z uw\psi^2 - \lambda\kappa(\varepsilon^2 w^2 - u^2)\psi \\ &\quad = -\cos\zeta - \tfrac{\partial p_{zz}}{\partial z} - \varepsilon\mu\tfrac{\partial(p_{xz}\psi)}{\partial x} - \varepsilon\mu\tfrac{\partial p_{yz}}{\partial y} + \varepsilon^2\lambda\kappa'\mu z p_{xz}\psi^2 + \varepsilon\lambda\kappa(p_{zz} - p_{xx})\psi.\end{aligned} \tag{2.51}$$

The free and basal surface are defined by their heights over the reference surface

$$F^s(\mathbf{x}, t) = z - z^s(x, y, t) = 0 \tag{2.52}$$
$$F^b(\mathbf{x}, t) = z^b(x, y, t) - z = 0. \tag{2.53}$$

Applying the scaling (2.47) and the curvilinear transformation rule (2.40), the kinetic boundary conditions (2.22), (2.24) and (2.25) become

$$\frac{\partial z^s}{\partial t} + u^s\psi^s\frac{\partial z^s}{\partial x} + v^s\frac{\partial z^s}{\partial y} - w^s = 0, \tag{2.54}$$
$$\frac{\partial z^b}{\partial t} + u^b\psi^b\frac{\partial z^b}{\partial x} + v^b\frac{\partial z^b}{\partial y} - w^b = 0, \tag{2.55}$$

where $\psi^s = 1/(1-\varepsilon\lambda\kappa z^s)$ and $\psi^b = 1/(1-\varepsilon\lambda\kappa z^b)$. The traction free dynamic boundary conditions for the free surface (2.26) can be transformed in a similar way. Split into downslope, cross-slope and normal components, this yields

$$\begin{aligned} -\varepsilon p^s_{xx}\psi^s\tfrac{\partial z^s}{\partial x} - \varepsilon\mu p^s_{xy}\tfrac{\partial z^s}{\partial y} + \mu p^s_{xz} &= 0, \\ -\varepsilon\mu p^s_{yx}\psi^s\tfrac{\partial z^s}{\partial x} - \varepsilon p^s_{yy}\tfrac{\partial z^s}{\partial y} + \mu p^s_{yz} &= 0, \\ -\varepsilon\mu p^s_{zx}\psi^s\tfrac{\partial z^s}{\partial x} - \varepsilon\mu p^s_{zy}\tfrac{\partial z^s}{\partial y} + p^s_{zz} &= 0. \end{aligned} \tag{2.56}$$

For the Coulomb dry-friction sliding law (2.27), the downslope, cross-slope and normal components are

$$\begin{aligned}
\varepsilon p^b_{xx}\psi^b \tfrac{\partial z^b}{\partial x} + \varepsilon\mu p^b_{xy}\tfrac{\partial z^b}{\partial y} - \mu p^b_{xz} &= \left(\mathbf{n}^b\cdot\mathbf{p}^b\mathbf{n}^b\right)\left(\Delta_b \tfrac{u^b}{|\mathbf{v}^b|}\tan\delta + \varepsilon\psi^b\tfrac{\partial z^b}{\partial x}\right),\\
\varepsilon\mu p^b_{yx}\psi^b \tfrac{\partial z^b}{\partial x} + \varepsilon p^b_{yy}\tfrac{\partial z^b}{\partial y} - \mu p^b_{yz} &= \left(\mathbf{n}^b\cdot\mathbf{p}^b\mathbf{n}^b\right)\left(\Delta_b \tfrac{v^b}{|\mathbf{v}^b|}\tan\delta + \varepsilon\tfrac{\partial z^b}{\partial y}\right),\\
\varepsilon\mu p^b_{zx}\psi^b \tfrac{\partial z^b}{\partial x} + \varepsilon\mu p^b_{zy}\tfrac{\partial z^b}{\partial y} - p^b_{zz} &= \left(\mathbf{n}^b\cdot\mathbf{p}^b\mathbf{n}^b\right)\left(\Delta_b \tfrac{w^b}{|\mathbf{v}^b|}\tan\delta - 1\right),
\end{aligned} \tag{2.57}$$

respectively, where $|\mathbf{v}| = \sqrt{u^2+v^2+\varepsilon w^2}$. The basal normal is given by

$$\mathbf{n}^b = \left(\varepsilon\psi^b\frac{\partial z^b}{\partial x}\mathbf{g}^*_1 + \varepsilon\frac{\partial z^b}{\partial y}\mathbf{g}^*_2 - \mathbf{g}^*_3\right)/\Delta_b, \tag{2.58}$$

and the associated normalization factor is

$$\Delta_b = \sqrt{1+\varepsilon^2(\psi^b)^2\left(\frac{\partial z^b}{\partial x}\right)^2 + \varepsilon^2\left(\frac{\partial z^b}{\partial y}\right)^2}. \tag{2.59}$$

The normal pressure experienced on the basal topography, $\mathbf{n}^b\cdot\mathbf{p}^b\mathbf{n}^b$, occurring in (2.57) takes the non-dimensional curvilinear form

$$\begin{aligned}
\Delta_b^2\left(\mathbf{n}^b\cdot\mathbf{p}^b\mathbf{n}^b\right) &= p^b_{zz} - 2\varepsilon\mu\left(p^b_{xz}\psi^b\frac{\partial z^b}{\partial x} + p^b_{yz}\frac{\partial z^b}{\partial y}\right)\\
&+ \varepsilon^2\left\{p^b_{xx}(\psi^b)^2\left(\frac{\partial z^b}{\partial x}\right)^2 + 2\mu p^b_{xy}\psi^b\frac{\partial z^b}{\partial x}\frac{\partial z^b}{\partial y} + p^b_{yy}\left(\frac{\partial z^b}{\partial y}\right)^2\right\},
\end{aligned} \tag{2.60}$$

which completes the transformation from the coordinate independent form to curvilinear coordinates, using the non-dimensional variables defined in (2.47).

2.2.4 Depth Integration

To simplify the problems from three-dimensional to two-dimensional, a crucial step is the depth integration of the motion equations for the shallow granular material. By defining the depth of the avalanche,

$$h(x,y,t) = z^s - z^b, \tag{2.61}$$

as the height of the material between basal surface z^b and free surface z^s and integrating the mass and momentum balance equations in the direction normal to the reference surface, the equations are reduced by one dimension.

In order to perform the integration procedure, the depth-averaged value of an arbitrary function $f = f(x, y, z, t)$, can be defined by

$$\overline{f} = \frac{1}{h}\int_{z^b}^{z^s} f dz, \tag{2.62}$$

where the overbar is used as notation for a depth-integrated mean value, and will be further used as such. To integrate the mass balance (2.48) through the depth, the Leibnitz rule to interchange the order of integration and differentiation is applied, thus

$$\int_{z^b}^{z^s}\left(\frac{\partial(u\psi)}{\partial x}+\frac{\partial v}{\partial y}+\frac{\partial w}{\partial z}\right)dz = \frac{\partial(h\overline{u\psi})}{\partial x}+\frac{\partial(h\overline{v})}{\partial y}-\left[u\psi\frac{\partial z}{\partial x}+v\frac{\partial z}{\partial y}-w\right]_{z^b}^{z^s} \tag{2.63}$$

Substituting the kinematic boundary equations (2.54) and (2.55) to simplify the right term in (2.63), yields

$$\left[u\psi\frac{\partial z}{\partial x}+v\frac{\partial z}{\partial y}-w\right]_{z^b}^{z^s} = -\frac{\partial h}{\partial t}. \tag{2.64}$$

It follows that the depth-integrated form of the mass balance (2.48) is

$$\frac{\partial h}{\partial t}+\frac{\partial(h\overline{u\psi})}{\partial x}+\frac{\partial(h\overline{v})}{\partial y}-\varepsilon\lambda\kappa' h\overline{zu\psi^2}-\varepsilon\lambda\kappa h\overline{w\psi}=0. \tag{2.65}$$

The depth-integration of the downslope component of the momentum balance (2.49) is done in several steps. Starting with the integration of the first four terms and applying the Leibnitz rule, yields

$$\begin{aligned}
&\int_{z^b}^{z^s}\left(\frac{\partial u}{\partial t}+\frac{\partial(u^2\psi)}{\partial x}+\frac{\partial(uv)}{\partial y}+\frac{\partial(uw)}{\partial z}\right)dz \\
&= \frac{\partial(h\overline{u})}{\partial t}+\frac{\partial(h\overline{u^2\psi})}{\partial x}+\frac{\partial(h\overline{uv})}{\partial y}-\left[u\left(\frac{\partial z}{\partial t}+u\psi\frac{\partial z}{\partial x}+v\frac{\partial z}{\partial y}-w\right)\right]_{z^b}^{z^s} \\
&= \frac{\partial(h\overline{u})}{\partial t}+\frac{\partial(h\overline{u^2\psi})}{\partial x}+\frac{\partial(h\overline{uv})}{\partial y},
\end{aligned} \tag{2.66}$$

since the square-bracketed term is identical zero, due to the kinematic boundary conditions (2.54) and (2.55). The integration of the pressure divergence of (2.49) is done in a similar way, thus

$$\begin{aligned}
&\int_{z^b}^{z^s}\left(\varepsilon\frac{\partial(p_{xx}\psi)}{\partial x}+\varepsilon\mu\frac{\partial p_{xy}}{\partial y}+\mu\frac{\partial p_{xz}}{\partial z}\right)dz \\
&= \varepsilon\frac{\partial(h\overline{p_{xx}\psi})}{\partial x}+\varepsilon\mu\frac{\partial(h\overline{p_{xy}})}{\partial y}-\left[\varepsilon p_{xx}\psi\frac{\partial z}{\partial x}+\varepsilon\mu p_{xy}\frac{\partial z}{\partial y}-\mu p_{xz}\right]_{z^b}^{z^s} \\
&= \varepsilon\frac{\partial(h\overline{p_{xx}\psi})}{\partial x}+\varepsilon\mu\frac{\partial(h\overline{p_{xy}})}{\partial y}+\left(\mathbf{n}^b\cdot\mathbf{p}^b\mathbf{n}^b\right)\left(\Delta_b\frac{u^b}{|\mathbf{v}^b|}\tan\delta+\varepsilon\psi^b\frac{\partial z^b}{\partial x}\right),
\end{aligned} \tag{2.67}$$

where the square-bracketed term is substituted by the dynamic boundary conditions (2.56) and (2.57). The cross-slope and normal components are depth-integrated in exactly the same way as the downslope component. Hence, the downslope, cross-slope and normal components of the momentum balances (2.49) - (2.51) are rewritten as

$$\begin{aligned}
&\tfrac{\partial(h\overline{u})}{\partial t} + \tfrac{\partial(h\overline{u^2\psi})}{\partial x} + \tfrac{\partial(h\overline{uv})}{\partial y} - \varepsilon\lambda\kappa' h\overline{zu^2\psi^2} - 2\varepsilon\lambda\kappa h\overline{uw\psi} \\
&= \; h\sin\zeta - \left(\mathbf{n}^b\cdot\mathbf{p}^b\mathbf{n}^b\right)\left(\Delta_b \tfrac{u^b}{|\mathbf{v}^b|}\tan\delta + \varepsilon\psi^b\tfrac{\partial z^b}{\partial x}\right) \\
&\quad -\varepsilon\tfrac{\partial(h\overline{p_{xx}\psi})}{\partial x} - \varepsilon\mu\tfrac{\partial(h\overline{p_{xy}})}{\partial y} + \varepsilon^2\lambda\kappa' h\overline{zp_{xx}\psi^2} + 2\varepsilon\lambda\kappa\mu h\overline{p_{xz}\psi},
\end{aligned} \tag{2.68}$$

$$\begin{aligned}
&\tfrac{\partial(h\overline{v})}{\partial t} + \tfrac{\partial(h\overline{uv\psi})}{\partial x} + \tfrac{\partial(h\overline{v^2})}{\partial y} - \varepsilon\lambda\kappa' h\overline{zuv\psi^2} - \varepsilon\lambda\kappa h\overline{vw\psi} \\
&= \; -\left(\mathbf{n}^b\cdot\mathbf{p}^b\mathbf{n}^b\right)\left(\Delta_b \tfrac{v^b}{|\mathbf{v}^b|}\tan\delta + \varepsilon\tfrac{\partial z^b}{\partial y}\right) \\
&\quad -\varepsilon\mu\tfrac{\partial(h\overline{p_{xy}\psi})}{\partial x} - \varepsilon\tfrac{\partial(h\overline{p_{yy}})}{\partial y} + \varepsilon^2\lambda\kappa'\mu h\overline{zp_{xy}\psi^2} + \varepsilon\lambda\kappa\mu h\overline{p_{yz}\psi},
\end{aligned} \tag{2.69}$$

$$\begin{aligned}
&\varepsilon\left(\tfrac{\partial(h\overline{w})}{\partial t} + \tfrac{\partial(h\overline{uw\psi})}{\partial x} + \tfrac{\partial(h\overline{vw})}{\partial y}\right) - \varepsilon^2\lambda\kappa' h\overline{zuw\psi^2} - \lambda\kappa h\overline{(\varepsilon^2 w^2 - u^2)\psi} \\
&= \; h\cos\zeta - \left(\mathbf{n}^b\cdot\mathbf{p}^b\mathbf{n}^b\right)\left(\Delta_b \tfrac{\varepsilon w^b}{|\mathbf{v}^b|}\tan\delta - 1\right) \\
&\quad -\varepsilon\mu\tfrac{\partial(h\overline{p_{xz}\psi})}{\partial x} - \varepsilon\mu\tfrac{\partial(h\overline{p_{yz}})}{\partial y} + \varepsilon^2\lambda\kappa'\mu h\overline{zp_{xz}\psi^2} + \varepsilon\lambda\kappa h\overline{(p_{zz} - p_{xx})\psi},
\end{aligned} \tag{2.70}$$

respectively. This completes the depth-integration step. (2.65), (2.68) and (2.69) form the basis of shallow granular flow equations.

2.2.5 Ordering

In natural granular flow events, like snow avalanches, landslides and rock falls, downslope and cross-slope lengths are typically much larger than their normal thickness. Based on this observation the so-called shallowness-assumption

$$\varepsilon = \frac{H}{L} \ll 1 \tag{2.71}$$

is used to reduce the equations (2.65), (2.68) and (2.69) in a rational and consistent way.

For λ, the characteristic ratio between avalanche length L and the radius of curvature of the reference surface $R = 1/\kappa$, it can be assumed that

$$\lambda = \mathcal{O}(\varepsilon^\alpha), \tag{2.72}$$

where $0 < \alpha < 1$. Obviously, the reference surface can vary rapidly in some small regions, resulting in a large local curvature. But for the characteristic basal curvature, an average variation over the whole basal topography has to be considered. Typically, the inclination angle ζ of the starting area of the

avalanche can be assumed in a range of 30° to 45°, while the run out zone has an inclination of less than 20°. Therefore, the assumption $0 < \lambda < 1$ holds for most plausible cases, which justifies (2.72).
The typical basal friction angle δ lies in a range of 20° to 30°, so $0 < \mu = \tan\delta < 1$. Hence,

$$\mu = \mathcal{O}(\varepsilon^{\beta}), \tag{2.73}$$

where $0 < \beta < 1$.
Applying these results to Taylor series expansions of ψ and Δ_b, yields

$$\psi = 1 + \mathcal{O}(\varepsilon^{1+\alpha}), \quad \Delta_b = 1 + \mathcal{O}(\varepsilon^{2}). \tag{2.74}$$

To continue the ordering process, by virtue of the normal component of the momentum balance (2.70), the factor $\mathbf{n}^b \cdot \mathbf{p}^b\mathbf{n}^b$ reduces to

$$\mathbf{n}^b \cdot \mathbf{p}^b\mathbf{n}^b = h\cos\zeta + \lambda\kappa h\overline{u^2} + \mathcal{O}(\varepsilon), \tag{2.75}$$

or ordered by ε^{α}

$$\mathbf{n}^b \cdot \mathbf{p}^b\mathbf{n}^b = h\cos\zeta + \mathcal{O}(\varepsilon^{\alpha}), \tag{2.76}$$

With these gathered ordering arguments for the non-dimensional parameters, the mass balance equation (2.65) can be approximated to first order in the small parameter ε:

$$\frac{\partial h}{\partial t} + \frac{\partial (h\overline{u})}{\partial x} + \frac{\partial (h\overline{v})}{\partial y} = 0 + \mathcal{O}(\varepsilon^{1+\alpha}), \tag{2.77}$$

which takes exactly the same form as in Cartesian coordinates. The momentum balances in downslope (2.68) and cross-slope (2.69) direction reduce to

$$\begin{aligned}
&\frac{\partial (h\overline{u})}{\partial t} + \frac{\partial (h\overline{u^2})}{\partial x} + \frac{\partial (h\overline{uv})}{\partial y} && (2.78)\\
&= h\sin\zeta - \frac{u^b}{|\mathbf{v}|^b} h\tan\delta(\cos\zeta + \lambda\kappa\overline{u^2}) - \varepsilon\frac{\partial (h\overline{p_{xx}})}{\partial x} - \varepsilon\cos\zeta h\frac{\partial z^b}{\partial x} + \mathcal{O}(\varepsilon^{1+\gamma}),\\
&\frac{\partial (h\overline{v})}{\partial t} + \frac{\partial (h\overline{uv})}{\partial x} + \frac{\partial (h\overline{v^2})}{\partial y} && (2.79)\\
&= -\frac{v^b}{|\mathbf{v}|^b} h\tan\delta(\cos\zeta + \lambda\kappa\overline{u^2}) - \varepsilon\frac{\partial (h\overline{p_{yy}})}{\partial y} - \varepsilon\cos\zeta h\frac{\partial z^b}{\partial y} + \mathcal{O}(\varepsilon^{1+\gamma}),
\end{aligned}$$

where $\gamma = \min(\alpha, \beta)$.
The normal component (2.70) reduces to

$$\frac{\partial p_{zz}}{\partial z} = -\cos\zeta + \mathcal{O}(\varepsilon^{\alpha}). \tag{2.80}$$

2.2.6 Closure

Further reduction of (2.78) and (2.79) requires constitutive information about the pressure tensor $\mathbf{p}$ and the velocity vector $\mathbf{v}$. The Savage-Hutter theory assumes a very simple state of stress within the avalanche.
With aid of the Mohr circle, the pressures p_{xx} and p_{yy} can be expressed in terms of the overburden pressure p_{zz}, by defining earth pressure coefficients

$$K_x^b = \frac{p_{xx}^b}{p_{zz}^b}, \quad K_y^b = \frac{p_{yy}^b}{p_{zz}^b}. \tag{2.81}$$

Given the three principal stresses, p_1, p_2 and p_3, one of these, w.l.o.g. p_1, is assumed to lie in cross-slope direction, hence $p_1 = p_{yy}$. The notion that the dominant shearing takes place in downslope direction justifies this assumption.
Further, it is assumed that one of the other principal stresses, p_2 or p_3, equals p_1. This assumption is not justified by any physical argument, but reduces the three-dimensional Mohr circle to a single two-dimensional Mohr circle of stress, as described in Section 2.1. The principle stresses, p_2 and p_3 in the xz-plane are given by

$$p_{2,3} = \frac{1}{2}(p_{xx} + p_{zz}) \pm \frac{1}{2}\sqrt{(p_{xx} + p_{zz})^2 + 4\mu^2 p_{xz}^2}. \tag{2.82}$$

Following the original Savage-Hutter theory, the basal normal pressure equals p_{zz}^b and the shear stress equals $-p_{xz}^b$.
Two Mohr stress circles can be constructed that satisfy both the basal sliding law and the internal yield criterion simultaneously. Therefore, two values are possible for the basal downslope pressure p_{xx}^b, one on the larger circle, where $p_{xx}^b > p_{zz}^b$, and one on the smaller circle, where $p_{xx}^b \leq p_{zz}^b$, which are associated with active and passive stress, respectively. Hence, there are four possible values for the principle stresses p_2^b and p_3^b and consequently also for the basal cross-slope pressure p_{yy}^b.
Following the geometrical arguments of Section 2.1, K_x^b and K_y^b can be constructed as function of the internal and basal angles of frictions by

$$K^b_{x_{act/pass}} = 2\left(1 \mp \sqrt{1 - \cos^2\phi/\cos^2\delta}\right)\sec^2\phi - 1, \tag{2.83}$$

$$(K^{x_{act/pass}}_{y_{act/pass}})^b = \frac{1}{2}\left(K^b_{x_{act/pass}} + 1 \mp \sqrt{(K^b_{x_{act/pass}} - 1)^2 + 4\tan^2\delta}\right), \tag{2.84}$$

which is real if and only if $\delta \leq \phi$.
There is no physical criterion to uniquely determine which value corresponds to which particular deformation. Savage and Hutter [51] made ad hoc definitions that the downslope earth pressure K_x^b was active during a dilatational

motion and passive during a compressional motion and similarly for the cross-slope earth pressure $(K_y^x)^b$, thus

$$K_x^b = \begin{cases} K_{x_{act}} & for \ \frac{\partial u}{\partial x} \geq 0, \\ K_{x_{pass}} & for \ \frac{\partial u}{\partial x} < 0, \end{cases} \tag{2.85}$$

$$K_y^b = \begin{cases} K_{y_{act}}^{x_{act}} & for \ \frac{\partial u}{\partial x} \geq 0 \text{ and } \frac{\partial v}{\partial y} \geq 0, \\ K_{y_{pass}}^{x_{act}} & for \ \frac{\partial u}{\partial x} \geq 0 \text{ and } \frac{\partial v}{\partial y} < 0, \\ K_{y_{act}}^{x_{pass}} & for \ \frac{\partial u}{\partial x} < 0 \text{ and } \frac{\partial v}{\partial y} \geq 0, \\ K_{y_{pass}}^{x_{pass}} & for \ \frac{\partial u}{\partial x} < 0 \text{ and } \frac{\partial v}{\partial y} < 0, \end{cases} \tag{2.86}$$

2.2.7 Model Equations

After the closure step of Section 2.2.6 and the reduction of the balance equations (2.77) - (2.79) by all terms of order $\varepsilon^{1+\gamma}$ and higher, the depth-averaged two-dimensional model equations can be written in vector form as

$$\frac{\partial \mathbf{w}}{\partial t} + \frac{\partial \mathbf{f}(\mathbf{w})}{\partial x} + \frac{\partial \mathbf{g}(\mathbf{w})}{\partial y} = \mathbf{s}(\mathbf{w}), \tag{2.87}$$

where $\mathbf{w}$ denotes the vector of conservative variables, $\mathbf{f}$ and $\mathbf{g}$ represent the transport fluxes in x-, respectively y-direction and $\mathbf{s}$ denotes the source term. They are

$$\begin{aligned} \mathbf{w} &= \begin{pmatrix} h \\ hu \\ hv \end{pmatrix}, & \mathbf{f} &= \begin{pmatrix} hu \\ hu^2 + \beta_x h^2/2 \\ huv \end{pmatrix}, \\ \mathbf{g} &= \begin{pmatrix} hv \\ huv \\ hv^2 + \beta_y h^2/2 \end{pmatrix}, & \mathbf{s} &= \begin{pmatrix} 0 \\ hs_x \\ hs_y \end{pmatrix}, \end{aligned} \tag{2.88}$$

where

$$\beta_x = \varepsilon \cos\zeta K_x^b \tag{2.89}$$

$$\beta_y = \varepsilon \cos\zeta K_y^b \tag{2.90}$$

$$s_x = \sin\zeta - \frac{u}{|\mathbf{u}|}\tan\delta(\cos\zeta + \lambda\kappa u^2) - \varepsilon\cos\zeta\frac{\partial z_b}{\partial x} \tag{2.91}$$

$$s_y = -\frac{v}{|\mathbf{u}|}\tan\delta(\cos\zeta + \lambda\kappa u^2) - \varepsilon\cos\zeta\frac{\partial z_b}{\partial y}. \tag{2.92}$$

Chapter 3

Numerical Methods

Solving the model equations of Chapter 2 analytically is difficult and would require further, unphysical simplification. More appropriate is to solve the equations numerically, by translating the physical problem into a discrete form. This approach ensures to attack the original problem without further assumption. Since the rapid development of computational power in the second half of the 20^{th} century, numerical simulations became popular and many different methods were developed. Most popular are traditional grid based methods. There are two fundamental frames to describe the physical governing equations: the Lagrangian description and the Eulerian description.
The Lagrangian description is a material description. The grid is attached to the material in the entire computation process and moves with the material. The advantages of the Lagrangian description are:

- a relative simple formulation of the equation,
- a flexible mesh, in terms of covering irregularities,
- a relatively small grid size, which only covers the area covered by the material,
- hence, a relatively short computation time,
- it is easily possible to track single points of the material by tracking it's attached grid point.

Since, each node follows it's material point, huge deformations of the material can lead to distorted meshes. The accuracy of the formulation and hence the solution can be heavily deteriorated. Also the time step, which is controlled by the smallest element size, can be become very small, resulting in a slow,

inefficient time progress. In extreme cases it can also lead to a breakdown of the algorithm.
The Eulerian description is a spatial description. The grid is fixed in space and time. The material moves in the grid, without altering it. The features of the Eulerian description are quite opposite to the Lagrangian description:

- the formulation of the equations is more difficult,
- mapping of irregularities in the geometry is generally difficult,
- the mesh has to cover the whole area, where material moves at any time in the computation, at all time steps,
- hence, a relatively large computation time,
- it is difficult to track single points of the material.

But it is able to handle large deformation, since the grid is fixed.
The Savage-Hutter equations for rapidly moving boundary problems of granular flows are hyperbolic equations. An appropriate numerical scheme must handle shock waves, occurring if the velocity of the flow changes from supercritical to subcritical. This can be observed in experiment when the material reaches the run-out zone or obstructions are hit in the slope. The mass decelerates abrupt and a shock wave propagates against flow direction, up the slope. Such shock waves represent discontinuities of the physical quantities.
In the past decades various numerical techniques were applied. Early computations were based on Lagrangian moving mesh finite-difference schemes [13], [14], [24], [31], [52], [66]. These schemes can model the location of avalanches acceptable, but when shocks develop, numerical instabilities arise. An artificial numerical diffusion must be applied to avoid those instabilities, which results in uncontrolled spreading and therefore loss of quality of the solution.
Also in Eulerian integration techniques, if the central difference scheme is employed, numerical instabilities were observed and numerical diffusion must be included. First-order finite-difference schemes, like the first-order upstream scheme, are stable with respect to numerical integration, but the solution is often inaccurate since it becomes smeared (Wang et al. [65]).
Wang and Hutter [64] analyzed other traditional numerical integration techniques. They observed oscillations in areas of high gradients, that are not physically feasible, and also numerical instabilities occurred.
Since neither Lagrangian nor traditional Eulerian finite difference schemes are able to resolve the steep gradients and reproduce the observed front shape of the avalanche, it is necessary to apply other conservative high-resolution numerical techniques.

The development of high-resolution schemes has a long history, see e.g. [36], [57], [62], [68]. Nessyahu and Tadmor [46] introduced a one-dimensional high-resolution approach for flows without source term, named non-oscillatory central (NOC) scheme, which was extended to two dimensions by Jiang and Tadmor [47] and modified by Lie and Noelle [38]. Tai [57] and Tai et al. [60] applied it to the numerical simulation of granular avalanche flows.
Since only cell averages are available, high-resolution schemes can generate unphysical numerical oscillation near discontinuities or areas with steep gradients. An algorithms for cell reconstruction is needed to avoid spurious oscillation. For cell reconstruction, a Total Variation Diminishing (TVD) limiter [20], [56] or Essentially Non-Oscillatory (ENO) [36] scheme is applied, where the Minmod TVD limiter has shown best performance of the reconstruction schemes (Wang et al. [65]).

3.1 NOC Scheme

The two-dimensional NOC scheme uses staggered grids. It is a predictor-corrector method, which consists of two steps. First, the grid point values are predicted by using non-oscillatory reconstruction from the given cell averages. At the second corrector step, the staggered averages are introduced, together with the predicted mid-values. The key feature of this scheme is that the staggered averages at $(x_{p\pm1/2}, y_{p\pm1/2}, t^{n+1})$ are computed by the cell averages at (x_p, y_p, t^n) (see Figure 3.1).

Let $C_{i,j}$ be the cell

$$C_{i,j} = \left\{ (x,y) \middle| |x - x_i| \leq \frac{\Delta x}{2} \quad \text{and} \quad |y - y_j| \leq \frac{\Delta y}{2} \right\}, \tag{3.1}$$

covering (x_i, y_j). A piecewise linear reconstruction of the vector $\mathbf{w}$ from (2.87) for $(x,y) \in C_{i,j}$ is defined by

$$\begin{aligned} \mathbf{w}(x,y,t^n) &= \mathbf{w}^n_{i,j} + (x - x_i)(\frac{\partial \mathbf{w}}{\partial x})^n_{i,j} + (y - y_j)(\frac{\partial \mathbf{w}}{\partial y})^n_{i,j} \\ &= \mathbf{w}^n_{i,j} + (x - x_i)\boldsymbol{\sigma}^x_{i,j} + (y - y_j)\boldsymbol{\sigma}^y_{i,j}, \end{aligned} \tag{3.2}$$

where $\mathbf{w}^n_{i,j}$ is the cell average of $\mathbf{w}$ over $C_{i,j}$ at time t^n. $\boldsymbol{\sigma}^x_{i,j}$ and $\boldsymbol{\sigma}^y_{i,j}$ are the slopes of $\mathbf{w}$ in x-, respectively y-direction, which will be derived by TVD-limiters, see below.

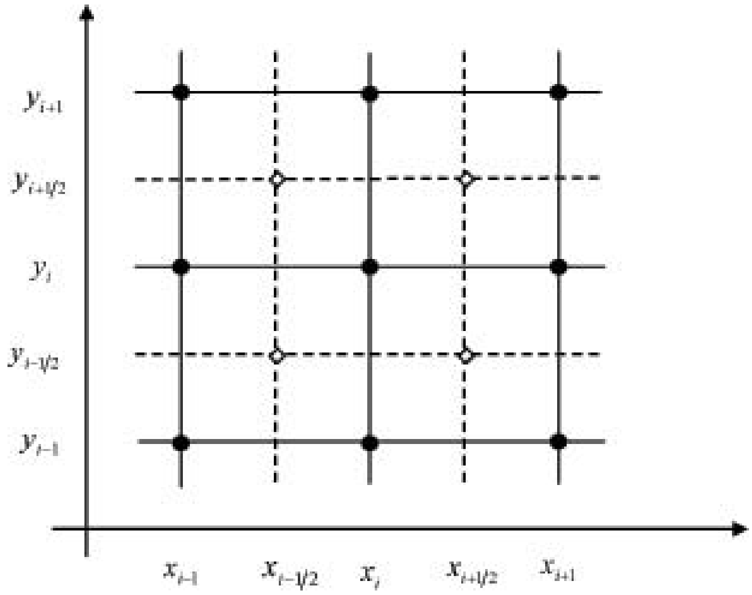

Figure 3.1: Sketch of a staggered grid used in two-dimensional NOC scheme. The staggered averages $(x_{i+1/2}, y_{i+1/2}, t^{n+1})$, marked by $\diamond$, are computed by averaging (x_i, y_i, t), displayed by $\bullet$

To determine the staggered averages over cell $C_{i+1/2,j+1/2}$, integrating (2.87) yields

$$\begin{aligned}
\mathbf{w}^{n+1}_{i+1/2,j+1/2} &= \frac{1}{\Delta x \Delta y} \int_{y_i}^{y_{i+1}} \int_{x_i}^{x_{i+1}} \mathbf{w}(x,y,t^{n+1})\ dx\ dy \\
&= \frac{1}{\Delta x \Delta y} \int_{y_i}^{y_{i+1}} \int_{x_i}^{x_{i+1}} \mathbf{w}(x,y,t^{n})\ dx\ dy \\
&\quad - \frac{1}{\Delta x \Delta y} \int_{t^n}^{t^{n+1}} \int_{y_i}^{y_{i+1}} \left(\mathbf{f}(x_{i+1},y,t) - \mathbf{f}(x_i,y,t)\right) dy\ dt \\
&\quad - \frac{1}{\Delta x \Delta y} \int_{t^n}^{t^{n+1}} \int_{x_i}^{x_{i+1}} \left(\mathbf{g}(x,y_{i+1},t) - \mathbf{g}(x,y_i,t)\right) dx\ dt \\
&\quad + \frac{1}{\Delta x \Delta y} \int_{t^n}^{t^{n+1}} \int_{y_i}^{y_{i+1}} \int_{x_i}^{x_{i+1}} \mathbf{s}(x,y,t)\ dx\ dy\ dt
\end{aligned} \tag{3.3}$$

To integrate the first term in (3.3) the integration domain is divided into four intersecting cells, so

$$\begin{aligned}
&\frac{1}{\Delta x \Delta y} \int_{x_i}^{x_{i+1}} \int_{y_i}^{y_{i+1}} \mathbf{w}(x,y,t^n) dx\ dy \\
&= \frac{1}{\Delta x \Delta y} \Big\{ \int_{y_i}^{y_{i+1/2}} \int_{x_i}^{x_{i+1/2}} \mathbf{w}(x,y,t^n) dx\ dy \\
&\qquad + \int_{y_{i+1/2}}^{y_{i+1}} \int_{x_i}^{x_{i+1/2}} \mathbf{w}(x,y,t^n) dx\ dy \\
&\qquad + \int_{y_i}^{y_{i+1/2}} \int_{x_{i+1/2}}^{x_{i+1}} \mathbf{w}(x,y,t^n) dx\ dy \\
&\qquad + \int_{y_{i+1/2}}^{y_{i+1}} \int_{x_{i+1/2}}^{x_{i+1}} \mathbf{w}(x,y,t^n) dx\ dy \quad \Big\} \\
&= \frac{1}{4} \left\{ \mathbf{w}^n_{i+1/4,j+1/4} + \mathbf{w}^n_{i+1/4,j+3/4} + \mathbf{w}^n_{i+3/4,j+1/4} + \mathbf{w}^n_{i+3/4,j+3/4} \right\},
\end{aligned} \tag{3.4}$$

where

$$\begin{aligned}
\mathbf{w}^n_{i+1/4,j+1/4} &= \mathbf{w}^n_{i,j} + \tfrac{\Delta x}{4}\boldsymbol{\sigma}^x_{i,j} + \tfrac{\Delta y}{4}\boldsymbol{\sigma}^y_{i,j},\\
\mathbf{w}^n_{i+1/4,j+3/4} &= \mathbf{w}^n_{i,j+1} + \tfrac{\Delta x}{4}\boldsymbol{\sigma}^x_{i,j+1} - \tfrac{\Delta y}{4}\boldsymbol{\sigma}^y_{i,j+1},\\
\mathbf{w}^n_{i+3/4,j+1/4} &= \mathbf{w}^n_{i+1,j} - \tfrac{\Delta x}{4}\boldsymbol{\sigma}^x_{i+1,j} + \tfrac{\Delta y}{4}\boldsymbol{\sigma}^y_{i+1,j},\\
\mathbf{w}^n_{i+3/4,j+3/4} &= \mathbf{w}^n_{i+1,j+1} - \tfrac{\Delta x}{4}\boldsymbol{\sigma}^x_{i+1,j+1} - \tfrac{\Delta y}{4}\boldsymbol{\sigma}^y_{i+1,j+1},
\end{aligned} \tag{3.5}$$

The fluxes, second and third term in (3.3) are approximated by second-order rectangular rule for the spacial integral and by midpoint quadrature rule for second-order accuracy of the temporal integral. Therefore,

$$\begin{aligned}
&\tfrac{1}{\Delta x\Delta y}\int_{t^n}^{t^{n+1}}\int_{y_i}^{y_{i+1}} (\mathbf{f}(x_{i+1},y,t)-\mathbf{f}(x_i,y,t))\,dy\;dt\\
&= \tfrac{\Delta t}{2\Delta x}\{\ \mathbf{f}(x_{i+1},y_j,t^{n+1/2})-\mathbf{f}(x_i,y_j,t^{n+1/2})\\
&\qquad +\ \mathbf{f}(x_{i+1},y_{j+1},t^{n+1/2})-\mathbf{f}(x_i,y_{j+1},t^{n+1/2})\ \}\\
&= \tfrac{\Delta t}{2\Delta x}\left\{\mathbf{f}(\mathbf{w}^{n+1/2}_{i+1,j})-\mathbf{f}(\mathbf{w}^{n+1/2}_{i,j})+\mathbf{f}(\mathbf{w}^{n+1/2}_{i+1,j+1})-\mathbf{f}(\mathbf{w}^{n+1/2}_{i,j+1})\right\},
\end{aligned} \tag{3.6}$$

$$\begin{aligned}
&\tfrac{1}{\Delta x\Delta y}\int_{t^n}^{t^{n+1}}\int_{x_i}^{x_{i+1}} (\mathbf{g}(x,y_{j+1},t)-\mathbf{g}(x,y_j,t))\,dx\;dt\\
&= \tfrac{\Delta t}{2\Delta y}\{\ \mathbf{g}(x_i,y_{j+1},t^{n+1/2})-\mathbf{g}(x_i,y_j,t^{n+1/2})\\
&\qquad +\ \mathbf{g}(x_{i+1},y_{j+1},t^{n+1/2})-\mathbf{g}(x_{i+1},y_j,t^{n+1/2})\ \}\\
&= \tfrac{\Delta t}{2\Delta y}\left\{\mathbf{g}(\mathbf{w}^{n+1/2}_{i,j+1})-\mathbf{g}(\mathbf{w}^{n+1/2}_{i,j})+\mathbf{g}(\mathbf{w}^{n+1/2}_{i+1,j+1})-\mathbf{g}(\mathbf{w}^{n+1/2}_{i+1,j})\right\}.
\end{aligned} \tag{3.7}$$

First-order Taylor series expansion in time is used to approximate the values of $\mathbf{w}^{n+1/2}_{i,j}$. From (2.87) the predictor step of the NOC-scheme is derived,

$$\begin{aligned}
\mathbf{w}^{n+1/2}_{i,j} &= \mathbf{w}^n_{i,j} + \tfrac{\Delta t}{2}\left(\tfrac{\partial \mathbf{w}}{\partial t}\right)^n_{i,j}\\
&= \mathbf{w}^n_{i,j} - \tfrac{\Delta t}{2}\left(\tfrac{\partial \mathbf{f}(\mathbf{w})}{\partial t}\right)^n_{i,j} - \tfrac{\Delta t}{2}\left(\tfrac{\partial \mathbf{g}(\mathbf{w})}{\partial t}\right)^n_{i,j} + \tfrac{\Delta t}{2}\mathbf{s}(\mathbf{w}^n_{i,j})\\
&= \mathbf{w}^n_{i,j} - \tfrac{\Delta t}{2}\boldsymbol{\sigma}^f_{i,j} - \tfrac{\Delta t}{2}\boldsymbol{\sigma}^g_{i,j} + \tfrac{\Delta t}{2}\mathbf{s}(\mathbf{w}^n_{i,j}),
\end{aligned} \tag{3.8}$$

where $\boldsymbol{\sigma}^f_{i,j}$ and $\boldsymbol{\sigma}^g_{i,j}$ are the slopes for $\mathbf{f}$ and $\mathbf{g}$, which can also be written by using the corresponding Jacobian.

$$\boldsymbol{\sigma}^f_{i,j} = \left(\frac{\partial \mathbf{f}(\mathbf{w})}{\partial \mathbf{w}}\right)^n_{i,j}\boldsymbol{\sigma}^x_{i,j}, \quad \boldsymbol{\sigma}^g_{i,j} = \left(\frac{\partial \mathbf{g}(\mathbf{w})}{\partial \mathbf{w}}\right)^n_{i,j}\boldsymbol{\sigma}^y_{i,j} \tag{3.9}$$

The integral of the forth term in (3.3) is also approximated by splitting the domain into the four intersecting cells and using the midpoint quadrature rule for second-order accuracy of the temporal integral. This yields

$$\begin{aligned}
&\tfrac{1}{\Delta x\Delta y}\int_{t^n}^{t^{n+1}}\int_{y_i}^{y_{i+1}}\int_{x_i}^{x_{i+1}} \mathbf{s}(x,y,t)dx\;dy\;dt\\
&= \tfrac{\Delta t}{4}\{\ \mathbf{s}(x_{i+1/4},y_{i+1/4},t^{n+1/2})+\mathbf{s}(x_{i+1/4},y_{i+3/4},t^{n+1/2})\\
&\qquad +\ \mathbf{s}(x_{i+3/4},y_{i+1/4},t^{n+1/2})+\mathbf{s}(x_{i+3/4},y_{i+3/4},t^{n+1/2})\ \}\\
&= \tfrac{\Delta t}{4}\{\ \mathbf{s}(\mathbf{w}^{n+1/2}_{i+1/4,j+1/4})+\mathbf{s}(\mathbf{w}^{n+1/2}_{i+1/4,j+3/4})\\
&\qquad +\ \mathbf{s}(\mathbf{w}^{n+1/2}_{i+3/4,j+1/4})+\mathbf{s}(\mathbf{w}^{n+1/2}_{i+3/4,j+3/4})\ \}.
\end{aligned} \tag{3.10}$$

The values $\mathbf{w}^{n+1/2}_{i+1/4,j+1/4}$, $\mathbf{w}^{n+1/2}_{i+1/4,j+3/4}$, $\mathbf{w}^{n+1/2}_{i+3/4,j+1/4}$ and $\mathbf{w}^{n+1/2}_{i+3/4,j+3/4}$ are again determined by virtue of first-order Taylor series expansion in time and space,

$$\begin{aligned}
\mathbf{w}^{n+1/2}_{i+1/4,j+1/4} &= \mathbf{w}^{n+1/2}_{i,j} + \tfrac{\Delta x}{4}\boldsymbol{\sigma}^x_{i,j} + \tfrac{\Delta y}{4}\boldsymbol{\sigma}^y_{i,j},\\
\mathbf{w}^{n+1/2}_{i+1/4,j+3/4} &= \mathbf{w}^{n+1/2}_{i,j+1} + \tfrac{\Delta x}{4}\boldsymbol{\sigma}^x_{i,j+1} - \tfrac{\Delta y}{4}\boldsymbol{\sigma}^y_{i,j+1},\\
\mathbf{w}^{n+1/2}_{i+3/4,j+1/4} &= \mathbf{w}^{n+1/2}_{i+1,j} - \tfrac{\Delta x}{4}\boldsymbol{\sigma}^x_{i+1,j} + \tfrac{\Delta y}{4}\boldsymbol{\sigma}^y_{i+1,j},\\
\mathbf{w}^{n+1/2}_{i+3/4,j+3/4} &= \mathbf{w}^{n+1/2}_{i+1,j+1} - \tfrac{\Delta x}{4}\boldsymbol{\sigma}^x_{i+1,j+1} - \tfrac{\Delta y}{4}\boldsymbol{\sigma}^y_{i+1,j+1}.
\end{aligned} \tag{3.11}$$

In summary, the two-dimensional NOC-scheme consists of the predictor step (3.8) and the staggered corrector step (3.3), by substituting (3.4), (3.6), (3.7) and (3.10). The cell average value at $(x_{i+1/2}, y_{j+1/2}, t^{n+1})$ is given by

$$\begin{aligned}
&\mathbf{w}^{n+1}_{i+1/2,j+1/2}\\
&= \tfrac{1}{4}\left\{\mathbf{w}^n_{i+1/4,j+1/4} + \mathbf{w}^n_{i+1/4,j+3/4} + \mathbf{w}^n_{i+3/4,j+1/4} + \mathbf{w}^n_{i+3/4,j+3/4}\right\}\\
&-\tfrac{\Delta t}{2\Delta x}\left\{\mathbf{f}(\mathbf{w}^{n+1/2}_{i+1,j}) - \mathbf{f}(\mathbf{w}^{n+1/2}_{i,j}) + \mathbf{f}(\mathbf{w}^{n+1/2}_{i+1,j+1}) - \mathbf{f}(\mathbf{w}^{n+1/2}_{i,j+1})\right\}\\
&-\tfrac{\Delta t}{2\Delta y}\left\{\mathbf{g}(\mathbf{w}^{n+1/2}_{i,j+1}) - \mathbf{g}(\mathbf{w}^{n+1/2}_{i,j}) + \mathbf{g}(\mathbf{w}^{n+1/2}_{i+1,j+1}) - \mathbf{g}(\mathbf{w}^{n+1/2}_{i+1,j})\right\}\\
&+\tfrac{\Delta t}{4}\{\mathbf{s}(\mathbf{w}^{n+1/2}_{i+1/4,j+1/4}) + \mathbf{s}(\mathbf{w}^{n+1/2}_{i+1/4,j+3/4}) + \mathbf{s}(\mathbf{w}^{n+1/2}_{i+3/4,j+1/4}) + \mathbf{s}(\mathbf{w}^{n+1/2}_{i+3/4,j+3/4})\}.
\end{aligned} \tag{3.12}$$

The slopes $\boldsymbol{\sigma}^x$, $\boldsymbol{\sigma}^y$, $\boldsymbol{\sigma}^f$ and $\boldsymbol{\sigma}^g$ are a question of cell reconstruction. The solution must meet two main criteria. It must be of second-order accuracy to avoid diffusion and, to avoid oscillation, it must fulfill the Total Variation Diminishing (TVD) condition

$$\mathrm{TV}(U^{n+1}) \leq \mathrm{TV}(U^n), \tag{3.13}$$

where $\mathrm{TV}(U^n) = \sum |U^n_{i+1} - U^{n+1}_{i+1}|$ is a measure for the total variation of a one-dimensional variable U at time step n. Methods fulfilling the the TVD condition are called TVD methods. Harten [20] has proven that a tow-sided numerical scheme of the form

$$U^{n+1}_i = U^n_i - C_{i-1/2}(U^n_i - U^n_{i-1}) + D_{i+1/2}(U^n_{i+1} - U^n_i), \tag{3.14}$$

where $C_{i-1/2}$ and $D_{i+1/2}$ are data-dependent expressions fulfilling the conditions

$$0 \leq C_{i-1/2}, \quad 0 \leq D_{i+1/2} \quad \text{and} \quad 0 \leq (C_{i-1/2} + D_{i+1/2}) \leq 1 \quad \forall i \tag{3.15}$$

is a TVD method. For example, the low-order upwind scheme fulfilling a Courant-Friedrichs-Levy condition is a first-order TVD method. To achieve second-order accuracy for smooth solutions, combined with well-resolved discontinuities a high-order scheme F^H, i.e. the Lax-Wendroff method, is described as a modification of a low-order scheme F^L, i.e. the upwind scheme by

$$F^H = F^L + (F^H - F^L). \tag{3.16}$$

The first term of (3.16), F^L, is very diffusive, the second term, $F^H - F^L$, is called anti-diffusive (Selby [56]), it captures discontinuities. Introducing a flux-limiter ϕ_i allows to define a method with second-order accuracy for smooth regions and fulfilling the TVD condition near to discontinuities

$$F^H = F^L + \phi_i(F^H - F^L). \tag{3.17}$$

ϕ_i is chosen near unity if the data is smooth and near zero if near to discontinuities. The description can be done in various ways. One possibility is to introduce the ratio of consecutive gradients as a measure of smoothness,

$$\theta_i = \frac{U_i^n - U_{i-1}^n}{U_{i+1}^n - U_i^n} \tag{3.18}$$

and to describe ϕ_i as a function of this ratio

$$\phi_i = \phi(\theta_i) \tag{3.19}$$

The most applicable limiter for the Savage-Hutter model is the so-called Minmod limiter

$$\phi^{\text{Minmod}}(\theta) = \max(0, \min(1, \theta)), \tag{3.20}$$

as shown by Wang et al. [65].
The one-dimensional slope limiter is then introduced by

$$\sigma_i = \left(\frac{U_{i+1}^n - U_i^n}{\Delta x} \right) \tag{3.21}$$

To ensure a smooth piecewise polynomial reconstruction of the cell averages, the Courant-Friedrichs-Levy (CFL) condition must be fulfilled, thus

$$\Delta t \max \left(\frac{|c_x^{max}|}{\Delta x}, \frac{|c_y^{max}|}{\Delta y} \right) < \frac{1}{2}, \tag{3.22}$$

where c_x^{max} and c_y^{max} are the maximum wave speeds in x- and y-direction. They are

$$\begin{aligned} c_x^{max} &= \max_{\forall i,j} \left(|u_{i,j}| + \sqrt{(\beta_x)_{i,j}\ h_{i,j}} \right), \\ c_y^{max} &= \max_{\forall i,j} \left(|v_{i,j}| + \sqrt{(\beta_y)_{i,j}\ h_{i,j}} \right), \end{aligned} \tag{3.23}$$

for all $h_{i,j} \neq 0$.

Chapter 4

Interaction between Granular Flow and Obstruction

For engineers building avalanche protection systems, the interaction of snow avalanches and the built defensive structures is one of the most important issues in avalanche dynamics. Such defense structures are of different shape and are built for different purpose. Smaller breaking dams are placed in the slope to absorb energy. Catchment and deflection dams are usually built in the runout zone to protect facilities. Of special interest are forces acting on the building, volume of the retained mass and the impact on the size of the run out area.
The interaction of moving avalanches and dams can not entirely modeled numerically and theoretically nowadays. Scientists are currently working on this topic, but no model is able to cover the interaction satisfactorily, yet.
First approaches to adjust the Savage-Hutter model to implement dams were done by Tai et al. [58] and Gray et al. [12]. Chiou et al. [9] continued their work and tested different kind of obstacles. In her dissertation [8], Chiou documented various experimental and numerical simulations. Several simulations within this work will refer to these experiments. These models use the elevation function (2.28) to add obstacles to the slope.
Continuum mechanic approaches like the Savage-Hutter theory are only useful to simulate shallow, dense flows. Material overflowing the dam becomes airborne and does not fulfill these restrictions anymore. Jets were observed in experiments and described by simple models, e.g. by Hákonardóttir et al. [16], [19].
A totally different approach is the use of Discrete Element Methods (DEM), see e.g. Teufelsbauer et al. [61]. The material consists of balls which interact with one another while moving down the slope. The advantage is the fully three-dimensional calculation, which allows deep insight into the event and

the implementation of dams. Also airborne is covered by such models.
In this chapter, the experiments performed and documented by Chiou [8] are introduced in the first section.
In the second section, the continuum mechanical model, introduced in Chapter 2, is used to simulate these experiments as done by Chiou [8]. Also weaknesses of this method are discussed.
The third section focuses on Discrete Element Methods as an alternative to the continuum mechanical approach. The same experiments were simulated by Teufelsbauer et al. [61] by using the commercial software PFC3d.
The last section contains a summery of the achieved results.

4.1 Experimental Set-up

To validate the Savage-Hutter theory, experiments, done by Chiou in the laboratory of the TU Darmstadt are simulated numerically. The experiments were described and documented in her dissertation [8].

Figure 4.1: Set-up of the experiment in the laboratory in Darmstadt, by Chiou [8]

The chute (see photograph by Chiou [8] in Figure 4.1) was in total 1915 mm long. It had an inclined upper part. The inclination angle of the upper part could be set to 30°, 40°, 45° or 50°. Depending on the angle the inclined slope was between 930 mm and 939 mm long. The lower part was a 835 mm long plane runout zone. Both parts were connected by a constantly curved transition zone. The granular material was firstly stored in a cap, which could be quickly opened by pulling a rope to release the mass. Chiou used two kinds of caps. The first one, a hemisphere of radius 100 mm was called High-Cap. The second one, called Shallow-Cap, was the top part of a hemisphere of radius 238, where the bottom-radius was 158 mm and the height was 60 mm. Alternatively, a vertically oriented silo, with a gate 180 mm from the top edge of the chute, was used. The opening height of the gate could be varied from 3, 6, 9, 12, 15 to 18 mm. The material was released by quickly lifting the confining plate. This silo was designed to produce a nearly uniform flow with mass evenly distributed over the whole width. Three different dry, granular materials: Quartz, Yellow-Sand and Vestolen, were used, respectively. The material properties are listed in Table 4.1.

Table 4.1: Material properties of the three different granular materials: d is the mean grain diameter, ρ the mass density, M_1 the mass of granular material for High-Cap, M_2 the mass of granular material for Shallow-Cap, ϕ the internal friction angle and δ the basal friction angle

	d (mm)	ρ (kg/m^3)	M_1 (kg)	M_2 (kg)	ϕ	δ
Quartz	5	1639	2.95	3.69	40°	28°
Yellow-Sand	fine	1661	2.99	3.75	33°	27°
Vestolen	4	639	1.15	1.41	37°	24°

Obstacle could be fixated at three different positions of the chute, $P_1 =$ 650 mm, the distance between the first possible position of the obstacle and the upper edge of the inclined plane, $P_2 = 730$ mm and $P_3 = 810$ mm, the distances for the second and third position. Chiou documented two classes of obstacles. Small rectangular Plexiglas plates of different sizes were placed perpendicular to the slope to model walls. The second kind of used obstacles were tetrahedral wedges, with an equilateral triangle as base, lying in the slope with one vertex in the center line pointing up the slope.
For recording of the experiments a CCD camera and two flashes were used. A digital video camera was used as synchronizer and for recording the entire flow motion. A clock was placed on the chute to identify the time in each frame.

4.2 Numerical Simulation by means of Savage-Hutter Model

The continuum mechanical approach is based on the Savage-Hutter equations presented in Chapter 2. There are two material parameters to be determined. Computational results indicate that the geometry of the flow is not very sensitive to the alteration of the internal friction angle ϕ, see Wang et al. [65]. For laboratory experiments, it can be measured from a conical pile of granular material built on horizontal plane.

The determination of the dynamic bed friction angle δ follows the common suggestion to measure the static bed friction angle and reduce it by 4° [22], [23]. In all following calculations both parameters are assumed to be constant values according to Table 4.1.
The two non-dimensional parameters ε and λ of (2.87) are chosen to be unity. This does not conflict the assumption that these two non-dimensional parameters should be small. It indicates only the same length scale is employed in the downflow and cross-slope direction and for the radius of the curvature.
The elevation function $z_b(x, y)$ is used to implement obstructions like dams. Physically, this implementation will cause large errors, especially for high obstructions. The obstructions are only implemented as local height differences in the basal topography. Other physical variables are not considered at all. From (2.91) and (2.92) it becomes obvious that only spatial derivatives of the elevation function, $\partial z_b/\partial x$ and $\partial z_b/\partial y$ enter the model equations. In the most extreme case of steep walls, these terms may be non-zero only in very few grid points. The less steep the gradient, the more grid points are affected and the better the quality of the results. Originally the elevation function was implemented to model channels, with relatively smooth gradients, mainly in cross slope direction.

4.2.1 Granular Flows past Tetrahedral Obstructions

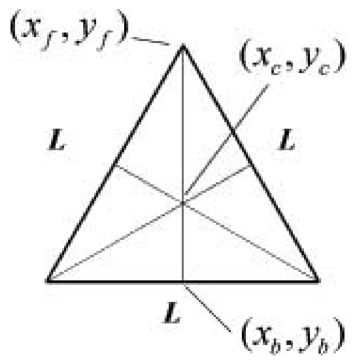

Figure 4.2: Sketch of a ground view of a tetrahedra.

The used tetrahedra has an equilateral basis with edge length L and body height H. Let $X_f = (x_f, y_f)$ be the front vertex of the tetrahedra, lying in the basal triangle, pointing up the slope, see Figure 4.2. $X_b = (x_b, y_b)$ is the center of the back edge and $X_c = (x_c, y_c)$ is the center of the basal triangle above which the top vertex (not shown in the figure) lies. Since the tetrahedra is placed symmetrically regarding the x-coordinate,

$$y_f = y_b = y_c. \tag{4.1}$$

By means of geometric properties of equilateral triangles,

$$\begin{aligned} x_b &= x_f + \frac{\sqrt{3}L}{2}, && (4.2) \\ x_c &= x_f + \frac{L}{\sqrt{3}}. && (4.3) \end{aligned}$$

The tetrahedra enters the model by the derivatives of the elevation function, $\partial z_b/\partial x$ and $\partial z_b/\partial y$, which are prescribed as follows,

$$\frac{\partial z_b(x,y)}{\partial x} = \begin{cases} 0 & \text{for} \quad \{(x,y)|x+\sqrt{3}y < x_f+\sqrt{3}y_f\} \cup \\ & \phantom{\text{for}} \quad \{(x,y)|x-\sqrt{3}y < x_f-\sqrt{3}y_f\} \cup \\ & \phantom{\text{for}} \quad \{(x,y)|x > x_b\}, \\ \frac{\sqrt{3}H}{L} & \text{for} \quad \{(x,y)|x+\sqrt{3}y > x_f+\sqrt{3}y_f\} \cap \\ & \phantom{\text{for}} \quad \{(x,y)|\sqrt{3}x+y < \sqrt{3}x_f+y_f+L\} \cap \\ & \phantom{\text{for}} \quad \{(x,y)|y < y_f\}, \\ \frac{\sqrt{3}H}{L} & \text{for} \quad \{(x,y)|x-\sqrt{3}y > x_f-\sqrt{3}y_f\} \cap \\ & \phantom{\text{for}} \quad \{(x,y)|\sqrt{3}x-y < \sqrt{3}x_f-y_f+L\} \cap \\ & \phantom{\text{for}} \quad \{(x,y)|y \geq y_f\}, \\ -\frac{2\sqrt{3}H}{L} & \text{for} \quad \{(x,y)|\sqrt{3}x+y > \sqrt{3}x_f+y_f+L\} \cap \\ & \phantom{\text{for}} \quad \{(x,y)|\sqrt{3}x-y > \sqrt{3}x_f-y_f+L\} \cap \\ & \phantom{\text{for}} \quad \{(x,y)|x < x_b\}, \\ \frac{\sqrt{3}H}{L} & \text{for} \quad \{(x,y)|y = y_f\} \cap \\ & \phantom{\text{for}} \quad \{(x,y)|x \in [x_f, x_c]\} \\ \frac{\sqrt{3}H}{2L} & \text{for} \quad \{(x,y)|x+\sqrt{3}y = x_f+\sqrt{3}y_f\} \cap \\ & \phantom{\text{for}} \quad \{(x,y)|x \in]x_f, x_b]\}, \\ \frac{\sqrt{3}H}{2L} & \text{for} \quad \{(x,y)|x-\sqrt{3}y = x_f-\sqrt{3}y_f\} \cap \\ & \phantom{\text{for}} \quad \{(x,y)|x \in]x_f, x_b]\}, \\ -\frac{\sqrt{3}H}{2L} & \text{for} \quad \{(x,y)|\sqrt{3}x+y = \sqrt{3}x_f+y_f+L\} \cap \\ & \phantom{\text{for}} \quad \{(x,y)|x \in]x_c, x_b]\}, \\ -\frac{\sqrt{3}H}{2L} & \text{for} \quad \{(x,y)|\sqrt{3}x+y = \sqrt{3}x_f+y_f+L\} \cap \\ & \phantom{\text{for}} \quad \{(x,y)|x \in]x_c, x_b]\}, \\ -\frac{\sqrt{3}H}{L} & \text{for} \quad \{(x,y)|x = x_f+\sqrt{3}L/2\} \cap \\ & \phantom{\text{for}} \quad \{(x,y)|y \in]y_f-L/2, y_f+L/2[\}, \end{cases} \tag{4.4}$$

$$\frac{\partial z_b(x,y)}{\partial y} = \begin{cases} 0 & \text{for} \quad \{(x,y)|x+\sqrt{3}y < x_f + sqrt3y_f\} \cup \\ & \quad \{(x,y)|x-\sqrt{3}y < x_f - \sqrt{3}y_f\} \cup \\ & \quad \{(x,y)|x > x_b\}, \\ \frac{3H}{L} & \text{for} \quad \{(x,y)|x+\sqrt{3}y > x_f + \sqrt{3}y_f\} \cap \\ & \quad \{(x,y)|\sqrt{3}x + y < \sqrt{3}x_f + y_f + L\} \cap \\ & \quad \{(x,y)|y < y_f\}, \\ -\frac{3H}{L} & \text{for} \quad \{(x,y)|x-\sqrt{3}y > x_f - \sqrt{3}y_f\} \cap \\ & \quad \{(x,y)|\sqrt{3}x - y < \sqrt{3}x_f - y_f + L\} \cap \\ & \quad \{(x,y)|y > y_f\}, \\ 0 & \text{for} \quad \{(x,y)|\sqrt{3}x + y > \sqrt{3}x_f + y_f + L\} \cap \\ & \quad \{(x,y)|\sqrt{3}x - y > \sqrt{3}x_f - y_f + L\} \cap \\ & \quad \{(x,y)|x < x_b\}, \\ 0 & \text{for} \quad \{(x,y)|y = y_f\} \cap \\ & \quad \{(x,y)|x \in [x_f, x_c]\} \\ \frac{3H}{2L} & \text{for} \quad \{(x,y)|x+\sqrt{3}y = x_f + \sqrt{3}y_f\} \cap \\ & \quad \{(x,y)|x \in]x_f, x_b]\}, \\ -\frac{3H}{2L} & \text{for} \quad \{(x,y)|x-\sqrt{3}y = x_f - \sqrt{3}y_f\} \cap \\ & \quad \{(x,y)|x \in]x_f, x_b]\}, \\ \frac{3H}{2L} & \text{for} \quad \{(x,y)|\sqrt{3}x + y = \sqrt{3}x_f + y_f + L\} \cap \\ & \quad \{(x,y)|x \in]x_c, x_b]\}, \\ -\frac{3H}{2L} & \text{for} \quad \{(x,y)|\sqrt{3}x + y = \sqrt{3}x_f + y_f + L\} \cap \\ & \quad \{(x,y)|x \in]x_c, x_b]\}, \\ 0 & \text{for} \quad \{(x,y)|x = x_f + \sqrt{3}L/2\} \cap \\ & \quad \{(x,y)|y \in]y_f - L/2, y_f + L/2[\}, \end{cases} \tag{4.5}$$

Note that the derivatives of z_b are not defined for the edges. They are defined by averaging the derivatives of the intersecting planes.

Figure 4.3 shows a comparison of experiment (left side) and theoretical prediction (right side) for a tetrahedra using the silo for a uniform flow performed by Chiou [8]. At the given time step the flow already formed its steady state. As long as a uniform flow is provided the shown shape is not changed. The flowing mass is split into two parts by the tetrahedra. Since the obstruction is symmetric regarding to the cross-slope center line, also separation is done in a symmetric way. If the obstruction is not high enough to avoid overflowing, the mass is not fully divided but partly overflowing the obstruction. Even if the obstruction is high enough to pretend complete overflow, the mass climbs up at the front of it to some extend before it is deflected to the side. The minimal height necessary to avoid total overflow is called critical height of the obstruction. In Figure 4.3, it can be seen that the numerical results are not satisfactory in many important criteria. The mass overflowing the tetrahedra in the computation goes much higher to the

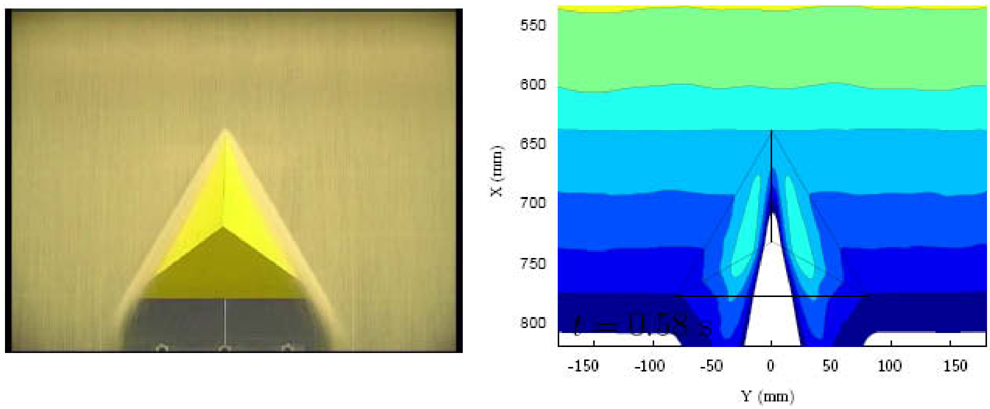

Figure 4.3: Comparison between experiment (left panel) and numerical result (right panel) for a uniform inflow of yellow-sand released from the silo at $x = 180$ mm with opening height 9 mm moving down a chute with inclination angle 45°. A forward-facing tetrahedral wedge with height 80 mm and bottom-side length 160 mm lies in the middle of the inclined plane at P_1 (the downslope coordinate $x = 650$ mm), by Chiou [8].

top of the tetrahedra than does the mass in the experiment. As a result, the area in the back of the obstacle that is free of mass, called granular vacuum, is much narrower than observed. Also estimations of the critical height are not accurate.

4.2.2 Granular Flows past Cuboid Obstructions

Cuboid obstructions, which represent a small wall in the slope, are more difficult to handle than tetrahedral wedges, due to their steep front surface the mass partly depositions in the front of the cuboid. The front side of the tetrahedra has a sharp edge that deflects the impacting mass to the side. The front of the cuboid is a plane, usually orthogonal to the slope plane.

To implement the cuboid obstruction the elevation function is used. Similar to the tetrahedral wedge, the derivatives of the elevation function must be defined. The cuboid obstruction is modeled by a polyhedron, as shown in Figure 4.4. It has a rectangular base with length L_b and width W_b and a rectangular top with length L_t and width W_t, which is parallel to the base rectangular. The center of the top rectangular covers the center of the base plane. The body height of the obstruction is H. The side surface consists of four symmetric trapezoids. Let

$$\Delta_L = \frac{L_b - L_t}{2} \quad \text{and} \quad \Delta_W = \frac{W_b - W_t}{2}, \tag{4.6}$$

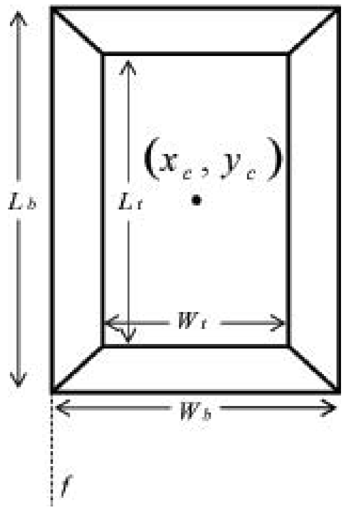

Figure 4.4: Sketch of a ground view of a cuboid obstruction.

then the slope angles α and β of the side planes are given by

$$\tan\alpha = \frac{H}{\Delta_W} \quad \text{and} \quad \tan\beta = \frac{H}{\Delta_L}. \tag{4.7}$$

The center of the base, $X_c = (x_c, y_c)$ lies in the center of the chute and the front line f is orthogonal to the x-axis. Thus, the derivatives of the elevation function, $\partial z_b/\partial x$ and $\partial z_b/\partial y$, are

$$\frac{\partial z_b(x,y)}{\partial x} = \begin{cases} 0 & \text{for} \quad \{(x,y)|W_b/2 < |x-x_c|\} \cup \\ & \quad\ \{(x,y)|L_b/2 < |y-y_c|\}, \\ 0 & \text{for} \quad \{(x,y)|W_b/2 = |x-x_c|\} \cap \\ & \quad\ \{(x,y)|L_b/2 = |y-y_c|\}, \\ 0 & \text{for} \quad \{(x,y)|W_t/2 > |x-x_c|\} \cap \\ & \quad\ \{(x,y)|L_t/2 > |y-y_c|\}, \\ \frac{H}{\Delta_W} & \text{for} \quad \{(x,y)|x \in]x_c - W_b/2, x_c - W_t/2[\} \cap \\ & \quad\ \{(x,y)|\Delta_L x + \Delta_W y < \\ & \quad\quad \Delta_L(x_c - W_b/2) + \Delta_W(y_c + L_b/2)\} \cap \\ & \quad\ \{(x,y)|\Delta_L x - \Delta_W y < \\ & \quad\quad \Delta_L(x_c - W_b/2) - \Delta_W(y_c - L_b/2)\}, \\ -\frac{H}{\Delta_W} & \text{for} \quad \{(x,y)|x \in]x_c + W_t/2, x_c + W_b/2[\} \cap \\ & \quad\ \{(x,y)|\Delta_L x + \Delta_W y > \\ & \quad\quad \Delta_L(x_c + W_b/2) + \Delta_W(y_c - L_b/2)\} \cap \\ & \quad\ \{(x,y)|\Delta_L x - \Delta_W y > \\ & \quad\quad \Delta_L(x_c + W_b/2) - \Delta_W(y_c + L_b/2)\}, \\ \vdots & \end{cases} \tag{4.8}$$

$$
\frac{\partial z_b(x,y)}{\partial x} = \begin{cases}
\vdots & \\
0 \quad \text{for} & \{(x,y)|y \in [y_c - L_b/2, y_c - L_t/2]\} \cap \\
& \{(x,y)|\Delta_L x + \Delta_W y < \\
& \quad \Delta_L(x_c - W_b/2) + \Delta_W(y_c - L_b/2)\} \cap \\
& \{(x,y)|\Delta_L x - \Delta_W y > \\
& \quad \Delta_L(x_c + W_b/2) - \Delta_W(y_c - L_b/2)\}, \\
0 \quad \text{for} & \{(x,y)|y \in [y_c + L_t/2, y_c + L_b/2]\} \cap \\
& \{(x,y)|\Delta_L x + \Delta_W y > \\
& \quad \Delta_L(x_c - W_b/2) + \Delta_W(y_c + L_b/2)\} \cap \\
& \{(x,y)|\Delta_L x - \Delta_W y < \\
& \quad \Delta_L(x_c + W_b/2) - \Delta_W(y_c + L_b/2)\}, \\
\frac{H}{2\Delta_W} \quad \text{for} & \{(x,y)|x \in]x_c - W_b/2, x_c - W_t/2]\} \cap \\
& \{(x,y)|\Delta_L x + \Delta_W y = \\
& \quad \Delta_L(x_c - W_b/2) + \Delta_W(y_c + L_b/2)\}, \\
\frac{H}{2\Delta_W} \quad \text{for} & \{(x,y)|x \in]x_c - W_b/2, x_c - W_t/2]\} \cap \\
& \{(x,y)|\Delta_L x - \Delta_W y = \\
& \quad \Delta_L(x_c - W_b/2) - \Delta_W(y_c - L_b/2)\}, \\
-\frac{H}{2\Delta_W} \quad \text{for} & \{(x,y)|x \in [x_c + W_t/2, x_c + W_b/2[\} \cap \\
& \{(x,y)|\Delta_L x + \Delta_W y = \\
& \quad \Delta_L(x_c + W_b/2) + \Delta_W(y_c - L_b/2)\}, \\
-\frac{H}{2\Delta_W} \quad \text{for} & \{(x,y)|x \in [x_c + W_t/2, x_c + W_b/2[\} \cap \\
& \{(x,y)|\Delta_L x - \Delta_W y = \\
& \quad \Delta_L(x_c + W_b/2) - \Delta_W(y_c + L_b/2)\}, \\
\frac{H}{2\Delta_W} \quad \text{for} & \{(x,y)|x = x_c - W_b/2]\} \cap \\
& \{(x,y)|y \in]y_c - L_b/2, y_c + L_b/2[\}, \\
\frac{H}{2\Delta_W} \quad \text{for} & \{(x,y)|x = x_c - W_t/2]\} \cap \\
& \{(x,y)|y \in]y_c - L_t/2, y_c + L_t/2[\}, \\
-\frac{H}{2\Delta_W} \quad \text{for} & \{(x,y)|x = x_c + W_b/2]\} \cap \\
& \{(x,y)|y \in]y_c - L_b/2, y_c + L_b/2[\}, \\
-\frac{H}{2\Delta_W} \quad \text{for} & \{(x,y)|x = x_c + W_t/2]\} \cap \\
& \{(x,y)|y \in]y_c - L_t/2, y_c + L_t/2[\},
\end{cases}
$$

$$\frac{\partial z_b(x,y)}{\partial y} = \begin{cases} 0 & \text{for} \quad \{(x,y)|W_b/2 < |x-x_c|\} \cup \\ & \quad \{(x,y)|L_b/2 < |y-y_c|\}, \\ 0 & \text{for} \quad \{(x,y)|W_b/2 = |x-x_c|\} \cap \\ & \quad \{(x,y)|L_b/2 = |y-y_c|\}, \\ 0 & \text{for} \quad \{(x,y)|W_t/2 > |x-x_c|\} \cap \\ & \quad \{(x,y)|L_t/2 > |y-y_c|\}, \\ 0 & \text{for} \quad \{(x,y)|x \in [x_c - W_b/2, x_c - W_t/2]\} \cap \\ & \quad \{(x,y)|\Delta_L x + \Delta_W y < \\ & \quad\quad \Delta_L(x_c - W_b/2) + \Delta_W(y_c + L_b/2)\} \cap \\ & \quad \{(x,y)|\Delta_L x - \Delta_W y < \\ & \quad\quad \Delta_L(x_c - W_b/2) - \Delta_W(y_c - L_b/2)\}, \\ 0 & \text{for} \quad \{(x,y)|x \in [x_c + W_t/2, x_c + W_b/2]\} \cap \\ & \quad \{(x,y)|\Delta_L x + \Delta_W y > \\ & \quad\quad \Delta_L(x_c + W_b/2) + \Delta_W(y_c - L_b/2)\} \cap \\ & \quad \{(x,y)|\Delta_L x - \Delta_W y > \\ & \quad\quad \Delta_L(x_c + W_b/2) - \Delta_W(y_c + L_b/2)\}, \\ \frac{H}{\Delta_L} & \text{for} \quad \{(x,y)|y \in]y_c - L_b/2, y_c - L_t/2[\} \cap \\ & \quad \{(x,y)|\Delta_L x + \Delta_W y < \\ & \quad\quad \Delta_L(x_c - W_b/2) + \Delta_W(y_c - L_b/2)\} \cap \\ & \quad \{(x,y)|\Delta_L x - \Delta_W y > \\ & \quad\quad \Delta_L(x_c + W_b/2) - \Delta_W(y_c - L_b/2)\}, \\ -\frac{H}{\Delta_L} & \text{for} \quad \{(x,y)|y \in]y_c + L_t/2, y_c + L_b/2[\} \cap \\ & \quad \{(x,y)|\Delta_L x + \Delta_W y > \\ & \quad\quad \Delta_L(x_c - W_b/2) + \Delta_W(y_c + L_b/2)\} \cap \\ & \quad \{(x,y)|\Delta_L x - \Delta_W y < \\ & \quad\quad \Delta_L(x_c + W_b/2) - \Delta_W(y_c + L_b/2)\}, \\ -\frac{H}{2\Delta_L} & \text{for} \quad \{(x,y)|x \in]x_c - W_b/2, x_c - W_t/2]\} \cap \\ & \quad \{(x,y)|\Delta_L x + \Delta_W y = \\ & \quad\quad \Delta_L(x_c - W_b/2) + \Delta_W(y_c + L_b/2)\}, \\ \frac{H}{2\Delta_L} & \text{for} \quad \{(x,y)|x \in]x_c - W_b/2, x_c - W_t/2]\} \cap \\ & \quad \{(x,y)|\Delta_L x - \Delta_W y = \\ & \quad\quad \Delta_L(x_c - W_b/2) - \Delta_W(y_c - L_b/2)\}, \\ \frac{H}{2\Delta_L} & \text{for} \quad \{(x,y)|x \in [x_c + W_t/2, x_c + W_b/2[\} \cap \\ & \quad \{(x,y)|\Delta_L x + \Delta_W y = \\ & \quad\quad \Delta_L(x_c + W_b/2) + \Delta_W(y_c - L_b/2)\}, \\ -\frac{H}{2\Delta_L} & \text{for} \quad \{(x,y)|x \in [x_c + W_t/2, x_c + W_b/2[\} \cap \\ & \quad \{(x,y)|\Delta_L x - \Delta_W y = \\ & \quad\quad \Delta_L(x_c + W_b/2) - \Delta_W(y_c + L_b/2)\}, \\ \vdots & \end{cases} \tag{4.9}$$

$$\frac{\partial z_b(x,y)}{\partial y} = \begin{cases} & \vdots \\ \frac{H}{2\Delta_W} & \text{for} \quad \{(x,y)|y = y_c - L_b/2]\} \cap \\ & \qquad \{(x,y)|x \in]x_c - W_b/2, x_c + W_b/2[\}, \\ \frac{H}{2\Delta_W} & \text{for} \quad \{(x,y)|y = y_c - L_t/2]\} \cap \\ & \qquad \{(x,y)|x \in]x_c - W_t/2, x_c + W_t/2[\}, \\ -\frac{H}{2\Delta_W} & \text{for} \quad \{(x,y)|y = y_c + L_b/2]\} \cap \\ & \qquad \{(x,y)|x \in]x_c - W_b/2, x_c + W_b/2[\}, \\ -\frac{H}{2\Delta_W} & \text{for} \quad \{(x,y)|y = y_c + L_t/2]\} \cap \\ & \qquad \{(x,y)|x \in]x_c - W_t/2, x_c + W_t/2[\}, \end{cases}$$

where the derivatives for the edges are defined by averaging the intersecting planes, similar to the tetrahedra.

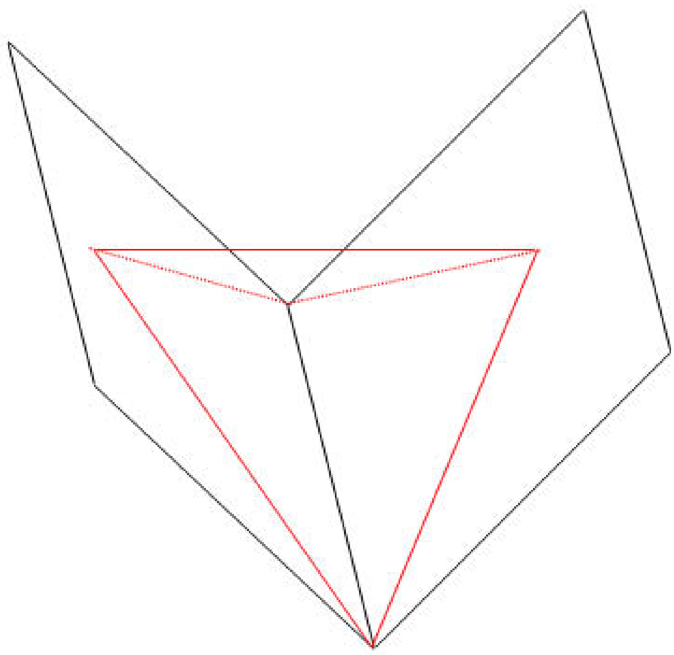

Figure 4.5: Sketch of stored mass between the inclines slope plane of the chute and the orthogonal front plane of the wall. The mass forms a shape close to a tetrahedra (shown in red), where one edge is lying in the intersection of the slope plane and the front plane, the adjacent triangles lie in the slope, respectively front plane. The sixth edge, connecting the two top vertexes of the triangles, is lying horizontal.

The first thing happening, when mass reaches the obstruction, is mass accumulating in the space between the front plane of the cuboid and the

slope. The successive mass is moving along the surface of the stored mass. The stored mass forms a stable shape that is close to a tetrahedra, where one edge is lying in the intersection of the slope plane and the front plane of the obstruction, the adjacent triangles lie in the slope, respectively front plane. The sixth edge connects the two top vertexes of the triangles. It faces the moving mass and can be compared with the front edge of the tetrahedral wedge, as it divides the mass into two parts, by deflecting it to the left or right side. A sketch of the thought tetrahedra is shown in Figure 4.5. In the computations this stable shape of stored mass can not be achieved. For a suitable model, it would be necessary to allow the mass to deposit in the area and successive mass to move along its surface. The present continuum model is only suitable to simulating dynamic processes. No deposition model is implemented. A one-dimensional deposition model was introduced by Tai and Kuo [59], but no two-dimensional deposition model is known so far.
In the used model, the mass is decelerated and the slowly flowing mass in the front of the obstruction is replaced by the following mass. If no successive mass is left, the accumulation is disintegrating slowly. No stable shape is formed, but a quasi steady state can be observed for a long time, which can be considered as a final deposition.
A comparison between experiment and numerical simulation is shown in Figure 4.6.

The computations for cuboid wall elements showed similar weaknesses as for the tetrahedral wedges. Again, the impact of the obstruction is underestimated in computations.
In cases, where the cuboid is sized in the way that the mass is not overflowing it in the experiments, but is almost reaching its top, the error is seen most evidently. The material overflows the obstruction in computations whilst not in experiment. Therefore, also other significant observable features of the flow reveal evident differences between experiments and calculations. The granular vacuum in the back of the obstruction is, if it exists at all, smaller and the shape of the deposit in the runout zone looks different. The model fails if the critical height of the obstruction, the minimal height to avoid overflowing, shall be calculated, which is one of the most important criteria in avalanche protection. For such tasks other more suitable models may be necessary.

In Figure 4.7, the granular flow height on the central symmetric xz-plane is displayed for a given time point after the mass is released at the top of a chute. The model is based on the set-up described in Section 4.1. The chute consists of an inclined plane from $x = 0$ to $x = 251$ and a horizontal part for $x > 295$ with a smooth connection from $x = 251$ to $x = 295$. A cuboid obstruction is considered in the model equations via elevation function (4.8)

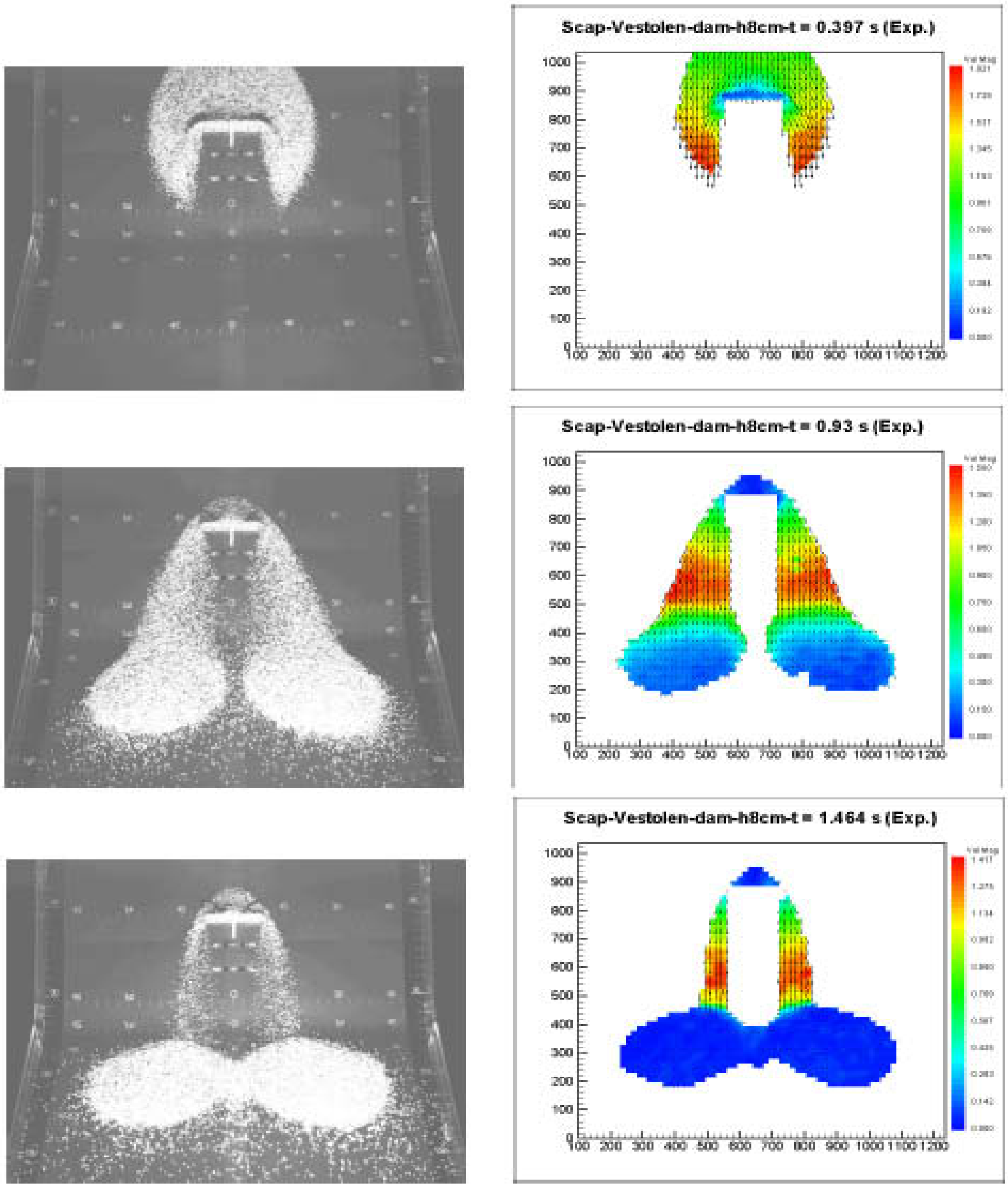

Figure 4.6: Comparison between experiment (left panels) and numerical result (right panels) for a mass of Vestolen released from the Shallow-Cap down a chute with inclination angle 40°. A cuboid dam with height 80 mm and width 160 mm lies in the middle of the inclined plane at position P_1 ($x = 650$ mm). The cylindrical transition zone of the chute starts from 933.5 mm and ends at 1080 mm. The time in each panel from up to down are: 0.397, 0.93, and 1.464 seconds. Experiment and numerical simulation by Chiou [8]

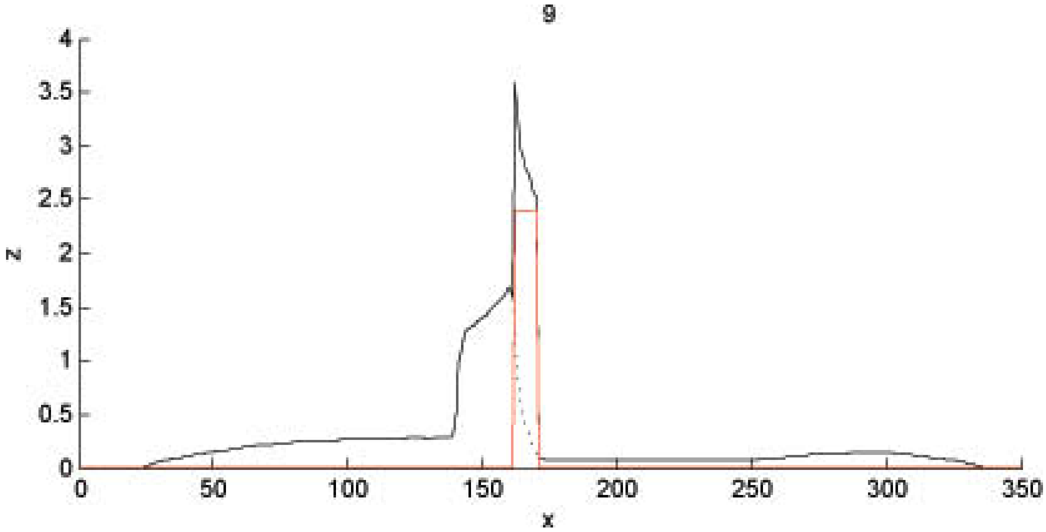

Figure 4.7: Side view on the curve within the xz-plane: x-axis count shows numeration of the grid points, z-axis shows the depth of the material in the corresponding grid point.

and (4.9).
The center of the obstruction is at $x_c = 165$, the height is $H = 2.4$. Until the position $x = 160$ the elevation function is constantly equal to zero. At $x = 161$ it jumps to H. When the obstruction ends at $x = 170$, it jumps back and keeps being zero from $x = 171$ onwards. So the only points where the derivative $\partial z_b / \partial x$ is not zero are at $x \in [160, 161]$ and $x \in [170, 171]$.
The black lines in Figure 4.7 shows the numerical solution. It can be seen that mass is still running down the slope and some mass has accumulated in the front of the obstruction. Some mass already passed the obstructions and accumulates in the run-out zone. The dashed line shows the flow height, when the elevation function is not added to the result. In the area outside of the cuboid, it overlaps the solid black line, which is the height with added elevation function. It could be expected that the mass height jumps to zero at the point it reaches the cuboid if no mass overflows the obstruction. In the numerical result it can be clearly seen that the solution is slowly becoming zero. A significant amount of mass is flowing through (dashed line) or over (solid line) the obstruction. Obviously it is not physically feasible that the mass is running through a solid obstruction. Overflowing may be more feasible, but considering that the mass accumulating in the front is by far not as high as the cuboid, overflowing should not be observed in this case. Also in the corresponding laboratory experiment, hardly any overflowing was observed for this case [8].

In summary, the presented numerical model has two major weaknesses. One is the numerical scheme which tends to smear the solution. The other is the implementation of the obstruction.
A simple way to improve the results is to increase the resolution of the grid, particularly in the vicinity of the obstruction. If more grid points are lying in the front plane of the obstruction, the influence of the obstruction can be better captured. The unphysical smearing of the solution through the obstruction can also be reduced.
The drawback of the increased grid resolution is increased computation time. Since only the area close to the obstruction needs finer grids, while the basic grid is sufficient elsewhere, it seems plausible to increase the resolution only locally. The Adaptive Mesh Refinement Method (AMR), see Chapter 5 may be a reasonable method for this purpose.
Also alternative ways to implement the cuboid are of interest. The slope surface of the obstruction may be implemented by additional planes with own grids for numerical computations. This includes transferring of solutions at the intersection lines. However, singularities at the intersection need to be handled. This method is presented in Chapter 6.

4.3 Discrete Element Model

As alternative to the continuum mechanical approach, a DEM (Discrete Element Method) [11] can be used to simulate the interaction of granular flows and obstructions, as well as to calculate interaction forces (see Section 7.2). In such discontinuum approaches the mass is modeled by discrete particles. Motion and interaction among the particles obey the basic laws of motion. The presented numerical calculations are carried out with the commercial software PFC3d (Version 3.0, Itasca Consulting Group), as performed by Teufelsbauer et al. [61]. PFC3d supports two kind of elements. Arbitrarily sized balls, which are used to simulate the granular material, and wall elements, enabling the creation of topography with static boundary conditions. All elements are characterized by material properties like stiffness and friction. The ball elements have also predefined diameters and densities. Studies on the impact of the diverse parameters can be found in [11], [10], [54], [53], [55], [67], [69].
The interactions between particles and between particles and walls are determined by simple mechanical models, such as springs and dashpots ([10], [32], [42]) and overlapping. Contact forces are decomposed into a normal and a shear component, goverend by the Kelvin-Voigt model. This model consists of an elastic spring and a viscous damper, controlling energy dissipation dur-

ing collisions.
Normal and shear forces are subjected by some restrictions. Tensile normal forces are not allowed and the tangential forces are assumed to obey a Coulomb friction law, which can be expressed by a linear relationship between the normal force F^n and the maximal allowable shear force F^s_{max},

$$F^s_{max} = \mu |F^n|, \tag{4.10}$$

where μ is the friction coefficient. Slip between two adjacent particles occurs, if the shear force is equal to the maximal allowable shear force. In the presented granular flow model internal and basal friction angles determined in laboratory are assigned to calculate the internal and bed friction coefficients. In general, these DEM parameters differ from laboratory measurements. However, in the case of rapid granular flows Coulomb sliding friction is dominated by rotational friction which allows a rough estimation of internal and basal friction.
An additional rotation control is added to the DEM model which allows to describe the rotation behavior of arbitrarily shaped granules with a rough surface by spherical balls ([61], [29], [70]). Without any rolling friction, the friction μ would be not strong enough to prevent the particles from rolling down an incline. As a result, the model would strongly underestimate bed and internal friction angles measured in laboratory. By means of the rotation control it is possible to simulate gravity driven flows of granular material realistically by DEM. The mechanism of rotation control is described in detail by Teufelsbauer et al. [61]. Two parameters, the retarding time λ and the particle contact influence χ have to be identified to describe the rotation behaviour of the particles. The retarding time λ defines the time span which is needed to reduce the angular velocity $\boldsymbol{\omega}$ by the retarding coefficient

$$k_\lambda = \frac{1}{1 + c^\chi} \in [0; 1], \tag{4.11}$$

where c is the number of contacts of a particle to its neighbor particles and χ indicates the sensitivity of the retarding coefficient to the number of contacts. Let Δt be a discrete time step of the DEM calculation, then the particle rotation ω_i^t, in direction $i \in \{1, 2, 3\}$, is reduced to the new rotation

$$\omega_i^{t+1} = k_\lambda^{\Delta t/\lambda} \omega_i^t \tag{4.12}$$

for the following time step. Observations showed that the influence of the shape of angular particles decreases with increased shear velocity. Hence, the rotation model is enhanced by a linear model for the retarding coefficient

$$\lambda = k_v v_s + \lambda_c, \tag{4.13}$$

dependent on a shear velocity v_s, a shear retarding coefficient k_v and an independent retarding time λ_c. This relation allows a more accurate description of the static deposition and dynamic flow of granular material with one mathematical model.
Furthermore, a threshold velocity v_{sr} is defined at which particle rotation is initiated. If the relative particle velocity is below the threshold velocity, the particle rotation is set to zero. This effect can often be observed in laboratory experiments, when an angular particle slides along a smooth inclined. When the particle begins to move it is mostly sliding without rotation. If it has reached a certain (mostly stochastically varying) velocity it begins to rotate. A similar effect can be observed in the deposition process. In general the threshold velocity v_{rs}, the threshold for an angular particle from rolling to pure sliding, is much lower than the threshold v_{sr} from sliding to rolling, due to the kinetic energy of particle spin.
The numerical simulations have proven to be most sensitive to viscous damping and ball rotation (see Figure 4.9). Other material parameters, provided by PFC3d, were significantly less influential. Only if ball rotation is low, shear parameters become important.

In Figure 4.8, it can be seen that the experiment can be reproduced well with PFC3d. The displayed experiment, was executed by Chiou [8] on the chute described in Section 4.1. The photographs in the right panels show experimental results with quartz particles moving down the Plexiglas chute with inclination angle $\zeta = 40°$, interacting with a 80 mm high and 160 mm long Plexiglas wall, positioned at P_1 (650 mm from the upper edge of the chute). The left panels show the results of the simulations performed with PFC3d. A qualitative good agreement can be seen.
It is usually difficult to determine a suitable set of model parameters. Some parameters, such as friction angles, ball diameter or density, can be estimated by using values measured in the laboratory or back analysis [61], [71], others not.
The DEM model has demonstrated to be very sensitive to the viscous damping parameter and the rotation of the particles. Figure 4.9 shows a comparison of the same channel flows, but with free and highly constrained rotation, respectively. The inclination angle of the channel is $\zeta = 45°$. The model is completely three-dimensional. The only difference between the right and the left panels is the ball rotation, which is free in the simulation shown in the right panels, but highly constraint in the simulation shown in the left panels. The significant difference can be seen in the simulated maximal velocity, noted for each shown time step underneath the pictures in Figure 4.9, as well as on the force acting on the back wall of the channel, marked in yellow in

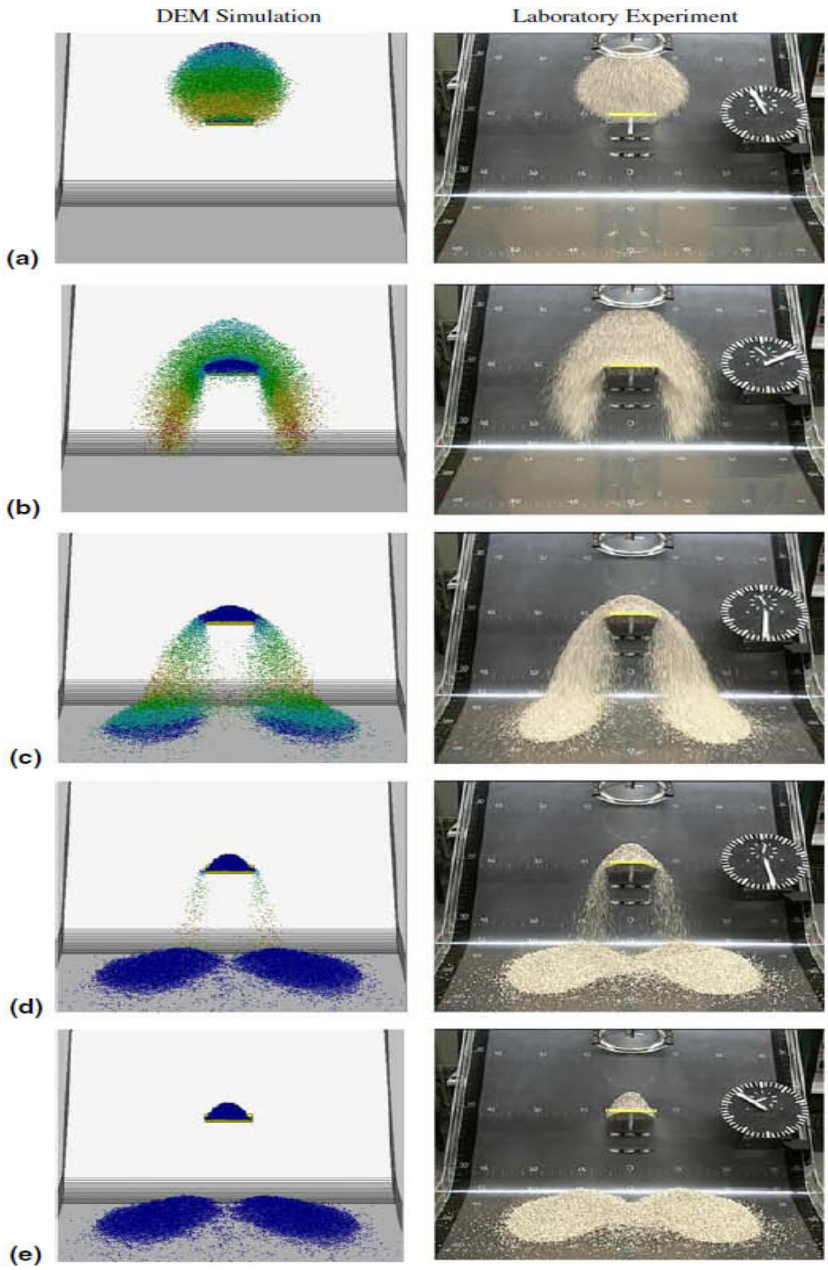

Figure 4.8: Comparison between DEM simulation (left panels) and laboratory experiments (right panels) on a 40° inclination angle of the chute and a 80 mm high and 160 mm long wall at positioned at P_1 ($x = 650$ mm). Time steps: (a) $t = 0.28$ s, (b) $t = 0.56$ s, (c) $t = 0.84$ s, (d) $t = 1.8$ s, (e) $t = 8.2$ s. Laboratory experiments and photographs by Chiou [8], DEM simulations published in H. Teufelsbauer et al. [61]

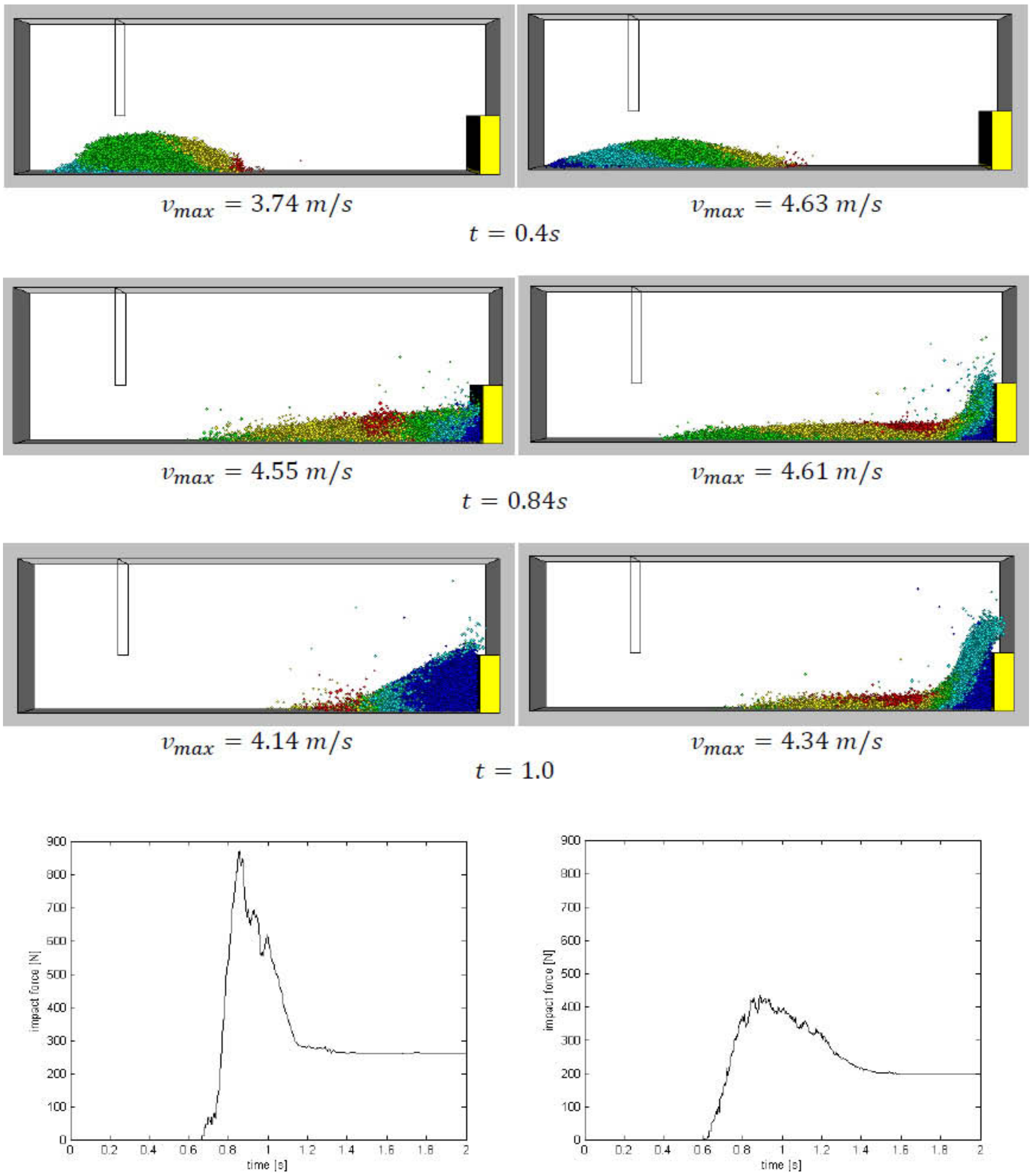

Figure 4.9: Comparison between two DEM simulation for different ball rotation set-ups. For the simulation shown in the left panels, the ball-ball rotation is highly constraint, while it is free in the simulation shown in the right panels. The ball-wall rotation is free for both simulations. The upper three panels show side views on a three-dimensional channel flow at time steps $t = 0.4$ s, $t = 0.84$ s and $t = 1$ s. The bottommost panels show the calculated force acting on the yellow marked back wall over the time of simulation.

the upper six panels of Figure 4.9. The impact force recorded over time is shown in the bottommost panels over the time of simulation.
It is not possible to determine the two parameters, viscous damping and rotation, in laboratory experiments or by some physical relationship. A significant number of test runs is needed to find a good set of parameters. Especially the spread in the run-out area is hard to simulate, due to the shape of the particles, which is spherical in the DEM, while real particles, e.g. quartz, are usually more angular.
Further, it has been seen that a specific set of parameters may not be suitable for another experimental set-up using the same material, but in other chute geometries. A new set of parameters must be identified for each single set-up. Hence, the quality of forecast data obtained by numerical simulations by DEM is not reliable.
Another draw back of the DEM is the large demand on computer memory. Simulations with a realistic number of particles, i.e. when compared to the number of sand particles in the material used in the experiment, need the power of modern super computers. The simulation of natural large scale events is difficult with nowadays computers.

4.4 Conclusions

Continuum mechanical models, such as the presented one based on Savage-Hutter theory, have proven to simulate shallow granular flows appropriately in the past. But they are limited to smooth topographies. If topographies with large gradients are present, as they occur when obstructions like dams are implemented, the quality of the simulation results becomes rather poor. Shallowness assumptions are not valid anymore in front of steep walls, where mass is accumulated and stored and hence the depth becomes comparable with horizontal extension of the flow. For such cases, the flow cannot be considered two-dimensional anymore.
For tetrahedral wedges, which are also used in practice as breaking dams, the shallowness assumption may be still acceptable, since no mass is stored at its front. Still the numerical simulations showed errors, when compared to laboratory experiments.
A disadvantage that all shown continuum mechanical simulations share is the uniform grid. Around the obstructions finer grids are needed, which can be conducted by using Adaptive Mesh Refinement methods. In Chapter 5, this methods is discussed in detail and it will be seen how far the model can be pushed.
As alternative to continuum mechanical models, Discrete Element Methods

(DEM) have been presented. DEM allows a full three-dimensional simulation of the interaction between granular flow and obstruction. It can be used to visualize and understand the complex action at impact. The parameter identification is difficult and critical to achieve good results. Forecast simulations are hardly reliable due to the high sensitivity to the choice of the parameters. Also the demand on computational memory is large, making it difficult to handle large scale simulations.

Chapter 5

Mesh Refinement

5.1 Introduction

For the used finite difference methods the meshes are rectangular grids. In general it can be expected that the finer the grid is, the smaller the numerical error. But finer grids cause higher computation time and demand on memory. Adaptive Mesh Refinement (AMR) is a useful tool to combine high accuracy and low computational cost when finer spatial resolution is necessary only in partial regions. It has been designed by Berger and Oliger [2] and Berger and Colella [1] to solve partial differential equations using finite difference methods. The idea is to refine a basic grid locally, where refinement is needed. For the mayor part of the calculation area the coarse basic grid is used, but the critical areas, where high errors can be expected, are refined.
An AMR mesh can contain various arrays with different refinement levels. Basically, every single grid cell can be arbitrarily refined. But it is useful to cluster them into rectangular grids. Such clusters of cells with the same level of refinement are called patches.
An AMR algorithm consists of two steps. The first step is called prolongation. The grids are adjusted to the current situation. New grids are created if cells need to be refined, grids are deleted if their coarser parent grid is fine enough, others stay as they are.
The second step is called restriction. The equations are solved for each grid. The first grid integrated is the basic grid. Then the others follow level by level. Afterwards the solutions of the finer grids are copied to their parent.

5.1.1 Prolongation

The intention of the prolongation step is to build a tree of grids. It's root is the basic grid, that is laid on the whole computational area. In case

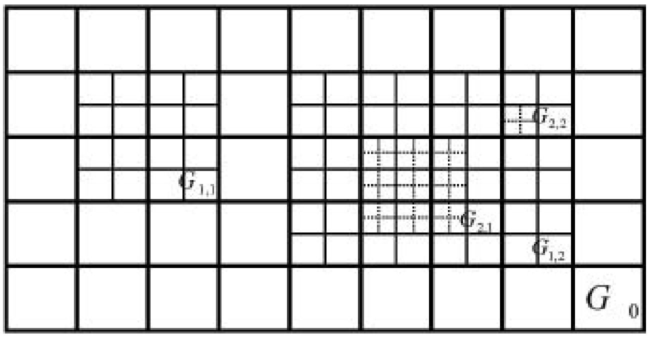

Figure 5.1: An example for a grid tree build in the prolongation step. Starting with the basic grid G_0, a first level of refinement is formed by two new grids $G_{1,1}$ and $G_{1,2}$. $G_{1,2}$ is refined further by the grids $G_{2,1}$ and $G_{2,2}$, which represent a second level of refinement.

of necessity, several areas of this basic grid may be chosen for refinement. Typically the critical cells are tagged and then clustered. Also adjacent untagged cells are joint to the clusters so that rectangular clusters are built. These rectangular clusters of cells are called patches. For each new patch a new grid is generated, with a finer resolution than the basic grid. All these new grids, that originate from the basic grid, build the first level of refinement. Within these patches cells can be tagged, clustered and gathered to patches again, in the same way as for the basic grid. Again new grids are created for the new patches, building a new level of refinement. This procedure is repeated till the necessary fineness is achieved or a maximum of allowed refinement levels is reached. An example for such a resulting grid tree is shown in Figure 5.1.

The refinement ratio of two adjacent levels is always a constant given integer r. So, if the grid spacing at level l is called h_l,

$$r = \frac{h_l}{h_{l+1}}.$$

The decision which cells are refined is made by a previously defined condition. Typically, such conditions are based on error estimations for the numerical solution on each grid point. If the expected error is too large, the adjacent cells are tagged for refinement. The constructed grid trees are saved. Later prolongation steps start with the old trees. But they can be completely reconstructed. New grids can be added and old grids can be deleted, if their parent grid is fine enough.
Whenever a new grid is generated the solutions of its parent grid has to be transfered. For grid points covering grid points of the parent the solution

can be copied. Grid points lying in between, have to be interpolated. The boundary conditions have to be defined as well, either by given external conditions, by adjacent sibling patches, or by interpolation from the parent grid.
Theoretically, the refinement procedure could be run after each coarse time step. In practice this is not very effective, since running the refinement after every time step costs a lot of calculation time. Therefore it is common to run the procedure only every N time steps. The described procedure can be run fully automatically, once the refinement condition is defined. Alternatively the areas of refinements can be declared manually. In many applications, the critical areas, where refinement is needed, are well known and the difficult definition of a condition for an automatic procedure can be avoided.

5.1.2 Restriction

In the restriction step, all grids are integrated. The root grid is integrated first. The finer grids follow in order of level of refinement. After the integration, the more accurate results of the finer patches is copied to their parent. This can be done in several ways. Two common variants are either copying the values of corresponding nodes of the finer grid, or averaging surrounding finer grid values. Note that these methods are generally not conservative. More complex numerical schemes are needed if flux conservation of the model variables at the interfaces, between those coarse cells that are overlapped by fine cells and those that are not is demanded, see e.g. Kurihara et al. [33], Laugier et al. [35] or Perkins et al. [48]. These methods were developed for nested grid calculations, but can be applied for AMR as well. For explicit methods, the time step size is determined by the finest grid. Hence, Berger and Colella [1] used a local time step method to improve the efficiency. For the refinement ratio of the time resolution, they used the same ratio r as for the spatial resolution. While the root level 0 proceeds one time step t_0, the l-th refinement level proceeds r^l time steps

$$t_l = \frac{t_0}{r^l}.$$

With such a convention, once h_0 and t_0 are chosen on the root grid, the corresponding CFL criterion is automatically verified for all grids.

5.2 Avalanche Model with AMR

The AMR technique is applied to the two-dimensional continuum mechanical model, based on Savage-Hutter theory and described in Chapter 2, to

solve the granular flow with obstructions. As Chiou did in her work [8] (see Chapter 4), an obstacle is introduced by using an elevation function (2.28), which accounts for the difference between the basal topography and its reference surface. As explained in Chapter 4, this model has its weaknesses, as the preventability of the obstruction in the computations is not as strong as observed in laboratory experiments. In this chapter, the influence of the grid size will be discussed further. The grid size can be changed in various ways. For all following computations the refinement factors were always multiples of 2 and both dimensions, x- and y-axes, were refined by the same factor. The simplest way of refinement is to refine the whole grid. The disadvantage is obviously huge computational cost.
Refining x and y by a factor n means, n^2 times basic grid points for calculation. Together with space, also time steps have to be shortened by factor n, which sums up to a total theoretical factor of n^3 for computational cost.
A more efficient way to improve calculations is to apply AMR-methods, as described above. Since the critical area is known very well in the present problem, complicated and time consuming algorithms for automatic refinement procedures can be saved.
As observations have shown, the critical area is clearly located at the front side of the obstruction, where the granular flow impinges. Therefore, the rectangular zone to be refined is fixated manually a priori. It covers the the whole front of the obstruction, spreads upwards the slope for a chosen distance, as well as to the left, right and downwards for a much shorter distance. The granular flow moves and reaches the defined zone. A significant part of the mass stays in the defined zone and is stored in the front of the obstruction. Therefore it is reasonable to avoid uneconomic procedures for temporal changes of the refinement zone. Instead the refinement starts right at the beginning with the release of the mass. The refinement zone stays static for the whole computation.
In the restriction step, the solutions of the finer grids are simply copied to their parent grids. The mass is conserved sufficiently in all performed simulations.

5.3 Results

5.3.1 Cuboid Wall

To compare the effect of different grid sizes, a set-up, based on a laboratory experiment executed and described by Chiou [8], was selected. The used chute was in total 1915 mm long and 1100 mm wide. The granular material, Vestolen ($\phi = 37°, \delta = 24°$) in this case, was released from a shallow cap, the top part of a hemisphere of radius 238 mm, where the bottom-radius was 158 mm and the height was 60 mm. The inclination angle ζ of the 933.5 mm long slope was 40° and a 80 mm high and 160 mm wide cuboid obstruction was positioned 650 mm below the upper edge of the slope. In the experiment, the mass just reached the top of the cuboid but only a few single particles flew over it.

To evaluate the effects of the different grids, the maximum heights of the mass on the obstruction (maximum of the solid black curve in Figure 4.7), are compared at a specified time step. The time step is chosen at a moment when a large amount of mass is passing the obstruction, which is short after the front of the granular flow hits the obstruction. This value correlates with the total amount of mass overflowing the obstruction. Since the experiment showed nearly no overflow and the first numerical results showed a significant amount of overflow, one can consider the solution improved if less mass is overflowing, i.e. the calculated maximum on the obstruction becomes smaller.

Another important aspect of the model performance is the calculation time, which is measured on a common 3.2 GHz Pentium 4 processor. The calculation time rises with increased grid resolution that is counteracting the measured maximums when evaluating a grid. As last evaluation factor, visual impressions of the result could be compared. But this is obviously a rather subjective aspect and will not be discussed in detail in this work.

First, the 1915 mm long and 1100 mm wide chute of the experiment is transfered into a 43 units long and 24 units wide computer model chute. All other components of the above described set-up are transfered in the same scale. This chute is covered by a grid, consisting of 431×241 points, with $dx = dy = 0.1$. This grid will be referred to as single resolution grid in the following and can be compared to the grid employed by Chiou [8]. The derivatives of the elevation function (4.8) and (4.9) define the obstruction in the model, with $H = 0.8$, $L_b = 4.8$, $L_t = 4.6$, $W_b = 1$ and $W_t = 0.8$. The cuboid obstruction is placed so that its vertexes locate just at grid points. Since $\Delta_L = \Delta_W = 0.1 = dx = dy$, no grid points are lying in the side walls of the obstruction for this single resolution basic grid.

If the whole grid is refined by a factor two, a 861×481 grid is received, called double resolution grid. Factor four makes a 1321×961 grid, called quadruple resolution grid, and so on. Due to the refinement, grid points lie in the sidewalls of the obstruction. For double resolution grid, with $dx = dy = 0.05$, 1 grid point is added within the side walls along each grid line. For the quadruple resolution grid, with $dx = dy = 0.025$, 3 grid points are added, and so on.

Table 5.1: Comparison of global grid refinement for a granular granular flow hitting a cuboid obstruction. Measured values are: maximum depth of mass on the cuboid at a dimensionless time 9 and calculation time for dimensionless time $t = 24$.

	on cuboid	calculation time
single resolution	1.1144	16 min
double resolution	1.0750	2 h 57 min
quadruple resolution	0.7501	19 h 17 min

Table 5.1 shows a comparison for different global refinements. It can be seen that the amount of mass overflowing the cuboid is decreasing with increased refinement. With the increase of the global refinement, the exploding calculation time makes the need for introducing local refinement obvious.
When refining locally, an area for refinement has to be chosen first. The area of the highest level of refinement has to cover the zone in front of the obstruction and must extend to all sides for some extend. The sizing of the refinement area is a relatively complex question, which will be discussed later. For the first comparison for the effect of local refinement, the area to be refined is chosen relatively arbitrarily. Since for the present case the critical area is known very well, the introduction of an complicated refinement condition for an automatic procedure is avoidable and the refinement zone is defined by hand and kept the same throughout the calculations.
As starting area the front plane of the cuboid shall be chosen. The refinement area is extended by 4 units up the slope, 0.5 to the right and left and 0.2 down the slope, all measured from the bottom of the obstruction. All given size informations concerning refinement in this work refer to the finest used grids. The coarser parent grids have to be slightly larger. In the following cases the parent grids are 0.5 units larger in all directions than their child grid.
One level of refinement makes the fineness of the refined area equivalent to the fineness of the double resolution grid of the global refinement. Two levels of refinements are equivalent to a quadruple resolution and so on.

Table 5.2 makes the effect of AMR visible. There is a clear tendency for decreased overflow with increased refinement. Compared to Table 5.1, the maximum depth on the cuboid is approximately of the same size for equivalent level of refinement, but the calculation time is much shorter, e.g. 56 min for level 2 AMR versus 19 h 17 min for quadruple resolution.
As mentioned earlier the choice of the size of the refinement area was relatively arbitrarily. Another choice does effect the result.

Table 5.2: Comparison of local refinement levels for a granular flow hitting a cuboid obstruction. The given level describes the finest level of refinement used. The grid with finest level of refinement covers a fixed area extending 4 units up the slope, 0.5 units to the right and to the left and 0.2 down the slope, starting from the front plane of the cuboid. Measured values are: maximum depth of mass on the cuboid at a dimensionless time 9 and calculation time for dimensionless time $t = 24$.

level	on cuboid	calculation time
1	0.9410	22 min
2	0.7991	56 min
3	0.5104	8 h 51 min
4	0.4280	56 h 07 min

Table 5.3: Comparison of local refinement areas for a granular flow hitting a cuboid obstruction. The level of refinement is one. The refinement are extends up the slope/to the left/to the right/down the slope, starting at the front plane of the cuboid. Measured values are: maximum depth of mass on the cuboid at a dimensionless time 9 and calculation time for dimensionless time $t = 24$.

refinement area	on cuboid	calculation time
5/1/1/1	0.9445	26 min
5.5/1.5/1.5/1.5	0.9222	26 min
6/2/2/2	0.9078	28 min
6.5/2.5/2.5/2.5	0.8773	33 min

With increased area of refinement, the maximum depth at the top of the cuboid decreases, as Table 5.3 shows. The solutions are improving, while the calculation time is increasing relatively moderately. So optimizing the area of refinement seems to be efficient. But it should be remarked, that the need for higher calculation power increases more rapidly for higher levels of refinement.

In all above computations, the grid was chosen in a way that the corners of the vertexes correspond with grid points. If not, there is, assuming the same grid size, one more point in the front plane of the cuboid, bot none at the edge. For such grid a new basic grid with 421×261 points on a 43 units long and 28 units wide chute. Except for the width of the chute, all used parameters are the same as for the model used before. This grid will be referred to as disarranged grid. The disarranged grid showed improved results when compared to previous computations, on comparable sized grids, as can be seen in Table 5.4.

Table 5.4: Comparison of local refinement levels for a granular flow hitting a cuboid obstruction, on a disarranged 421×261 grid. The given level describes the finest level of refinement used. The grid with finest level of refinement covers a fixed area extending 4 units up the slope, 2 units to the right, to the left and down the slope, starting from the front plane of the cuboid. Measured values are: maximum depth of mass on the cuboid at a dimensionless time 9 and calculation time for dimensionless time $t = 24$.

level	on cuboid	calculation time
1	0.5784	22 min
2	0.4506	2 h 03 min
3	0.3878	11 h 16 min

The used refinement area, starting from the front edge of the cuboid, is extending 4 units up the slope, 2 units to the right, to the left and down the slope, which seems to be an appropriate compromise between computational accuracy and cost. When comparing the results of the disarranged grid to those of the covering grid of the same level of refinement, the results are clearly better, although the resolution is slightly coarser.

In Figure 5.2 a three-dimensional graphic of the result of the numerical simulation can be seen. The grid used is the disarranged grid with three levels of refinement. The measured values are listed in Table 5.4 and are the best of all presented computations. The basic behaviour of accumulation in front of the obstruction and splitting the flow into two flows, which pass the obstruction to the left and to the right, is well captured. Also a shock waves, as observed in experiments, can be seen in front of the obstruction and in the run-out zone.

The amount of mass overflowing the cuboid can be seen better in a two-dimensional ground view, shown in Figure 5.3, where contour lines for the depth of the mass are shown for the same simulation. It can be seen that only around time 6, when the first impact takes place with a high velocity, a layer higher than 0.1, corresponding to the third blue contour line, is overflowing the cuboid. In the experiment with a granular material consisting of Vestolen, with a mean diameter of 4 mm, which is in scale of the numerical model 0.12, it was observed that some single particles jumped over the obstruction. Single particles can not be simulated in a continuum mechanical model, so a small overflow seems to be reasonable.

In later time steps the mass in the front of the obstruction is very slow and the overflow in the model is negligible as shown in experiments.

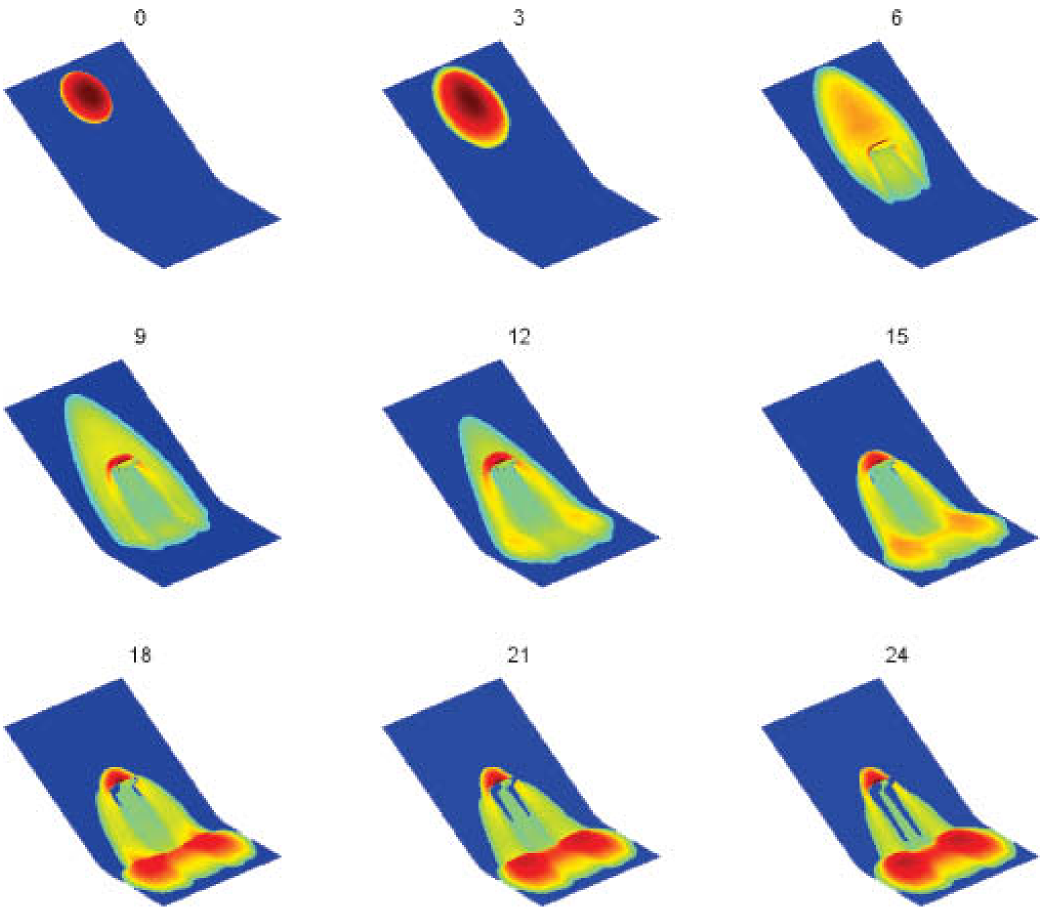

Figure 5.2: Interaction between granular flow and cuboid obstruction. Numerical simulation with three levels of refinement on a disarranged grid. The colour scheme indicates the depth of the mass, blue means almost no mass, red high depth.

5.3.2 Tetrahedra

For simulations of tetrahedral wedges better results can be expected than for steep walls, since no accumulation in the front of the obstruction can be expected if one of the edges is pointing up the slope, facing the granular flow. Still, the numerical results show similar weaknesses as for cuboid obstructions. The impact of the obstruction, when compared to laboratory experiment is underestimated in the numerical model. The results of the extended model for tetrahedra, using AMR, which will be shown in the following, do not refer to an laboratory experiment as for the cuboid, since the documentation in literature was not sufficient. Instead the focus will be on the purely numerical computations of the critical height.

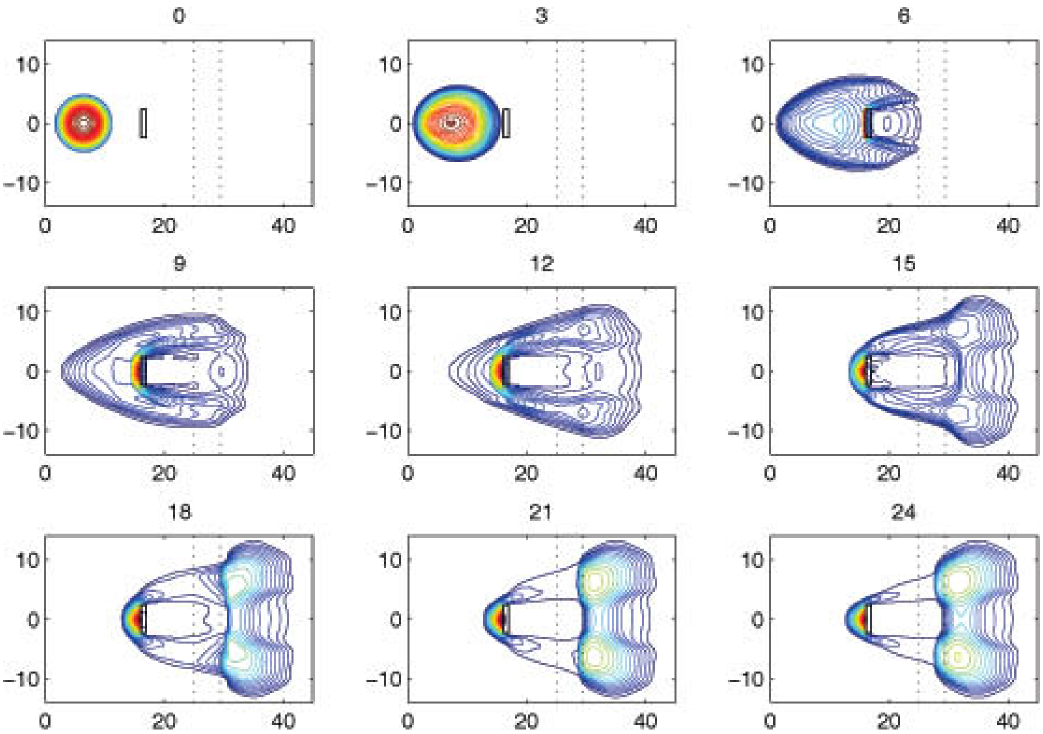

Figure 5.3: Ground view of the interaction between granular flow and cuboid obstruction. Numerical simulation with three levels of refinement on a disarranged grid. The contour lines indicate the depth of the mass, the first blue line contours a depth of 0.02.

These are based on an arbitrarily chosen model chute, which is 30 dimensionless units long and 20 dimensionless units wide. The longitudinal units are divided in a 20 units long slope, followed by a 4 units long transition zone and a 6 units long horizontal run-out zone. The inclination angle of the chute is 40°. Similar to the cuboid, the tetrahedra is defined by the derivatives of the elevation function (4.4) and (4.5) and is placed in the center of the slope, in respect to the cross-slope direction y. The distance between the lower edge of the tetrahedra and the upper edge of the slope is 17. The edges of the basal equilateral triangle have length $L = 4$. The height of the tetrahedra is varied to find the minimum to avoid overflow, so-called critical height. The granular mass with the internal friction angle $\phi = 35°$ and the basal friction angle $\delta = 30°$ is stored in a 4 units long, 2 units wide and 1 unit high semi-elliptical shape. The whole chute is covered by a rectangular grid with 301×101 grid points.

In order to compute the critical height an obstruction is defined to be overflown if the mass on the peak of the obstruction is higher than 0.02

dimensionless units at time step 9. The accuracy of calculations is one decimal, which is sufficient for qualitative observations. This definition follows the definition of Chiou [8]. It seems to be relatively arbitrary, but in order to be able to compare the results, the same criterion is used within this work. Since the laboratory experiments showed that the impact of the obstruction is underestimated, hence the critical height in the computations is too high, a result will be considered the better the lower the critical height is, although the real critical height is unknown, since the calculations are not based on experiments.

Table 5.5: Comparison of global refinement for a granular granular flow hitting a tetrahedral obstruction. Measured values are: critical height of the tetrahedra to avoid overflow at a dimensionless time 9 and calculation time for dimensionless time $t = 24$.

grid size	critical height	calculation time
301×101	4.4	5 min
301×201	2.6	9 min
301×401	1.8	26 min
601×101	5.0	22 min
601×201	3.1	33 min

The first observation compares, as for the cuboid obstruction, different global refinements. Chiou used 301×101 grids, which correspond to a grid size $dx = 0.1$ and $dy = 0.2$. This seems to be a reasonable choice for cuboid obstructions, where the main interaction takes place in x-direction, but for tetrahedral wedges the lateral deflection is mainly caused by the cross-slope gradient at the side walls. This effect can be seen in Table 5.5, which shows the critical height for globally refined grids without any AMR. The sensitivity of the critical height to the cross-slope refinement is much higher than to pure downslope refinement. The results get even worse if only the x-coordinate is refined. An explanation for this behaviour has not be found yet.

As for the cuboid obstruction, AMR can be used to improve the result. The area to be refined is rectangular, covering the whole tetrahedral obstruction. It is chosen relatively arbitrarily with a minimal distance of 1 unit to the basal triangle. When compared to other calculations with other areas this choice is proved to be good. Choosing larger refined areas was demonstrated no further improvement on the calculated critical heights, while the calculation time increased. As for the cuboid, the finest grid of each calculation covers the same area. Each parent covers the area of its child and is extended by 5 grid points in each direction.

Table 5.6: Comparison of local refinement levels for a granular flow hitting a tetrahedral obstruction, based on a grid with 301 $\times$ 101 points. The given level describes the finest level of refinement used. The grid with finest level of refinement covers a fixed rectangular area, which extends the basal triangle in the slope by at least 1 unit in all directions. Measured values are: critical height at a dimensionless time 9 and calculation time for dimensionless time $t = 24$.

level	critical height	calculation time
1	3.1	8 min
2	2.1	22 min
3	1.6	2 h 30 min
4	1.4	7 h 17 min

Table 5.7: Comparison of local refinement levels for a granular flow hitting a tetrahedral obstruction, based on a grid with 301 $\times$ 201 points. The given level describes the finest level of refinement used. The grid with finest level of refinement covers a fixed rectangular area, which extends the basal triangle in the slope by at least 1 unit in all directions. Measured values are: critical height at a dimensionless time 9 and calculation time for dimensionless time $t = 24$.

level	critical height	calculation time
1	1.8	16 min
2	1.3	42 min
3	1.2	6 h 51 min
4	1.2	62 h 23 min

Table 5.6 shows the results for the basic 301 $\times$ 101 grid. There is a clear tendency for lower critical heights for increased numbers of refinement levels. When starting with a 301$\times$201 grid the results get even better, see Table 5.7. A further increase in the refinement level will not cause obvious improvement, while computation time increases. The importance of the choice of the basic grid can be seen, when comparing the two tables.

Figure 5.4 shows a two-dimensional ground view for the above described set-up. The basic grid was 301 $\times$ 201 with four levels of refinement. The height of the obstruction is set to 1.2, the critical height for this grid. The result shows the expected behaviour. The mass is split by the obstruction and builds two accumulations in the run-out zone. As expected, there is no accumulation in the front of the obstruction. Shock waves can be seen in the run-out zone, where contour lines lie tight at the side pointing to the slope.

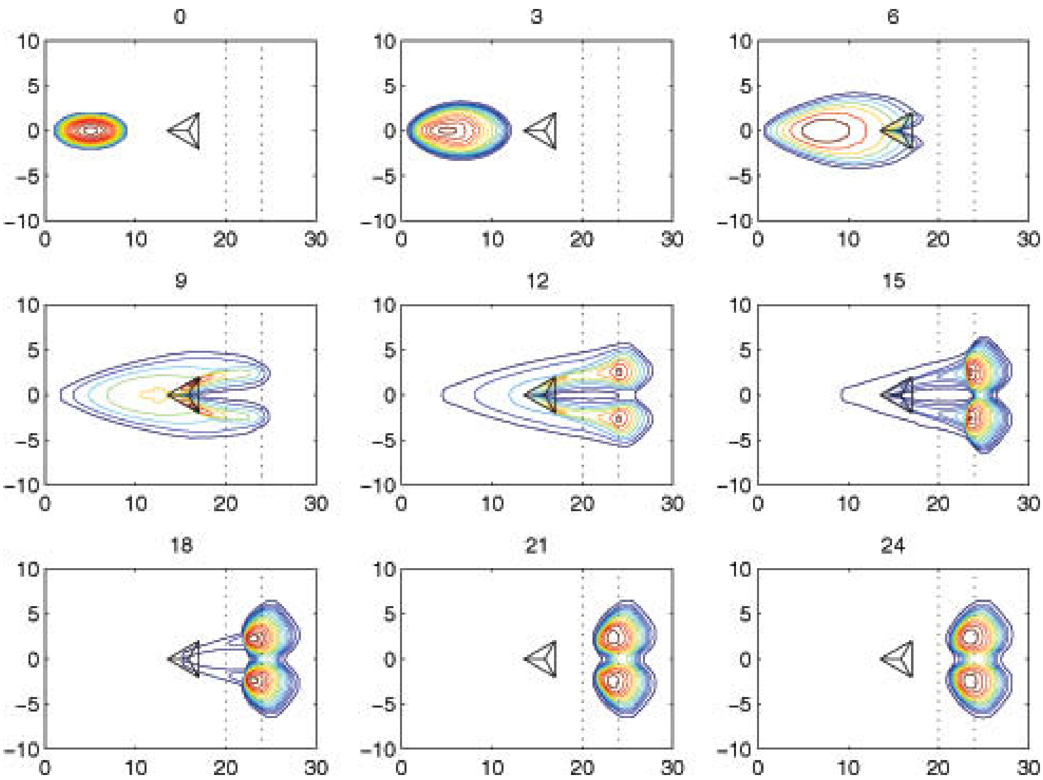

Figure 5.4: Ground view of the interaction between granular flow and tetrahedral obstruction. Numerical simulation with four levels of refinement. The contour lines indicate the depth of the mass, the first blue line contours a depth of 0.02.

5.4 Conclusions

It can be clearly seen that the continuum mechanical simulations become better with increased grid resolution. The Adaptive Mesh Refinement (AMR) method has proven to be suitable to be applied for local grid refinement. This way much finer grids can be used locally than with global refinement at comparable level of computation time and demand on memory.
Still, systematical weaknesses of a depth-averaged model in cases of steep walls, cannot be neglected.
In case of tetrahedral wedges the results look promising, but no useful experimental data was found in literature to validate the results.

Chapter 6

Additional Planes

In the last chapters the obstructions were implemented by overlaying an elevation function. By using this function, only height differences in the basal surface enter the model equations. The basal surface, where the grid for the numerical calculations is attached to, is unaffected. Errors can be expected, which raise proportional to the height differences in the elevation function. The most extreme case is a steep wall, attached perpendicular to the slope plane, as it is often used in laboratory experiments, see e.g. Chiou [8]. To avoid this unphysical modelling, obstruction can be implemented directly into the basal surface, without using an elevation function or, if so, only for minor alterations.
The Finite Differences Method used for the numerical calculation, see Chapter 3, is strictly limited to uniform, rectangular grids. Hence, obstructions cannot be simply added to the grid. Even more flexible methods, like the popular Finite Element Methods, are restricted in the choice of the surface. Singularities, as they can appear at the edges, e.g. where the slope plane intersects the perpendicular side planes of the obstruction, are problematic.
To implement an obstruction to the above presented model, additional planes are created for the model. Each of these new planes represents one surface plane of the obstruction and interacts with the other planes, including the slope plane, at its interaction lines. The Singularities appearing at these interaction lines need to be treated. A physical treatment would be very difficult, even impossible for a simple depth-integrated model, as the presented one. Within this work, the complex behaviour at the singularities are covered by a parameter, corresponding to the force compensated at these points. A discussion of this parameter will be conducted in Section 6.2.
After each time step, the interaction of the different planes has to be carried out. Therefore, an overlapping area is needed, where the planes interact. This overlapping area is attached to all planes at all sides. In this area, re-

sults of one plane are transfered to the neighbor plane and vice versa. This transfer of data is comparable to the transfer between parent and child grid in the AMR method, see Chapter 5.

6.1 Modelling Cuboid Dams by Using Additional Planes

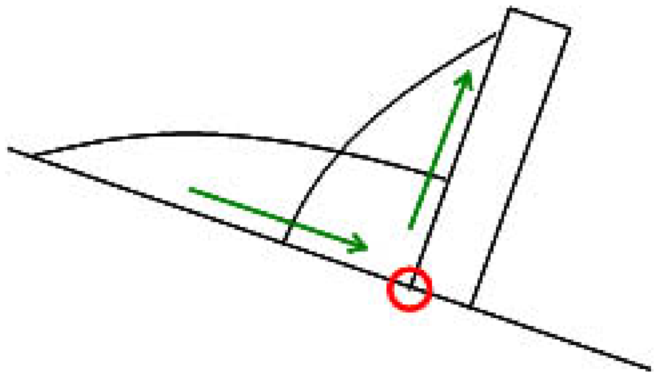

Figure 6.1: Sketch of cuboid, built by additional planes. The downward moving mass is transfered from the basic plane of the slope into the front plane of the cuboid. At the intersection of the two planes (marked by circle) a singularity occurs.

In case of cuboid dams five new planes are created, representing the front, back, left, right and top plane of the cuboid. The created planes have to be a bit larger than the corresponding planes of the cuboid. At each side points have to be added. These grid points lie in other planes and will be called overlapping area below. This area is needed for the numerical computations, see Chapter 3. After each time step the values for the overlapping area are copied from the adjacent plane. Also the basic plane needs such an overlapping area where interaction with other planes occurs.
The main flow direction is downwards and the cuboid dam is placed orthogonal to the thalweg. Overflow of the dam has to be avoided, since Savage-Hutter theory can not describe such action. Therefore the main interaction takes place between basic plane and front plane. Figure 6.1 shows a side view of the main movement of the mass. At the intersection of the basic plane of the slope and the front plane of the cuboid (marked with a circle) the mass is transfered from one plane to the other. In this point a singularity occurs that needs further treatment.

When the granular flow hits the front plane, a lot of kinetic energy is compensated by the dam. Mass is stored in front of the dam. The path of the remaining mass is also changed significantly, as it flows along the upper surface of the stored mass. Such behaviour can not be simulated in detail by the used model. The model described in Chapter 2 is depth integrated. So it is impossible to let part of the mass rest without extending it to a far more complicated three-dimensional model, or a model able to handle deposition of mass. Further, Savage-Hutter theory describes only moving mass and can not be applied for stored mass.

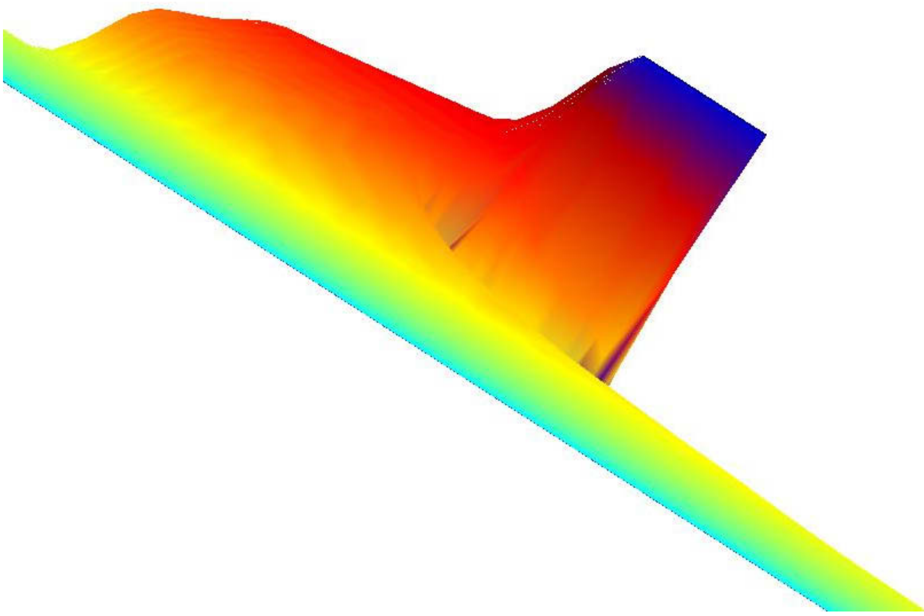

Figure 6.2: Side view of the simulation, zoomed at the accumulated mass in the front of the dam. The colour scheme indicates the depth of the mass, blue means almost no mass, red high depth.

To describe a comparable behaviour, the loss of kinetic energy has to be simulated. This will not allow mass to be stored in the front, but the mass will slow down and create an accumulation quite similar to stored mass. A snap shot of this almost static behaviour is shown in Figure 6.2. The figure

shows a side view zoomed on the cuboid obstruction. The colour scheme indicates the depth of the mass, measured from the slope plane. Blue surface means almost no material, as can be seen at the top of the cuboid, which is not overflown. Red colour indicates high depth, like at the front side of the dam. The mass in the front is not really deposited, but is flowing very slowly and replaced by the successive mass. This way the surface in the front keeps an almost stable shape. Only the tail of the granular flow is changing significantly as no mass is replacing it.
To consider the loss of kinetic energy a parameter η is introduced. $(1-\eta)$ represents the rate of the loss of kinetic energy due to the change of the flow from the slope surface to the front of the obstruction. A geometrical or physical estimation of η is difficult, due to the complex behaviour described above. Hence, a paramter study is conducted to identify η.

6.2 Parameter Study

Figure 6.3 shows a parameter study for η for values in $[0;1]$ at a fixed time step. At the chosen time step, the granular flow has already hit the obstacle and the material has already reached it's maximal depth at the front. Though only a small amount has passed the obstruction and the stable shape is not fully developed yet.
The interesting area for the parameter study is the area in front of the dam. To evaluate the parameter the height reached by the material is observed. In the model, this is equal to the distance the mass can climb up the steep front plane of the cuboid. Therefore, Figure 6.3 shows zoomed side views of the obstruction for a model based on experiments done and documented by Chiou (see Chapter 4). The released material were Vestolen with an internal friction angle $\phi = 37°$ and basal friction angle $\delta = 24°$. The slope angle ζ of the 933.5 mm long chute was chosen 40°, followed by a constantly curved transition zone and a flat runout zone. A 80 mm high and 160 mm wide wall was positioned at $P1$, with a distance of 650 mm to the upper edge of the chute. In the computer program the cute is represented by a dimensionless 43×24 sized model. The slope angle for the model is

$$\zeta(x) = \begin{cases} \zeta_0, & \text{for} \quad x \leq 25, \\ (29.4 - x)/(29.4 - 25)\zeta_0, & \text{for} \quad 25 < x < 29.4, \\ 0°, & \text{for} \quad x \geq 29.4, \end{cases}$$

where $\zeta_0 = 40°$. The wall is represented by a cuboid. The center is placed at $x = 16.5$ and central in respect of the y-coordinate. The front plane is placed orthogonal to the thalweg of the slope and is 2.4 units high and 4.8

units long. The width of the cuboid can be chosen relatively arbitrarily. If the mass is not overflowing the mass, the area behind the front wall is free of mass, called granular vacuum. Therefore, the choice of the width of the wall will not effect the simulation significantly. It is set to 1 for this computation. For the calculation a rectangular grid consisting of 431×241 points is laid over the model domain, yielding $\Delta x = \Delta y = 0.1$ for the grid size. The effect of the grid size is discussed more detailed in Chapter 5. The planes that create the cuboid must also be covered by a grid. The grid size can be arbitrary, it can be chosen independently of the basic grid size. But the simplest choice is to set it equal to the basic grid size, since the solutions on the grid points can be transfered without interpolation. Thus, front and back planes are covered by 25×49 points, left and right side plane by 11×25 points and the top plane by 11×49 points. All these specifications do not include the overlapping area, for which 3 to 5 additional points must be added on each side.
The starting mass was released from the Shallow-Cap (see Section 4.1). In the computer model this is simulated by a semi-ellipsoid with axis $a = b = 4.74$, both axis lying in the slope plane, and $c = 1.8$, orthogonal to the slope. This is not perfectly simulating the shape of the Shallow-Cap of the experiments, but the difference is negligibly small (see e.g. [8]). The shallow cap is placed at the top of the chute, in the center in respect of the y-coordinate.

The corresponding laboratory experiment showed that the mass reached the top of the obstruction. A few single particles even overflew it.
Unfortunately no pictures were taken from the side in Chiou's experiments. Nevertheless, side views of the model are used to make some qualitative statements about parameter η. As Figure 6.3 shows, the parameter η affects the flow as expected. For low values of η the mass does not move up the front plane of the obstruction very far. The higher the value, the higher the mass is climbing up the front plane, till it reaches the top of the cuboid. At 0.9 it can be seen that a significant amount of mass is overflowing.
The best choice seems to be a value between 0.7 and 0.9, as the mass is almost reaching, but not overflowing the wall at 0.7 and already overflowing at 0.9. To make more detailed statements, better experimental datasets, with detailed information about the depth of the mass in the front, are necessary.

6.3 Results

Figure 6.4 shows the numerical results of the computations in a general view. It is done for the same set-up as the parameter study, described above. But this time, the parameter is fixed at $\eta = 0.8$, which is in the middle of the

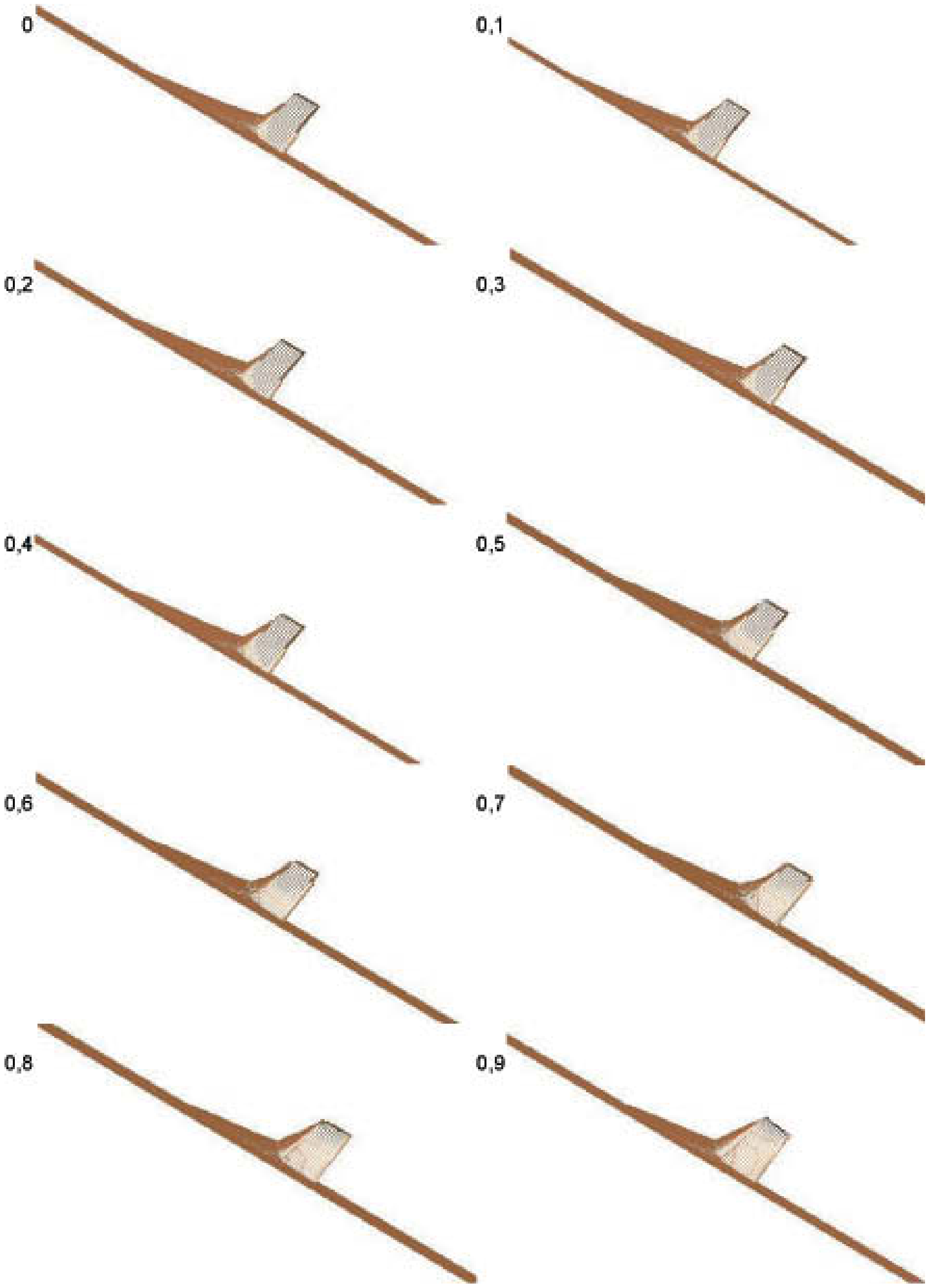

Figure 6.3: Study of parameter η. Side view of the simulations for $\eta = 0, 0.1, 0.2, 0.3, 0.4, 0.5, 0.6, 0.7, 0.8, 0.9$, zoomed at the accumulated mass in the front of the dam.

interval, that was observed to contain the reasonable values, and the development of the granular flow over time is observed. The granular flow is recorded

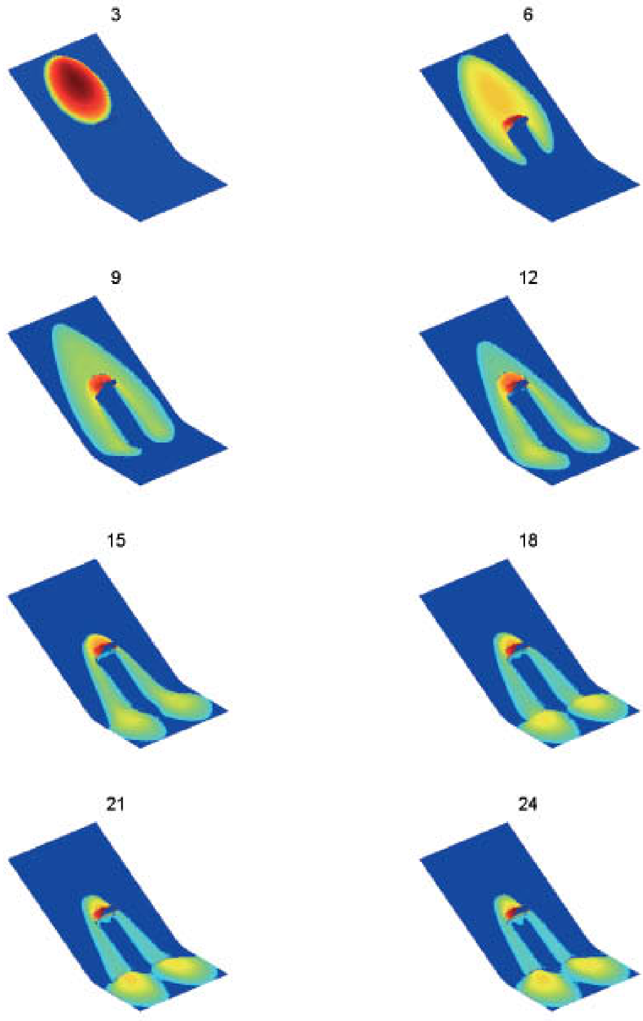

Figure 6.4: Numerical result for chute with cuboid obstruction, where the obstruction is built with different additional planes and the parameter $\eta = 0.8$. The colour scheme indicates the depth of the mass, blue means almost no mass, red high depth.

at different dimensionless times $t = 3, 6, 9, 12, 15, 18, 21$ and 24. These calculations were stopped at $t = 24$, since after that time the dynamic movement ends. At the corresponding time step of the experiment, the whole mass

already stopped. In the computations the mass cannot come to rest. This is due to the nature of the Savage-Hutter equations, which are only capable to describe the dynamics but not the still state. To describe this behaviour, some deposition model has to be used.
The colour scheme indicates the depth of the material. Again, blue areas contain almost no mass, while red indicates high depth, measured from the slope surface. At time $t = 3$ the free moving granular flow is still building up its shape. At time $t = 6$ the obstruction is hit and it can be seen that the mass is divided into 2 parts, passing the obstruction symmetrically on the right and left side. In the front of the obstruction, the mass is decelerated and is forming the accumulation described above. The maximum of deposition in the front can be observed at time $t = 9$. From time $t = 12$ on, no mass from the top of the chute is following. Therefore, the accumulation in the front is decreasing, but keeps a basic shape, close to that observed in experiments. In the same time, the deposition in the run out zone is raising, consisting of two symmetric heaps, one formed by the mass that passed the obstruction on the left side, one by the mass that passed on the right side.
It can be seen clearly that no mass is overflowing the obstruction. In the back of the obstruction, a granular vacuum can be observed. Only in the later time steps, when the deposition is spreading to the sides, the central area, but only in the run out zone, is filled again. When compared to the corresponding experimental observation (see Figure 4.6) the final deposition looks different. The numerical simulation no central deposit is formed in the run out area, unlike the corresponding experiment where a small central accumulation can be observed. This is due to the small overflow observed in the experiment. It should be mentioned once more, that overflowing can not be modeled within this model, as presented here. Overflowing would force the material to slide upside down along the back plane. Without introducing a free fall criterion, no realistic result can be expected. Obviously, only for experiments without overflowing satisfactory results can be expected. But then identification of the parameter η becomes difficult, since no observation concerning the depth reached by the mass in the front were documented.

6.4 Conclusions

The presented method is an alternative approach to simulate the interaction of granular flows with cuboid obstructions, which cannot be properly handled by the elevation function added to the continuum mechanical model, as in the previous chapters. The singularity at the intersection of the different planes, which exists in the real world, also occurs in this model, in contrast to the elevation function model. This alternative approach uses a parameter $\eta \in [0;1]$ to simulate the loss of kinetic energy by the granular flow when hitting the obstruction and compensating the complex physical procedures at the intersection lines. Although it has similar unphysical features as the previous model when mass is stored in the front of the obstruction, the model is able to simulate a realistic behaviour at the front side of the obstruction. But it fails if overflow should be simulated.

Chapter 7

Impact Force Computation

Measuring active forces in gravity driven granular flows in field or laboratory experiments is difficult. Only a limited number of sensors can be placed and they distort the flow by interacting with the moving material.
Numerical simulations are an interesting alternative to compute forces. Applicable models are based on the principles of continuum mechanics for shallow flows. They are depth integrated, assuming negligible small differences in the velocity distribution through the depth.
When observing the interaction of rapid flows and obstructions, the forces acting on the obstructions are of special interest, for computations of the static of the building as well as for estimation of the absorbed energy.
In this chapter, the forces acting on the obstruction for employing the continuum mechanical model, presented in Chapter 2, where the obstruction is added by using the elevation function, are computed and compared to experimental observations.
An interesting alternative is the use of Distinct Element Methods (DEM), which enables a fully three-dimensional computation.

7.1 Continuum Mechanical Model

The obstruction enters the model, (2.87) - (2.92), only via the terms

$$\varepsilon \cos\zeta \frac{\partial z_b}{\partial x} h, \tag{7.1}$$

$$\varepsilon \cos\zeta \frac{\partial z_b}{\partial y} h, \tag{7.2}$$

as external forces. (7.1) and (7.2) are gravitational forces, caused by the height differences in the topography, which are described by the elevation

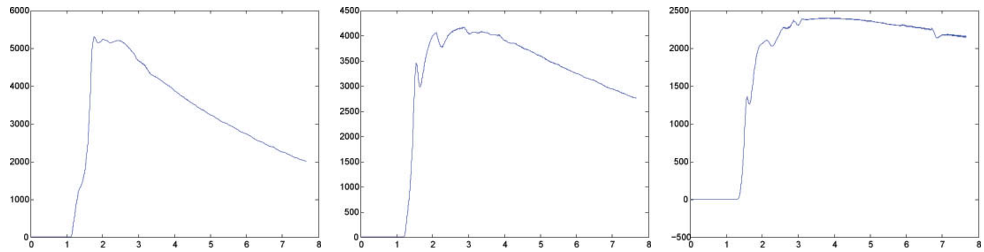

(a) $\zeta = 40°$ (b) $\zeta = 35°$ (c) $\zeta = 30°$

Figure 7.1: Comparison of forces acting on cuboid obstructions for different slope angels $\zeta = 30°, 35°$ and $40°$. Internal friction angle $\phi = 40°$ and basal friction angle $\delta = 28°$.

Table 7.1: Comparison of maximal and mean forces acting on cuboid obstructions for different slope angels $\zeta = 30°, 35°$ and $40°$. Internal friction angle $\phi = 40°$ and basal friction angle $\delta = 28°$.

ζ	maximal force	mean force
30°	2403	1583
35°	4170	2635
40°	5298	2609

function z_b.
Summing up these terms for all grid points, can be considered the force acting on the obstruction in x- and y-direction, respectively.

7.1.1 Cuboid

To observe the force acting on a cuboid obstruction, calculated by the continuum mechanical model (2.87) - (2.92), a set-up comparable to the experiments, described in Section 4.1, is chosen. The chute is in total 15 units long and 16 units wide, where the slope plane is 9.3 units long, the horizontal run-out plane is 4.35 units long and a constantly curved transition zone inbetween.
Before release, the material used for these computations is stored in a semi ellipsoid with a circular base of radius 0.85 and height 0.475. The internal friction angle is $\phi = 40°$ and the density $\rho = 1379$ kg/m^3. The cuboid obstruction is 1.5 units high, 2.4 units long and 0.9 units wide. It is placed perpendicular to the thalweg in the centerline of the chute, in respect to the y-coordinate, 7.3 units below the upper edge of the chute.
The inclination angle was varied between $\zeta = 30°, 35°$ and $40°$. The effects

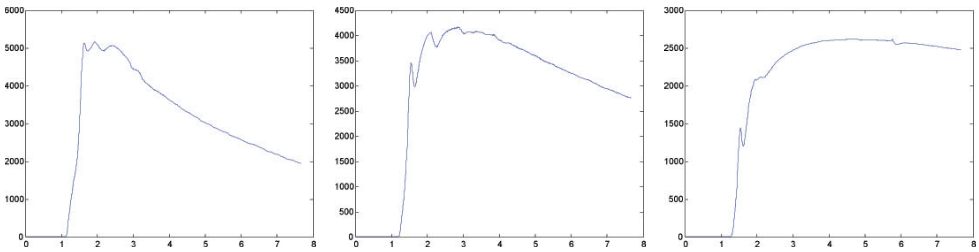

(a) $\delta = 23°$ (b) $\delta = 28°$ (c) $\delta = 33°$

Figure 7.2: Comparison of forces acting on cuboid obstructions for different angels of basal friction $\delta = 23°, 28°$ and $33°$. Slope angle $\zeta = 35°$ and internal friction angle $\phi = 40°$.

Table 7.2: Comparison of maximal and mean forces acting on cuboid obstructions for different angels of basal friction $\delta = 23°, 28°$ and $33°$. Slope angle $\zeta = 35°$ and internal friction angle $\phi = 40°$.

δ	maximal force	mean force
23°	5164	2478
28°	4170	2635
33°	2622	1747

of the varied slope angle can be seen in Figure 7.1. The exact values for the maximal calculated force and the mean force for the whole computational time $t \in [0, 7.6584]$, are listed in Table 7.1. After a strong impact, the force is decreasing as the mass is passing th obstruction. It can be seen that the force is very sensitive to the slope angle, since the velocity rises with increased slope angle. For $\zeta = 40°$ (Figure 7.1a), the impact force is higher and is decreasing faster afterwards, due to the higher velocity. For $\zeta = 30°$ (Figure 7.1c), hardly any impact force can be observed. Due to the low slope angle, $\zeta = 30°$, which is only slightly higher than the basal friction angle $\delta = 28°$ of the used material, the velocity is very low and the calculated forces are mainly caused by the weight of the material, not by the velocity. The behaviour for $\zeta = 35°$ (Figure 7.1b) is between those for $\zeta = 30°$ and $\zeta = 40°$.

Alteration of the the basal friction angle $\delta = 23°, 28°$ and $33°$, with fixed slope angle $\zeta = 35°$ and all other values as described above, has similar effects as the alteration of ζ, as can be seen in Figure 7.2. The computed values for maximal and mean force are listed in Table 7.2. For $\delta = 33°$ (Figure 7.2c), the slope angle, $\zeta = 35°$, is only slightly larger than the basal fiction angle, implying a slow movement in which hardly any impact force can be observed,

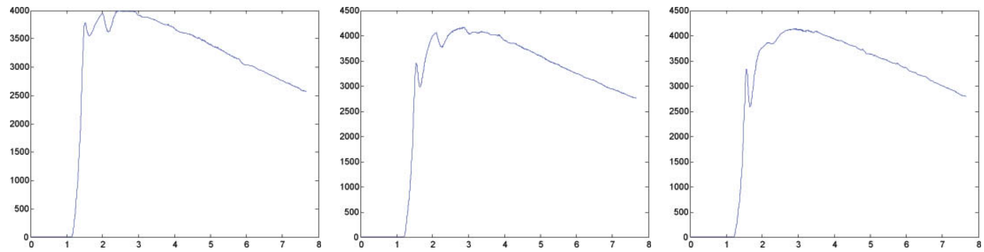

(a) $\phi = 45°$ (b) $\phi = 40°$ (c) $\phi = 35°$

Figure 7.3: Comparison of forces acting on cuboid obstructions for different angels of internal friction $\phi = 35°, 40°$ and $45°$. Slope angle $\zeta = 35°$ and basal friction angle $\delta = 40°$.

Table 7.3: Comparison of maximal and mean forces acting on cuboid obstructions for different angels of internal friction $\phi = 35°, 40°$ and $45°$. Slope angle $\zeta = 35°$ and basal friction angle $\delta = 40°$.

ϕ	maximal force	mean force
35°	4143	2626
40°	4170	2635
45°	3955	2543

similar to Figure 7.1c. For decreased angel of basal friction $\delta = 23°$ (Figure 7.2a), the velocity is higher resulting in a higher impact force and fast passing after the impact. Again, the results are similar to those of increased slope angle $\zeta = 40°$, shown in Figure 7.1a.

The effects of altering the angle of internal friction, $\phi = 35°, 40°$ and $45°$, are far less obvious. The computed maximal and mean forces, see Table 7.3, show no clear influence of the internal friction angle on the impact measured maximal or mean impact force. The values for $\phi = 35°$ lie between those for $\phi = 40°$ and $\phi = 45°$. More information on the effect can be taken from the graphical displays of the forces in Figure 7.3. For $\phi = 45°$ (Figure 7.3a), the force of the first impact is slightly larger, but its maximum is soon reached. With decreased angle of internal friction, the first impact becomes weaker, but the force builds up more slowly and reaches a higher absolute maximum.

Moving the obstruction one unit up or down the slope, $P = 6.3, 7.3$ and 8.3, effects the results mainly in a highly expected way. The time of the first impact is about 0.2 time units earlier, respectively later (see Figure 7.4). Looking at the computed maximal and mean forces for the different positions, listed in Table 7.4, it can be seen that the maximal force becomes

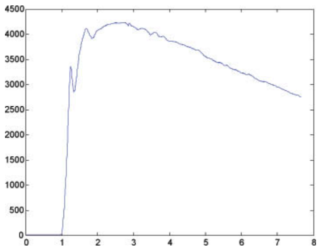

(a) $P = 6.3$

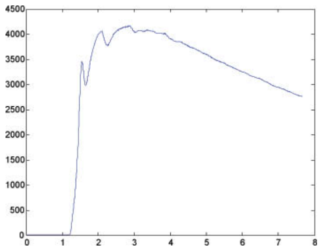

(b) $P = 7.3$

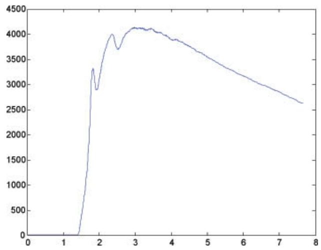

(c) $P = 8.3$

Figure 7.4: Comparison of forces acting on cuboid obstructions for different positions, $P = 6.3, 7.3$ and 8.3, of the obstruction. Slope angle $\zeta = 35°$, internal friction angle $\phi = 40°$ and basal friction angle $\delta = 40°$.

Table 7.4: Comparison of maximal and mean forces acting on cuboid obstructions for different positions, $P = 6.3, 7.3$ and 8.3, of the obstruction. Slope angle $\zeta = 35°$, internal friction angle $\phi = 40°$ and basal friction angle $\delta = 40°$.

P	maximal force	mean force
6.3	4234	2739
7.3	4170	2635
8.3	4133	2488

lower for obstructions places further down the slope, although it can be expected that the impact velocity is higher in this case. The clear reduction of the mean force, can be explained by the later impact.

Unfortunately, there were no experiments that could be used to validate these computed solutions. Chiou [8] documented some pressure measurements, but the used circular sensor, which was places in the front plane of the obstruction, could only measure the pressure acting on the sensor, not on the whole obstruction. The results (see Figure 7.5) are therefore not comparable to those of depth averaged continuum mechanical models. Also other force measurements of rapid flows, found in literature, were not comparable. The basic behaviour is captured well. But considering the weaknesses described in Chapter 4 and the missing experimental evaluation, it cannot be expected that the results are completely reliable. Solutions of better quality can be expected for dams with flatter slopes or tetrahedral wedges, see Section 7.1.2.

7.1.2 Tetrahedra

The simulation for tetrahedral wedges with a continuum mechanical model should yield better results than those for cuboid obstructions with steep front slopes.
The force acting on the tetrahedra over time is shown in Figure 7.6. The result looks realistically, although no experimental results could be found in literature to validate the results. The impact force is rising rapidly when the flowing mass hits the obstruction and decreasing as the mass is passing.

7.1.3 Flume

As alternative to the chute experiment, a second laboratory experiment is used for validation. Sets of flume experiments were performed and documented by Moriguchi et al. [43].
The flume is 1.8 m long, 0.3 m wide and diaphanous acryl boards are used as side walls. The slope angle of the flume is adjusted at 45, 50, 55, 60 or 65 degrees. On top of of the flume a box with 50 kg of dry Toyoura fine sand, with a density of 1.379 kg/m^3, is fixated. Opening the front gate of the box releases the material.
At the bottom of the flume is a stress gauge, measuring the impact force and stopping the flow. This gauge covers the whole width of the flume, but it is only 0.3 m high, too low to stop the whole mass. A small amount of sand overflows the gauge and is stopped by the back wall of the flume. This

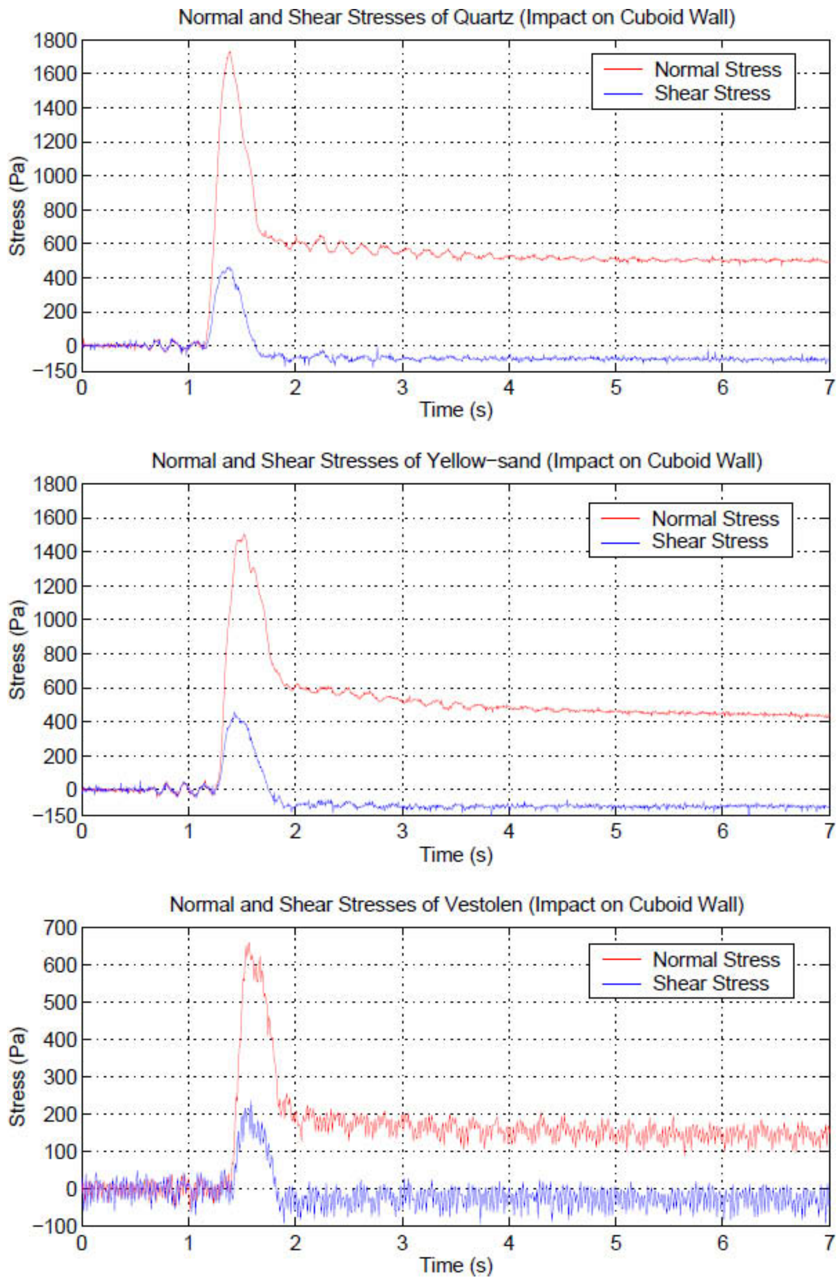

Figure 7.5: Normal and shear stresses of quartz (upper panel), yellow-sand (middle panel) and Vestolen (lower panel) when the bi-directional stress gauge is placed on the cuboid wall, by Chiou [8].

overflowing cannot be modeled properly with a continuum mechanical model. In the continuum mechanical model the back plane of the flume enters the model as border condition and the force acting on the back plane is calcu-

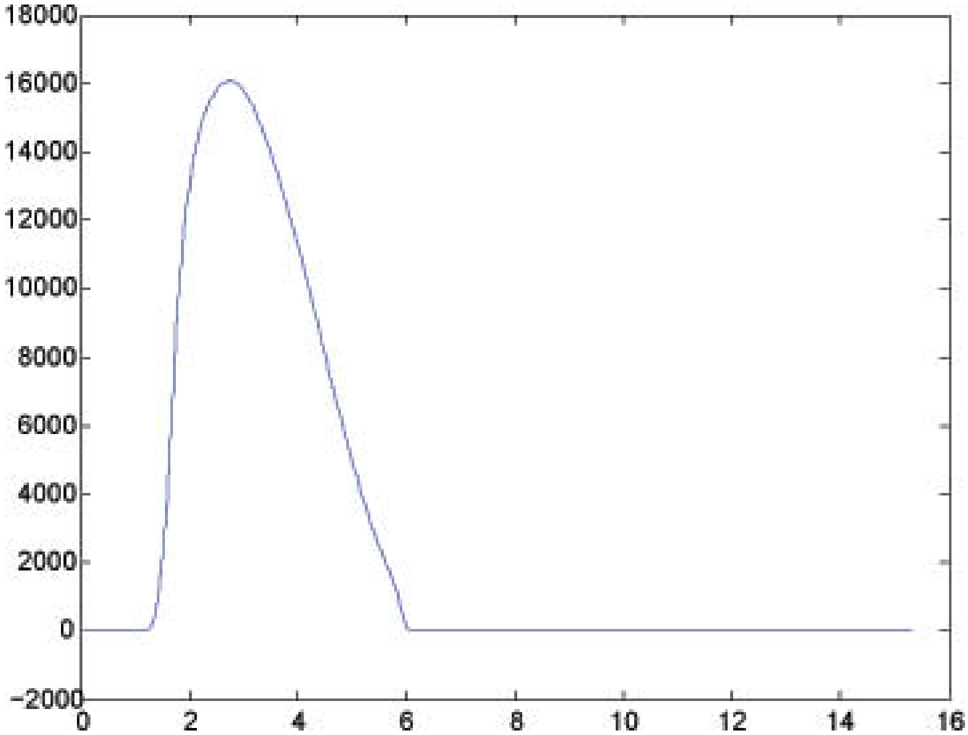

Figure 7.6: Graph of forces acting on tetrahedral obstructions.

lated.
The boundary conditions for the back plane, at $x = x_{end}$, are chosen to simulate a solid wall with no flow in x-direction, hence $u(x_{end}, y, t) = 0$. For the numerical scheme also the values $x = x_{end} + i$ for $i = 1, 2, 3$ need to be defined. They are

$$h(x_{end} + i, y, t) = h(x_{end} - i, y, t), \tag{7.3}$$
$$u(x_{end} + i, y, t) = -u(x_{end} - i, y, t), \tag{7.4}$$
$$v(x_{end} + i, y, t) = v(x_{end} - i, y, t). \tag{7.5}$$

For the side walls and the upper border of the chute, similar conditions are made.
Toyoura sand is also adhered to the ground surface of the flume, hence basal friction angle δ is roughly the same as the internal friction angle ϕ. The acryl side walls are smooth and are considered to be frictionless. To determine the internal friction angle ϕ, Moriguchi et al. [43] made a parameter study and compared the result to measurements of the experiment. Setting $\phi = 35°$ was demonstrated to be the best choice. Figure 7.7 shows a time history of side views of the simulation results with inclination angle $\zeta = 65°$. The blue

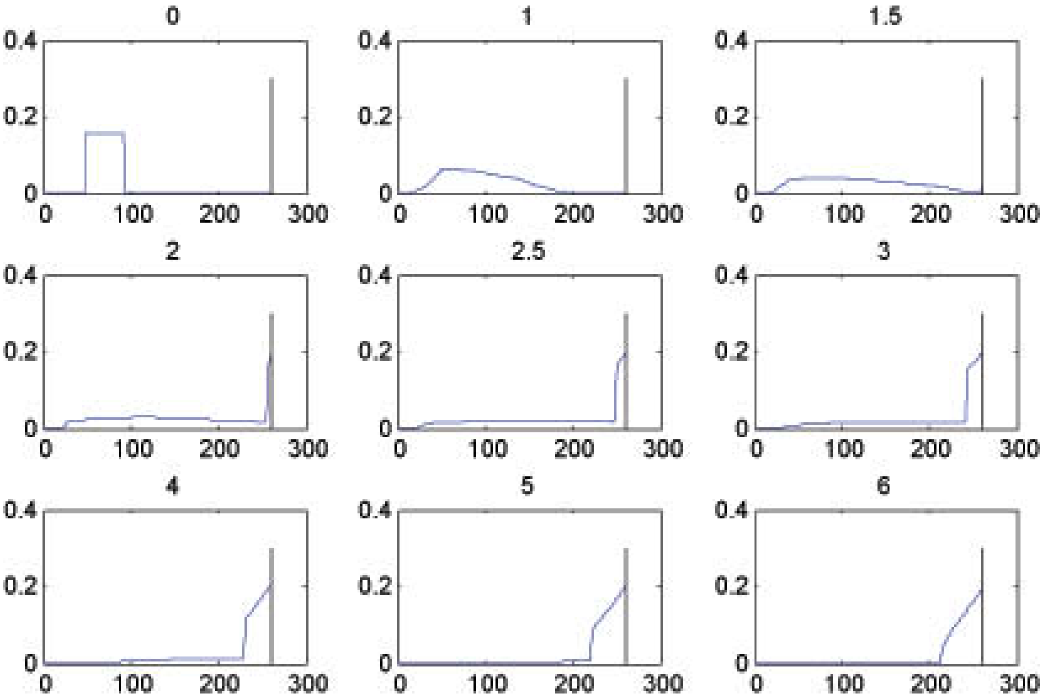

Figure 7.7: Granular flow in a flume with inclination angle $\zeta = 65°$ for non-dimensional times $t = 0, 1, 1.5, 2, 2.5, 3, 4, 5$ and 6. Blue line indicates the depth of the mass. The black line marks the back wall of the flume.

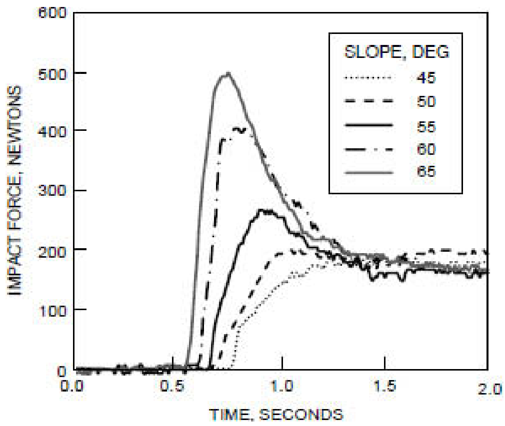

(a) Experiment

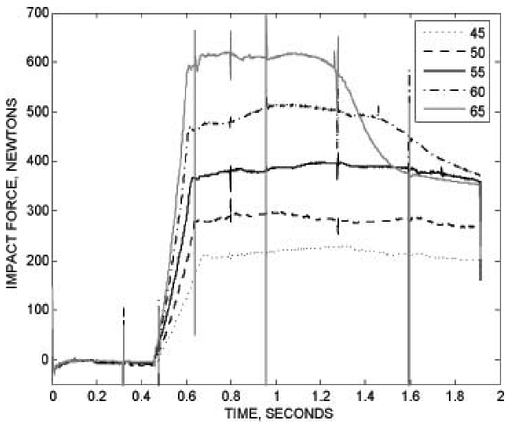

(b) Simulation

Figure 7.8: (a) Measured time histories of impact force for different flume inclinations, by Moriguchi et al. [43]. (b) Time histories of impact force for different flume inclinations computed by continuum mechanical model with friction angles $\delta = \phi = 35°$.

line indicates the depth of the mass.

The results for different flume inclinations are shown in Figure 7.8, with measurements by Moriguchi et al. [43] in Figure 7.8a and numerical results of the continuum mechanical model in Figure 7.8b. It can be seen that the simulation yields a far higher force than observed in the experiment. This can be explained by the low gauge in experiment, that is overflown. In the continuum mechanical model boundary conditions are used to simulate the back wall, hence no overflow is possible and the full impact is calculated.

For the simulations shown in Figure 7.7 and Figure 7.8, the friction angles δ and ϕ have been chosen according to the simulations of Moriguchi et al. [43]. A variation of the friction angles is shown in Figure 7.9. The slope angel is kept constant at $\zeta = 65°$. The three curves show the impact force over time for three different sets of friction angles, $\delta = \phi = 35°$, as in Figure 7.8, $\delta = \phi = 40°$ and a set where the basal friction angle $\delta = 35°$ is lower than the internal friction angle $\phi = 40°$. Especially for $\delta = 35°, \phi = 40°$ it can be seen that the first impact, caused by the kinetic energy of the granular mass, is far more distinguished than for the other parameter sets. A strong first impact is followed by rapid decrease of acting force, till a constant level, equal to the gravitational force of the mass, is reached. Very similar to what has been observed in the experiment. Again, the simulation is not comparable to the measurements, due to the overflow. Further experiments are needed to validate the model and identify the parameters.

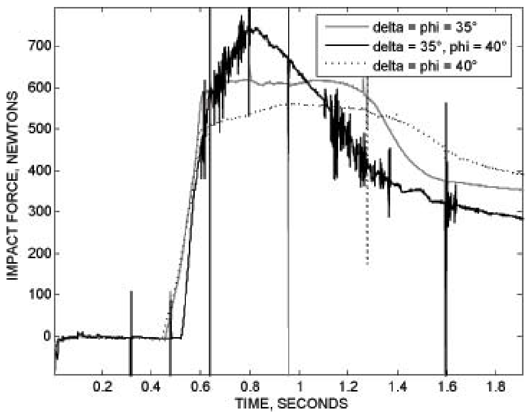

Figure 7.9: Measured time histories of impact force for different fiction angles: (a) $\delta = \phi = 35°$, (b) $\delta = 35°, \phi = 40°$ and (c) $\delta = \phi = 40°$.

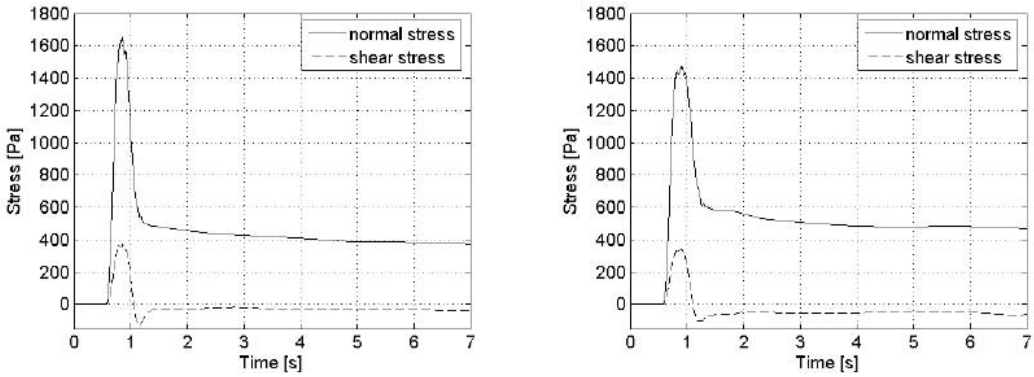

Figure 7.10: Evaluation of the impact forces against an obstacle for quartz (left panel) and yellow sand (right panel) from DEM simulations.

7.2 Discrete Element Method

DEM [11], as described in Section 4.3, using the comercial software PFC3d (Version 3.0, Itasca Consulting Group), can also be used to compute forces acting on an obstacle hit by a granular flow. The following simulations are based on and compared to the same laboratory experiments as used for the continuum mechanical model. In Section 7.2.1, the results for an granular flow passing a cuboid obstruction, comparable to the experiments by Chiou [8] are discussed. In Section 7.2.2 a channel flow, based on experiments by Moriguchi et al. [43], is discussed.

7.2.1 Cuboid

The set-up is describes in Section 4.1. A granular material, e.g. quartz or yellow sand, is released from a cap, flowing down an inclined Plexiglas chute until reaching, via a constantly curved transition zone, the horizontal run-out zone, where it comes to rest. In the lower part of the slope, a Plexiglas wall is positioned at the centerline of the chute, so that it is hit centrally by the granular flow. At the front side of this wall, a bi-directional stress gauge measures normal and shear stresses caused by the granular flow. The stress gauge is spherical and covers only a central part of the front side of the wall. PFC3d does not support spherical wall elements, so similar sized rectangular elements are used, on which acting stresses are computed on. The results of these computations are shown in Figure 7.10. When comparing these measurements to the experimental results of Chiou [8] (see Figure 7.5), the stresses are captured very well. Although, the same critical remarks on the identification of the sensitive material parameters as in Section 4.3 are true for these simulations. The experimental results can be successfully simulated, but forecasts based on DEM simulations are not reliable.

7.2.2 Flume

The flume experiment described in Section 7.1.3 is also implemented in a DEM model built in PFC3d. The parameter identification is as difficult as in the chute experiment. In addition to the viscous damping and particle rotation, also the basal surface conditions, i.e. the threshold velocity v_{sr}^{bw}, the retarding time λ^{bw} and the basal friction μ^{bw} for ball-wall interaction, have strong impact on the results, due to the rough surface of the sand coated flume.

Figure 7.11 shows a comparison for the impact force over time for different inclination angles $\zeta = 45°, 50°, 55°, 60°, 65°$. The left panel shows the measured values in the experiments by Moriguchi et al. [43], the right panel shows the results of the DEM simulations performed in PFC3d. As can be seen, the measured result can be predicted well by the DEM model.

7.3 Conclusions

All experiments for forces acting on obstructions interacting with granular flows, found in literature and used for validation within this work, are dealing with wall elements with steep front surfaces. Furthermore, they are not capturing the whole flow. The gauges are overflown, or don't cover the whole obstruction a priorily.

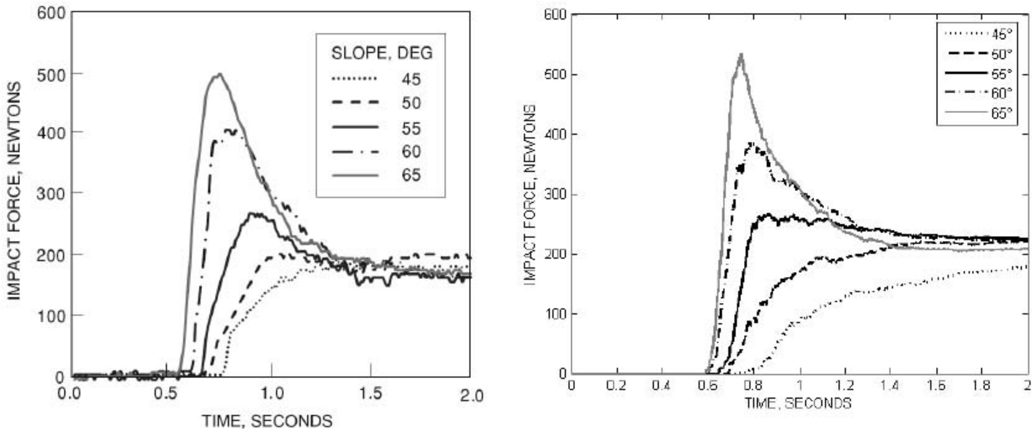

Figure 7.11: Left panel: Measured time histories of impact force for different flume inclinations, by Moriguchi et al. [43]. Right panel: Time histories of impact force for different flume inclinations computed by PFC3d.

Such experiments cannot be simulated properly in a depth averaged continuum mechanical model. For tetrahedral obstructions and simulations where obstructions can be built in as border conditions, the continuum mechanical model delivered realistic results, but other experiments are needed to validate these results.
The DEM model has proven to be applicable to simulate all presented experiments. The parameter identification is difficult and critical to achieve good results. Forecast simulations are hardly reliable due to the high sensitivity to the choice of the parameters. Also the demand on computational memory is large, making it difficult to handle large scale simulations.

Chapter 8

Concluding Remarks and Outlook

This chapter contains a summery of the main results. The topic of this thesis is on the interaction between granular flows and obstructions. The focus is on the continuum mechanical model based on Savage-Hutter theory. Moreover, an interesting alternative based on the Discrete Element Method using the commercial software PFC3d is discussed. The numerical simulations are compared with laboratory experiments.

8.1 Continuum Mechanical Model

The Savage-Hutter theory is suitable to simulate granular flows. The formulation is very elegant, yet physically substantial. The performance of the presented model is excellent if the topography is smooth.
If obstructions are implemented, like dams, the topography is no longer smooth. But the modelling of dams is of great interest for practice. Implementing obstructions with steep front walls by using the elevation function, originally added to model channel flows, leads to unrealistic results. The impact of the obstruction is underestimated. Some overflow over the obstruction is inevitable, although the material accumulation in front of the obstruction is far too low to expect overflow. This is partly due to the numerical scheme. It has been shown that the numerical scheme can be significantly improved by using local grid refinement, e.g. the Adaptive Mesh Refinement method (AMR).
Realistic simulation of the interaction with a steep wall cannot be provided though. In reality, the behaviour is too complex to be simulated by a depth-averaged model. The first mass hitting the obstruction is stopped and ac-

cumulates till it forms a wedge. The successive mass flows along the surface of the accumulated mass. To simulate such behaviour a three dimensional deposition model is needed. To simulate overflow of an obstruction, trajectories of single particles need to be modeled, the overflowing material cannot be modeled by a dense-flow model.
Simulations of granular flows interacting with tetrahedral wedges show much better results. Since the front sides of these obstructions are not steep and no mass is accumulated at its front, the assumptions of the theory still hold for material interacting with the obstruction. Still, the resolution of the grid influences the quality of the result significantly and the local grid refinement, by applying AMR, especially in cross-slope direction is useful. The documentation of experiments found in literature, regarding such objects, are rare though. Better experimental observations are needed to validate the model.

8.2 Numerical Scheme

Different numerical schemes have been tested to be applied to the extended Savage-Hutter model. The presented non-oscillatory central scheme (NOC) scheme with a Minmod Total Variation Diminishing (TVD) limiter has provided the best results. Being a Finite Difference scheme, it shares its drawbacks with other Eulerian schemes. The grid is inflexible, especially with regard to the local refinement and the computation time is larger than the Lagrangian schemes. The Adaptive Mesh Refinement (AMR) method enables local refinement, which also gives rise to reduced computation time.
As alternative the meshfree particle methods, which have been developed and applied to many different fields in the last years, could be applied to the model. But this has not been tested on avalanche models yet.

8.3 Discrete Element Method

The physical laws applied in the Discrete Element Method (DEM) are very simple. But the computational effort is large. In the last decades, with development of hardware, DEM became popular and is nowadays applied in many different fields.
In the presented examples, it can be seen that granular flows can be simulated very nicely. DEM allows a full three-dimensional simulation of the interaction between granular flow and obstruction. In cases where shallowness cannot be assumed and the movement can be observed in all spacial dimensions, DEM

is superior to the depth-averaged model.
DEM enables a good visualization of the flow dynamics and can be helpful for understanding the mechanisms. However, it seems less suitable for practice. The parameter identification is often very difficult. The numerical results can be hardly appreciated due to the high sensitivity to the choice of the parameters. Also the demand on computational effort is very high, making it difficult to handle large scale simulations.

8.4 Practice

In practice, dams are used mainly for three purposes, i.e. breaking, deflecting and capturing. Breaking dams shall break the avalanche, reduce its force and split it into smaller avalanches, deflecting dams are used to deflect the flow, while capturing dams are built to shorten the run-out zone, usually built directly in front of the infrastructure to be protected.
In the presented work only breaking dams are considered. The steep walls used in the laboratory experiments differ from the dams in practice. In practice, the front planes are not as steep, neither are the back nor the side planes. Alternatively, tetrahedral wedges, comparable to those presented in this work can be also found for breaking purposes.
Simulations of interaction with tetrahedral wedges seem to be possible with the existing model. For dams with plane front surface, the quality of results is dependent on various factors. The smoother the transition between slope and dam, the better the results. The steeper the front plane, the poorer the results.
For physically correct simulations of interaction with wall obstructions, like the ones presented here, the depth-averaged continuum is not suitable. This might be of interest for scientific investigations, but is it necessary to simulate such walls for practical purpose?
Even if the front plane of a dam is steep enough to store granular mass, the stored mass will act as a wedge for successive mass, similar to the effect of the tetrahedral shaped dams. Therefore, only the first part of mass hitting the dam needs some refined modelling. In large scale this should be negligible.

8.5 Outlook

Most well documented laboratory experiments, describing the interaction between granular flows and obstruction in literature deal with similar obstructions, namely wall elements. Of greater interest for testing depth-averaged

continuum models are tetrahedral wedges, or dams with small front slope angles. However, such experiments are scarce.
For evaluating the presented model against such obstructions, such experiments would be useful. Also measurements of impact forces on such obstructions are needed.

As to the numerical solution, the presented NOC scheme with AMR brings some improvement. The meshfree particle methods can be regarded as alternative. They allow more flexibility in grid coverage and could be more efficient in both solution quality and computation time.

Bibliography

[1] M. J. Berger and P. Colella. Local adaptive mesh refinement for shock hydrodynamics. *J. Comput. Phys.*, 82:64–84, 1989.

[2] M. J. Berger and J. Oliger. Adaptive mesh refinement for hyperbolic partial differential equations. *J. Comput. Phys.*, 53:484–512, 1984.

[3] E. Blayo and L. Debreu. Adaptive mesh refinement for finite-difference ocean models: First experiments. *J. Phys. Ozeanography*, 29:1239–1250, 1999.

[4] J. Bouchaud, M. E. Cates, J. R. Prakash, and S. F. Edwards. A model for the dynamics of sandpile surfaces. *J.Phys.I*, 4:1383–1410, 1994.

[5] T. Boutreux, E. Raphal, and P.-G. De Gennes. Surface flows of granular materials: A modified picture for thick avalanches. *Phys. Rev. E*, 58(4):4692–4700, 1998.

[6] R. Bowen and C.-C. Wang. *Introduction to vectors and tensors: volume 1 - linear and multilinear algebra.* Plenum Press, New York, 1976.

[7] R. Bowen and C.-C. Wang. *Introduction to vectors and tensors: volume 2 - vector and tensor analysis.* Plenum Press, New York, 1976.

[8] M.-C. Chiou. *Modelling dry granular avalanches past different obstructions.* PhD thesis, TU Darmstadt, 2006.

[9] M.-C. Chiou, Y. Wang, and K. Hutter. Influence of obstacles on rapid granular flows. *Acta Mech.*, 175:105–122, 2005.

[10] P. A. Cundall. Formulation of a three-dimensional distinct element model-Part I. a scheme to detect and represent contacts in a system composed of many polyhedral blocks. *International Journal of Rock Mechanics and Mining Sciences and Geomech.*, 25(3):107–116, 1988.

[11] P. A. Cundall and O. D. L. Strack. A distinct element model for granular assemblies. *Geotechnique*, 29:47–65, 1979.

[12] J. M. N. T. Gray, Y.-C. Tai, and S. Noelle. Shock waves, dead zones and particle-free regions in rapid granular free-surface flows. *Journal of Fluid Mechanics*, (491):161–181, 2003.

[13] J. M. N. T. Gray, M. Wieland, and K. Hutter. Gravity driven free surface flow of granular avalanches over complex basal topography. *Proc. R. Soc. London*, A 455:1841–1874, 1999.

[14] R. Greve and K. Hutter. The motion of granular avalanche in a convex and concave curved chute: Experiments and theoretical predictions. *Phil. Trans. R. Soc. London*, A 342:573–604, 1993.

[15] R. Greve, T. Koch, and K. Hutter. Unconfined flow of granular avalanches along a partly curved surface. Part I: Theory. *Proc. R. Soc. London*, A 445:399–413, 1994.

[16] K. Hákonardóttir, A. Hogg, T. Jóhannesson, M. Kern, and F. Tiefenbacher. Large-scale avalanche braking mound and catching dam experiments with snow: A study of the airborne jet. *Surveys in Geophysics*, 24(5-6):543–554, 2003.

[17] K. M. Hákonardóttir. *The interaction between snow avalanches and dams*. PhD thesis, University of Bristol, School of Mathematics, 2004.

[18] K. M. Hákonardóttir and A. J. Hogg. Oblique shocks in rapid granular flows. *Physics of Fluids*, 17(7):1–10, 2005.

[19] K. M. Hákonardóttir, A. J. Hogg, T. Jóhannesson, and G. G. Tómasson. A laboratory study of the retarding effects of braking mounds on snow avalanches. *Journal of Glaciology*, 49(165):191–200, 2003.

[20] A. Harten. High resolution schemes for hyperbolic conservation laws. *J. Comput. Phys.*, 49:357–393, 1983.

[21] A. Harten, S. Osher, B. Engquist, and R. Chakravarthy. Some results on uniformly high-order accurate essentially nonoscillatory schemes. *Appl. Numer. Math.*, 2:347–377, 1986.

[22] O. Hungr and N. R. Morgenstern. Experiments on the flow behaviour of the granular-materials at high-velocity in an open channel. *Geotechnique*, 34:405–413, 1984.

[23] O. Hungr and N. R. Morgenstern. High-velocity ring tests on sand. *Geotechnique*, 34:415–421, 1984.

[24] K. Hutter, T. Koch, C. Plüss, and S. B. Savage. The dynamics of avalanches of granular materials from initiation to runout. *Acta Mech.*, 109:127–165, 1995.

[25] K. Hutter, M. Siegel, S. B. Savage, and Y. Nohguchi. Two-dimensional spreading of a granular avalanche down an inclined plane. Part I: Theory. *Acta Mech.*, 100:37–68, 1993.

[26] J. T. Jenkins. Hydraulic theory for a frictional debris flow on a collisional shear layer. *Continuum Mechanics and Applications in Geophysics and in the Environment*, pages 113–125, 2001.

[27] J. T. Jenkins and M. W. Richardson. Boundary conditions for plane flows of smooth, nearly elastic, circular discs. *J. Fluid. Mech.*, 171:53–69, 1986.

[28] S. Keller and D. Issler. Staublawinen über Dämme und Mauern im Labor. Zusammenstellung aller Resultate und Auswertung. *Internal Report of the Swiss Federal Insitute for Snow and Avalanche*, 1996.

[29] K. M. Khan and G. Bushell. Comment on "rolling friction in the dynamic simulation of sandpile formation". *Physica A: Statistical Mechanics and its Applications*, 352(2-4):522–524, 2005.

[30] E. Klingbeil. *Tensorrechung für Ingenieure.* Bibliographisches Institut, Mannheim: Hochschultaschenbcher, 1976.

[31] T. Koch, R. Greve, and K. Hutter. Unconfined flow of granular avalanches along a partly curved chute. Part II: Experiments and numerical computations. *Proc. R. Soc. London*, A 445:415–435, 1994.

[32] H. Kruggel-Emden, E. Simsek, S. Rickelt, S. Wirtz, and V. Scherer. Review and extension of normal force models for the discrete element method. *Powder Technology*, 171(3):157–173, 2007.

[33] Y. G. Kurihara, G. J. Tripoli, and M. A. Bender. Design of a movable nested-mesh primitive equation model. *Mon. Wea. Rev.*, 107:239–249, 1979.

[34] G. Lane-Serff, L. Beal, and T. Hadfield. Gravity current flow over obstacles. *Journal of Fluid Mechanics*, 292:39–53, 1995.

[35] M. Laugier, P. Angot, and L. Mortier. Nested grid methods for an ocean model: A comparative study. *Int. J. Num. Meth. Fluids*, 23:1163–1195, 1996.

[36] R. J. LeVeque. *Numerical methods for conservations laws.* Birkhäuser Verlag Basel Bosten New York, 1992.

[37] S. Li and J. M. Hyman. Adaptive mesh refinement for finite difference WENO schemes. *Los Alamos Report*, (LA-UR-30-8927), 2003.

[38] K. A. Lie and S. Noelle. An improved quadrature rule for the flux-computation in staggered central difference schemes in multidimensions. *J. Sci. Comp.*, 18:69–80, 2003.

[39] K. Lied and S. Bakkehøi. Empirical calculations of snow-avalanche run-out distance based on topographic parameters identified by digital terrain models. *Ann. Glaciol.*, 13:164–169, 1989.

[40] G. R. Liu and M. B. Liu. *Smoothed Particle Hydrodynamics, a meshfree particle method.* Number ISBN: 981-238-456-1. World Scientific Printers, 2003.

[41] D. M. McClung and K. Lied. Statistical and geometrical definition of snow avalanche runout. *Cold Reg. Sci. Technol.*, 13:107–119, 1987.

[42] R. D. Mindlin and H. Deresiewicz. Elastic spheres in contact under varying oblique forces. *J.Appl.Mech.*, 20(3):327–344, 1953.

[43] S. Moriguchi, R. I. Borja, A. Yashima, and K. Sawada. Estimating the impact force generated by granular flow in a rigid obstruction. *Acta Geotechnica*, 4:57–71, 2009.

[44] F. Naaim-Bouvet, M. Naaim, M. Bacher, and L. Heiligenstein. Physical modelling of the interaction between powder avalanches and defense structures. *Natural Hazards and Earth System Sciences*, 2:193–202, 2002.

[45] F. Naaim-Bouvet, S. Pain, M. Naaim, and T. Faug. Numerical and physical modelling of the effect of a dam on powder avalanche motion: Comparison with previous approaches. *Surveys in Geophysics*, 24(5-6):479–498, 2003.

[46] H. Nessyahu and E. Tadmor. Non-oscillatory central differencing for hyperbolic conservation laws. *J. Comput. Phys.*, 87:408–463, 1990.

[47] H. Nessyahu and E. Tadmor. Nonoscillatory central for multidimensional hyperbolic conservation laws. *SIAM J. Sci. Comput.*, 19:1892–1917, 1998.

[48] A. L. Perkins, L. F. Smedstad, D. W. Blake, G. W. Heburn, and A. J. Wallcraft. A new nested boundary condition for a primitive equation ocean model. *J. Geophys. Res.*, 102:3483–3500, 1997.

[49] S. P. Pudasaini and K. Hutter. Rapid shear flows of dry granular masses down curved and twisted channels. *J. Fluid Mech.*, 495:193–208, 2003.

[50] S. P. Pudasaini and K. Hutter. *Avalanche Dynamics: Dynamics of Rapid Flow of Dense Granular Avalanches*. Number ISBN: 978-3-540-32686-1. Springer-Verlag Berlin Heidelberg, 2007.

[51] S. B. Savage and K. Hutter. The motion of a finite mass of granular material down a rough incline. *J. Fluid Mech.*, 199:177–215, 1989.

[52] S. B. Savage and K. Hutter. The dynamics of avalanches of granular materials from initiation to run-out. I. Analysis. *Acta Mech.*, 86:201–223, 1991.

[53] T. Schwager and T. Pöschel. *Coefficient of Restitution for Viscoelastic Spheres: The Effect of Delayed Recovery*, 2007.

[54] T. Schwager and T. Pöschel. Coefficient of restitution and linear-dashpot model revisited. *Granular Matter*, 9(6):465–469, 2007.

[55] A. B. Stevens and C. M. Hrenya. Comparison of soft-sphere models to measurements of collision properties during normal impacts. *Powder Technology*, 154(2-3):99–109, 2005.

[56] P. K. Sweby. High resolution schemes using flux limiters for hyperbolic conservation laws. *SIAM J. Numer. Anal.*, 21:995–1101, 1984.

[57] Y. C. Tai. *Dynamics of granular avalanches and their simulation with shock-capturing and front-tracking numerical schemes*. PhD thesis, TU Darmstadt, 2000.

[58] Y. C. Tai, J. M. N. T. Gray, K. Hutter, and S. Noelle. Flow of dense avalanches past obstructions. *Annals of Glaciology*, 32:281–284, 2001.

[59] Y. C. Tai and C. Y. Kuo. A new model of granular flows over general topography with erosion and deposition. *Acta Mech.*, 199:71–96, 2008.

[60] Y. C. Tai, S. Noelle, J. M. N. T. Gray, and K. Hutter. Shock-capturing and front-tracking methods for granular avalanches. *J. Comput. Phys.*, 175:269–301, 2002.

[61] H. Teufelsbauer, Y. Wang, M. C. Chiou, and W. Wu. Flow-obstacle-interaction in rapid granular avalanches: DEM simulation and comparison with experiment. *Granular Matter*, 11(4):209–220.

[62] E. F. Toro. *Riemann solvers and numerical methods for fluid dynamics, 2nd ed.* Springer-Verlag Berlin Heidelberg New York, 1999.

[63] A. Voellmy. Über die Zerstörungskraft von Lawinen. *Schweizerische Bauzeitung*, 73:159–162, 212–217, 246–249, 280–285, 1955.

[64] Y. Wang and K. Hutter. Comparison of numerical methods with respect to convectively-dominated problems. *Int. J. Numer. Meth. Fluids*, 37:721–745, 2001.

[65] Y. Wang, K. Hutter, and S. P. Pudasaini. The Savage-Hutter theory: A system of partial differential equations for avalanche flows of snow, debris and mud. *J. Appl. Math. Mech.*, 84:507–527, 2004.

[66] M. Wieland, J. M. N. T. Gray, and K. Hutter. Channelized free surface flow of cohesionless granular avalanche in a chute with shallow lateral curvature. *J. Fluid Mech.*, 392:73–100, 1999.

[67] C. Wu, L. Li, and C. Thornton. Rebound behaviour of spheres for plastic impacts. *International Journal of Impact Engineering*, 28(9):929–946, 2003.

[68] H. C. Yee. Construction of explicit and implicit symmetric tvd schemes and their application. *J. Comput. Phys.*, 68:151–179, 1987.

[69] J. Zhang, Z. Hu, W. Ge, Y. Zhang, T. Li, and J. Li. Application of the discrete approach to the simulation of size segregation in granular chute flow. *Industrial and Engineering Chemistry Research*, 43(18):5521–5528, 2004.

[70] Y. C. Zhou, B. D. Wright, R. Y. Yang, B. H. Xu, and A. B. Yu. Rolling friction in the dynamic simulation of sandpile formation. *Physica A: Statistical Mechanics and its Applications*, 269(2):536–553, 1999.

[71] Y. C. Zhou, B. H. Xu, A. B. Yu, and P. Zulli. An experimental and numerical study of the angle of response of coarse spheres. *Powder Techn.*, 125:45–54, 2002.

[72] T. Zwinger, A. Kluwick, and P. Sampl. Numerical simulation of dry-snow avalanche flow over natural terrain. *Dynamic Response of Granular and Porous Materials Under Large and Catastrophic Deformations*, 11:161–194, 2003.

Curriculum Vitae

Persönliche Daten:

Name	Markus Wawra
Geboren	21. Juni 1981
Geburtsort	Wien
Staatsangehörigkeit	Österreich

Ausbildung:

2007 - 2010	Doktoratsstudium am Institut für Geotechnik Universität für Bodenkultur Wien
1999 - 2005	Diplomstudium der Technischen Mathematik Schwerpunkt: Modellbildung und Simulation Diplomarbeit: Identifizierung von medizinischen Modellen Technische Universität Wien
2003 - 2004	Auslandssemester Rijksuniversiteit Groningen, Niederlande
1991 - 1999	BG & BRG Biondekgasse Baden mit Matura abgeschlossen